I. Multi-scale dynamics of mantle plumes
and
II. Compressible thermo-chemical convection and the stability of mantle superplumes

Thesis by

Eh Tan

In Partial Fulfillment of the Requirements
for the Degree of
Doctor of Philosophy

California Institute of Technology
Pasadena, California

2006
(Defended May 2, 2006)

Acknowledgements

I have enjoyed my graduate student life at Caltech. I came to Caltech with very little knowledge about solid earth geophysics. The small, yet diverse, academic background in the GPS division and the Seismo Lab is great for me to learn and to do research.

Special thanks go to my thesis adviser, Michael Gurnis. Mike is always approachable and patient in listening. He gave me a lot of freedom in choosing my research topics, encouraged me when I was stuck in debugging the compressible code, and offered insightful advices.

I would like to thank Don Helmberger for bringing me into the realm of body wave seismology. Without his seismic observations, most of the Part II of this thesis would not exist. His keen eyes on spotting tiny wiggles in the seismograms are unparallel. So does his humor. I would like to thank Michael Aivazis for teaching me the great Python programming language and introducing software engineering to me. Now I am enlightened by patterns, refactoring, unit testing, and various software engineering concepts. I would like to thank Peter Goldreich and Hiroo Kanamori for their guidance on my second oral project. Although the project did not have a final result, I do learn a lot of helioseismology, normal modes, seismic data processing, and atmospheric excitation during the project.

The stimulating discussion with many faculties, including Tom Ahrens, Don Anderson, Paul Asimow, Mark Simons, Dave Stevenson, Joann Stoke, and Jeroen Tromp, has broadened many aspects in my thesis, to whom I gratefully in debt. I would also like to thank my colleagues, including Lijie Han, Sidao Ni, Eun-seo Choi, Steve Quenette, Pat Sunter, and Daoyuan Sun. The collaboration with them is enjoyable and produces great results. The supporting staffs in the lab, including the system administrators – Kimo Yap, Ken Ou, Mike

Black, David Kewley, and the staffs – Elisa Loeffen, Sue Yamada, Evelina Cui, Viola Carter, and Candy Camarena, have done a great job to make the research work as hassle-free as possible.

The acknowledgement will not be complete without a long list of friends: my officemates – Jean Hardebeck, Emily Brodsky, Anu Venkataraman, Eun-seo Choi, Alex Song, and Ravi Konda; the labmates – Magali Billen, Chen Ji, Sidao Ni, Brian Savage, Ying Tan, Zhimei Yan, Anita Ai, Vala Hjorleifsdottir, Qinya Liu, Ozgun Konga, Min Chen, Jeroen Ritsema, Lijie Han, Clint Conrad, Chad Hall, Luc Lavier, Juliette Artru, Yaru Hsu, Vlad and Marina Manea; the Love Wave softball team, the GPS friends – Bruce Hsu, Jessie Wang, Lingsen Zeng, and Jing Liu; the Caltech friends – Ching-Tzu Chen and Shauming Wu; the ACT softball team; my college friends – Mei-Ling Bai, Wenchieh Yen, Woei-Jiun Guo, Yin-Hao Kuo, Josh Chi, Jay Song, and Chao-Wei Tsai. And a very special thank to my girlfriend, Wei-Ting Chen, for her company, patience and love. Without her, life would not have been so colorful.

Last but not the least, I would like to thank my family. I really appreciate the support from my parents during all my life. They have made their best efforts in raising four kids, offering us best education, and teaching us good manners and proprieties. They encouraged me to study abroad. My sisters have taken the responsibilities of taking care of our parents while I am far away on the other side of the ocean. My family, I am really proud of being a member of you.

Abstract

The dynamic interaction of mantle plumes with subducted slabs and plate-scale flow is studied in Part I. We found that plumes preferentially develop on the edge of slabs and that a substantial amount of hot mantle can be trapped beneath slabs over long periods of time, leading to “mega-plume” formation. We used the solver-coupling technique to study the deflection of plume conduits and compare our result with the parameterized approach. The stability of mantle superplumes in compressible thermo-chemical convection is studied in Part II. The depth-dependent chemical density profile, caused by composition-dependent compressibility, is the preferred mechanism to stabilize the superplumes.

Table of Contents

List of Figures

List of Animations

List of Tables

Chapter 1

Introduction

In this thesis, we use numerical models to explore the dynamics of mantle convection, especially plumes and superplumes. This thesis is composed of two parts. In Part I, the dynamics of thermal plumes and their interaction with large-scale flow and subducting slabs are explored. Part II focus on the largest-scale upwellings within the lower mantle (superplumes). Specifically, we develop a dynamic scenario to understand mantle superplumes consistent with seismological, geochemical and mineralogical constraints. Both parts of the thesis involve substantial developments in computer software, especially new methodologies that might have wide applicability within geophysics.

In Part I, we study the dynamics of plumes at different length scales with models of thermal convection. Plumes may originate from the thermal boundary layer at the core-mantle boundary (CMB). Small-scale instabilities, on the order of 10 km, grow within the thermal boundary layer and later erupt as plumes. On the other hand, plume formation is modulated by large-scale flow induced by subducted slabs. Cold and dense slabs descend through the mantle and induce a flow of 10^5 km scale. The large-scale flow can locally thicken or thin the thermal boundary layer at the CMB, which promotes or inhibits plume formation. Once a plume erupts from the CMB, it has a large plume "head." The plume head ascends through the mantle and rises to the surface. A narrow "tail," or plume conduit, connects the plume head with the thermal boundary layer. Warm material from the thermal boundary layer rises through the conduit. The diameter of the conduit is likely around 100 km. Like a plume of smoke rising from a chimney and deflected by the wind, a mantle plume conduit can be deflected by large-scale mantle flow as well. Simulating the process of plume formation and plume conduit deflection requires a very fine grid resolution, while modeling the large-scale flow requires a large computation domain. A model with large computation domain and fine grid resolution will demand massive computation resources and is presently impractical. We will use two different approaches to reconcile both requirements of fine-scale and large-scale models in Chapter 2 and 3.

In Chapter 2, we explore the large-scale flow and fine-scale flow with models separately at these scales. We first address the question, “Can subducted slabs reach the CMB?” using large-scale 2-D and 3-D models. We find that an increase in lower mantle viscosity, a phase transition at 660 km depth, depth-dependent coefficient of thermal expansion, and depth-dependent thermal diffusivity do not preclude model slabs from reaching the CMB. Only a few continuous slab-like features from the surface to the CMB are observed in seismic tomography. This observation is often cited as evidence against slabs reaching the CMB and as evidence of mantle layering. With Lijie Han, we performed 3-D regional spherical models with actual plate reconstructions. We show that slabs are unlikely to be continuous from the upper mantle to the CMB, even for radially simple mantle structures. We argued that the discontinuous slab-like features in seismic tomography result from the details of plate convergence, not mantle layering. Later in Chapter 2, we explore the effect of slabs on plume formation using 2-D fine-scale models. We find that plumes preferentially develop on the edge of slabs. An important result is that a substantial amount of hot mantle can be trapped beneath slabs over long periods of time, leading to “mega-plume” formation. This model for mega-plume formation has important predictions for mantle geochemistry and structural seismology.

In Chapter 3, using new development in computer science called “frameworks,” we developed a method of solver coupling and then applied the results to the deflection of a plume conduit. The coupled model has a fine resolution solver with a small computational domain embedded within a coarse resolution solver with a large computational domain. Together with Eun-seo Choi, Pururav Thoutireddy and Michael Aivazis, we developed a general-purpose software package allowing multiple solvers to communicate and mutually coordinate their activity during a large parallel computation. The result is a dynamically consistent and computationally efficient method for simulating large domains with locally refined resolution. The method is dynamically consistent because the two solvers communicate with each other to ensure consistent dynamic variables, and is computational efficient because the coarse resolution solver is not invoked as frequently as the fine resolution solver. The deflection of the Hawaiian plume within large-scale mantle flow is modeled with the framework-coupled solvers and then compared against a simple parameterized model. The parameterized model is computationally efficient, but its predicted plume track differs from the coupled model by 20%.

In Part II, we study the stability of mantle superplumes in the context of thermo-chemical convection. There are two superplumes, regions of low seismic velocity, at the base of the mantle, one beneath the southern Africa and the other beneath the southwestern Pacific. From various geophysical observations, the superplumes are expected to be warmer and have a distinct chemical composition than surrounding mantle. Although these chemical structures are called “superplumes,” whether they are stable (i.e. will remain at the base of the mantle at least for several hundred million years) or unstable (i.e. will rise to the upper mantle or mix with surrounding mantle in a few hundred million years) remains unresolved. Many geochemical observations require that some regions of the mantle (reservoir) remain isolated from the rest of the mantle for more than a billion years. Stable superplumes could be this geochemical reservoir. The stability of superplumes becomes an important issue in both geophysics and geochemistry. In Chapter 4 to 7, we present observational constraints on the southern African superplume and develop a series of models to explain the morphology, seismic signature, and stability of the superplume. In the preferred model, the superplume is composed intrinsically denser material with a higher bulk modulus than ambient mantle. Such a superplume can remain at the base of the mantle for billion years and satisfies seismological, geochemical, and mineralogical constraints.

In Chapter 4, we first present the work of Sidao Ni and Don Helmberger on the discovery of sharp boundary of the African superplume. The seismic observation shows that the African superplume is a large structure with a width of 1000 km, extending obliquely upward from the CMB by 1200 km. The boundary of the African superplume appears to be sharp, with a width less than 50 km, indicating the presence of a chemical boundary. Then, using an incompressible thermo-chemical convection model, we compute a series of dynamic models. We find that only unstable chemical structures can reproduce the observed morphology (shape and dimension) of the superplume and that models with constant coefficient of thermal expansion fit the morphology better than models with Earth-like depth-dependent coefficient of thermal expansion. The later result is puzzling and implies an important process is missing in our dynamic models.

In Chapter 5, we resolve the puzzle in Chapter 4 by introducing composition-dependent compressibility. The African superplume has a bulk modulus higher than that of ambient mantle. Materials with different compressibility (the inverse of bulk modulus) have different density profiles. The density difference of materials with different bulk modulus will vary with depth. Such a depth-dependent variation in density difference can stabilize a thermo-chemical structure. A new compressible thermo-chemical convection code is developed to demonstrate the concept. The resultant chemical structure has a similar morphology to the African superplume. We call this type of chemical structure “metastable dome.” But can we exclude other models of mantle superplumes? In Chapter 6 and 7, we address the uniqueness of superplume models.

In Chapter 6, we systematically explore the effect of composition-dependent compressibility (i.e., depth-dependent density difference) and depth-dependent thermal expansion. We find a wide range of morphologies for the chemical structures. Several models are morphologically similar to the superplume. These dynamic models are converted into seismic velocity anomalies and compared with seismic observation. The thermo-elastic parameters used in the conversion provide additional mineralogical constraints. We find that only metastable domes can simultaneously satisfy seismological, geochemical and mineralogical constraints on the superplumes.

In Chapter 7, we explore the competing effects of composition-dependent rheology and depth-dependent thermal expansion on the stability of a thermo-chemical structure. The chemical structure has an intrinsic viscosity increase and convects slowly. Such a structure can be morphologically similar to the superplume and is stable. We demonstrate that the strong temperature gradient inside the chemical structure, caused by composition-dependent rheology, is the dominant factor in stabilizing the structure. Such a temperature gradient will generate a strong gradient in seismic velocity, which is not observed. Other mechanisms, including temperature-dependent rheology with negative activation enthalpy and radiative heat transfer, could potentially stabilize the chemical structure as well. However, the plausibility of these mechanisms has never been demonstrated. In contrast, composition-dependent compressibility should exist in the mantle and is the most plausible mechanism for stabilizing a chemical anomaly at the base of the mantle.

Part I. Multi-scale dynamics of mantle plumes

Chapter 2

Slabs in the lower mantle and their modulation of plume formation

Published in *Geochemistry, Geophysics, Geosystems* (2002) by Eh Tan, Michael Gurnis, and Lijie Han, **3**, 1067, doi:10.1029/2001GC000238.

Abstract

Numerical mantle convection models indicate that subducting slabs can reach the core-mantle boundary (CMB) for a wide range of assumed material properties and plate tectonic histories. An increase in lower mantle viscosity, a phase transition at 660 km depth, depth-dependent thermal expansivity, and depth-dependent thermal diffusivity do not preclude model slabs from reaching the CMB. We find that ancient slabs could be associated with lateral temperature anomalies ~500˚C cooler than ambient mantle. Plausible increases of thermal conductivity with depth will not cause slabs to diffuse away. Regional spherical models with actual plate evolutionary models show that slabs are unlikely to be continuous from the upper mantle to the CMB, even for radially simple mantle structures. The observation from tomography showing only a few continuous slab-like features from the surface to the CMB may be a result of complex plate kinematics, not mantle layering. There are important consequences of deeply penetrating slabs. Our models show that plumes preferentially develop on the edge of slabs. In areas on the CMB free of slabs, plume formation and eruption are expected to be frequent while the basal thermal boundary layer would be thin. However, in areas beneath slabs, the basal thermal boundary layer would be thicker and plume formation infrequent. Beneath slabs, a substantial amount of hot mantle can be trapped over long periods of time, leading to “mega-plume” formation. We predict that patches of low seismic velocity may be found beneath large-scale high-seismic-velocity structures at the core-mantle boundary. We find that the location, buoyancy, and geochemistry of mega-plumes will differ from those plumes forming at the edge of slabs. Various geophysical and geochemical implications of this finding are discussed.

2.1 Introduction

Several geophysical observations suggest that slabs penetrate the 660 km seismic discontinuity and descend into the lower mantle. Global tomography models show that some continuous high-seismic-velocity anomalies extend from active subduction zones to a depth of at least 2000 km [*Grand et al.*, 1997; *van der Hilst et al.*, 1997]. Beneath Japan (Figure 2-1) and the Caribbean, high seismic-velocity anomalies extend nearly continuously from the upper mantle to the very base of the mantle. The spatial distribution of high-seismic-velocity anomalies in the deep mantle correlates with the position of past subduction [*Richards and Engebretson*, 1992]. However, seismic tomography generally shows that slab continuity from the upper mantle to the CMB is variable, with substantial down dip and along strike variations [*Megnin and Romanowicz*, 2000; *Ritsema and van Heijst*, 2000]. In addition to tomography, other arguments have been advanced suggesting that flow associated with plates penetrates deeply into the lower mantle [*Richards and Engebretson*, 1992] For example, the occurrence of positive geoid and gravity anomalies over subduction zones is most consistent with penetration of slabs into the lower mantle [*Hager*, 1984]. In addition, if the mantle were perfectly layered with a thermal boundary layer (TBL) at 660 km depth, robust buoyant upwellings would produce asymmetrical bathymetry at mid-ocean ridges, which are not observed [*Davies*, 1989].

Some geochemical arguments are also consistent with deeply penetrating slabs. Oceanic island basalts (OIBs) have a wide spectrum of isotopic heterogeneity. The origin of the heterogeneity is attributed to different reservoirs in the deep mantle [*Hofmann*, 1997]. One reservoir sampled by HIMU OIB ("high μ"; $\mu \equiv {}^{238}\text{U}/{}^{204}\text{Pb}$) has the highest ${}^{206}\text{Pb}/{}^{204}\text{Pb}$, ${}^{207}\text{Pb}/{}^{204}\text{Pb}$, and ${}^{208}\text{Pb}/{}^{204}\text{Pb}$ and the lowest ${}^{87}\text{Sr}/{}^{86}\text{Sr}$ of any OIB. The high Pb ratios indicate

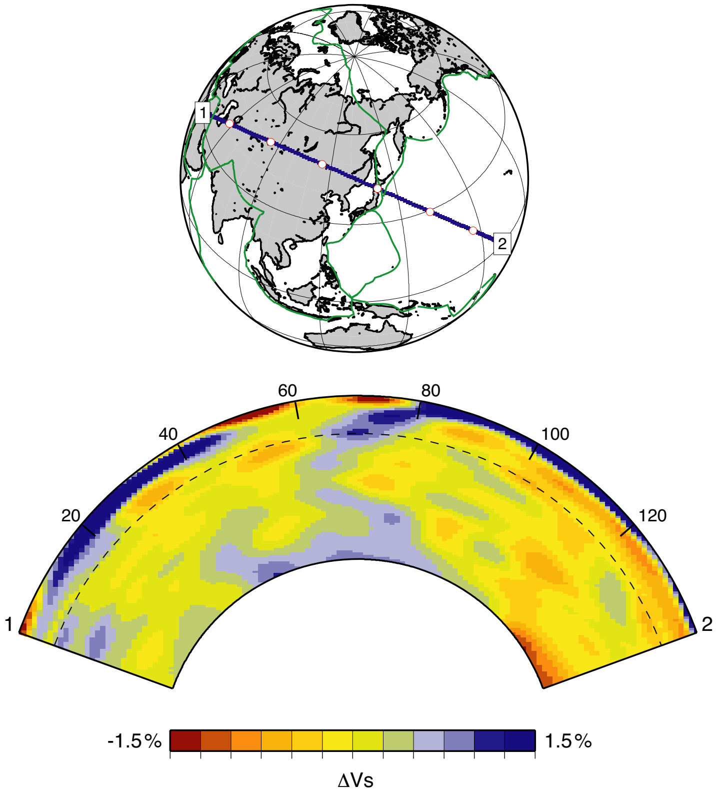

Figure 2-1. Tomography model S20RTS across Japan subduction zone [*Ritsema and van Heijst*, 2000]. The continuous high seismic velocity anomaly extending from the subduction zone to the CMB is most consistent with subduction of oceanic lithosphere into the lower mantle, clear down to the core mantle boundary.

enrichment in U and Th in the HIMU source, while the low Sr ratio indicates depletion in Rb. One potential source of the HIMU reservoir is oceanic crust that has been returned to the deep mantle during subduction [*Hofmann and White*, 1982]. The high Pb ratios and low Sr ratio of HIMU are inherited from the high U and low Rb in the oceanic crust.

Although seismic tomography models provide evidence that some slabs penetrate into the lower mantle, it is not clear that they penetrate to the CMB. There are several factors that might hinder and delay slab descent, leading to substantial warming of slabs before reaching the CMB. In a mantle with a highly viscous lower mantle and a decreasing thermal expansivity with depth, slabs would take a longer time to descend through the lower mantle, perhaps long enough for a slab to thermally dissipate. The radioactive heating in the mantle and slab, although small, might have some influence in the limit of long descent times. Furthermore, the thermal conductivity may increase with depth [*Hofmeister*, 1999] and potentially diminish the temperature anomaly in the slab [*Hauck et al.*, 1999]. Applying these various effects in mantle convection models, we explore under what conditions a slab can survive as a distinct thermal and mechanical entity before reaching the CMB.

On the other hand, assuming that slabs can indeed reach the CMB, they are likely to have a profound influence on the dynamics near the CMB. Regions, called ultra-low velocity zones (ULVZs), with reduction of *P*- and *S*-wave velocities over 10%, are observed at the CMB [*Garnero and Helmberger*, 1996; *Vidale and Hedlin*, 1998; *Ni and Helmberger*, 2001]. Plumes, presumably emanating from a TBL, are putatively rooted at the CMB. The interaction of slabs with ULVZs and plume roots might influence their geographical location.

Three types of dynamic models are presented in this paper. First, large-scale two-dimensional (2-D) cylindrical models with depth-dependent material properties, meant to simulate flow through the whole mantle, were formulated to show under what conditions slabs could reach the CMB. Second, 3-D spherical models with imposed plate evolution were formulated to explore the morphology of slabs in the presence of realistic evolution of surface plates. Last, high-resolution, fine-scale, 2-D Cartesian models were formulated to investigate the evolution of slabs near the CMB. Aspects of the formulation common to all of the models will first be described, followed by specified model characteristics and results. Various geophysical and geochemical implications are then considered. Since none of the models include chemical variation, when we refer to “slab,” we mean “cold anomaly.”

2.2 Methods

The numerical calculations were performed by solving the non-dimensional conservation equations of mass, momentum, and energy under using the Boussinesq approximation. The continuity (mass conservation) equation is (except where indicated, all quantities are non-dimensional)

$$\nabla \cdot u = 0 \tag{4-1}$$

where u is the velocity. The momentum equation for a fluid with an infinite Prandtl number is

$$\nabla \cdot \left(\eta(r,T)\nabla u\right) = -\nabla p + \left(\alpha(r)R_a T - R_b \Gamma\right)e_r = 0 \tag{4-2}$$

where η is the dynamic viscosity, p is the dynamic pressure, α is the thermal expansivity, R_a is the thermal Rayleigh number, R_b is the Rayleigh number associated with the density jump across a phase change, Γ is the phase change function, T is the temperature, r is the radius, and e_r is the unit vector in the radial direction.

The energy equation is

$$\frac{\partial T}{\partial t} = -u \cdot \nabla T + \nabla \cdot \left(\kappa(r)\nabla T \right) + H \tag{4-3}$$

where κ is the thermal diffusivity, H is the internal heating number, and t is time. Γ is defined as

$$\Gamma = \frac{1}{2}\left(1 + \tanh\left(\frac{1 - r - d_{ph} - \gamma(T - T_{ph})}{w_{ph}}\right)\right) \tag{4-4}$$

where d_{ph} and T_{ph} are the ambient depth and temperature of a phase change, γ is the Clapeyron slope of a phase change, and w_{ph} is the width of a phase transition. The non-dimensional Rayleigh numbers, R_a and R_b, are defined in terms of dimensional quantities

$$R_a = \frac{\rho_0 g \alpha_0 \Delta T R_0^3}{\kappa_0 \eta_0} \tag{4-5}$$

$$R_b = \frac{\Delta \rho_{ph} g R_0^3}{\kappa_0 \eta_0} \tag{4-6}$$

where ρ_0 is the reference density, g is the gravitational acceleration, α_0 is the reference thermal expansivity, ΔT is the temperature increase across the mantle, R_0 is the scale height of the domain, κ_0 is the reference thermal diffusivity, η_0 is the reference viscosity, and $\Delta\rho_{ph}$ is the density jump across a phase change. The functional forms of material properties, α, κ and η, are different in the large-scale and fine-scale models, and will be given below along with the boundary and initial conditions.

2.2.1 Large-scale Model (2-D)

A series of 2-D models of thermal convection in a cylindrical geometry with imposed plate kinematics were computed to investigate the evolution of subduction from the surface to the CMB. We followed the finite element method of *Sidorin and Gurnis* [1998]. The values of all parameters in Equation (2-4)–(2-6) are listed in Table 2-1. In this set of models, the material properties, α, κ and η, are depth-dependent.

At higher pressure, it requires more energy to expand or compress a mineral. So, thermal expansivity decreases with depth. This high-pressure behavior has been determined experimentally for perovskite and magnesiowüstite [*Wang et al.*, 1994; *Chopelas*, 1996] and is well represented by the non-dimensional equation:

$$\alpha(r) = \frac{\alpha_s}{1 + a(1 - r)^b} \tag{4-7}$$

where α_s=2.93 is the non-dimensional thermal expansivity at the surface, and a=10.5 and

Table 2-1. Values of parameters used in large-scale models (2-D).

Symbol	**Value**
ρ_0	4000 kg/m^3
g	10 m/s^2
ΔT	2900 K
R_0	6371 km
α_0	1.53x10^{-5} K^{-1}
κ_0	10^{-6} m^2/s
η_0	5.57x10^{21} Pa·s
$\Delta\rho_{ph}$	340 kg/m^3
w_{ph}	5.49x10^{-3}
d_{ph}	0.895
T_{ph}	0.5
γ	-0.0398
R_a	7.239x10^7
R_b	1.383x10^8

b=0.85 are fitting constants. This equation is an empirical fit to the theoretical values of thermal expansivity along a mantle adiabat [*Sidorin and Gurnis*, 1998]. The dimensional value of reference thermal expansivity, α_0, is chosen so that the volume average (geometric mean) of α is equal to 1.

Most radial viscosity profiles inverted from the geoid and postglacial rebound have a one to two orders of magnitude increase across the 660 km discontinuity [*Hager et al.*, 1985; *Mitrovica and Forte,* 1997; *Lambeck et al.*, 1998]. In order to include this effect, we used a modified Arrhenius law

$$\eta(r,T) = \eta^* \exp(\frac{c_1}{c_2+T} - \frac{c_1}{c_2+T_m}) \qquad (4\text{-}8)$$

where η^*=0.18 in the upper mantle and 1.8 in the lower mantle, T_m=0.5 is the non-dimensional temperature of ambient mantle, c_1=17.22, and c_2=0.64. A high viscosity cutoff of 10^3 is used. These parameters give three orders of magnitude variation in viscosity across the top TBL, one order of magnitude viscosity jump across the 660 km discontinuity, and another two orders of magnitude variation across the bottom TBL. The dimensional value of reference viscosity, η_0, is chosen so that the volume average (geometric mean) of η is equal to 1.

The thermal diffusivity, proportional to the thermal conductivity, may increase with depth (decrease with r) [*Hofmeister,* 1999]. Because the precise relation between κ and r is unknown, a simple implementation is used

$$\kappa(r) = 1 + \delta_\kappa f(r) \tag{4-9}$$

where δ_κ is a model parameter that controls the variation of thermal diffusivity across the mantle, and $f(r)$ is a stepwise decreasing function with value from 1 to 0. This formula represents a 10-layer mantle, with constant thermal diffusivity in each layer. The dimensional value of reference thermal diffusivity, κ_0, is chosen to be the surface thermal diffusivity.

The phase change parameters are chosen to be consistent with seismological observations and high-pressure experiments. From the amplitudes of reflected seismic phases off the 660 km discontinuity, the density jump across the discontinuity is estimated as ~4–6% [*Shearer and Flanagan*, 1999], substantially below the value of 9.3% in PREM [*Dziewonski and Anderson*, 1981]. The Clapeyron slope of spinel dissociation has been determined experimentally and falls between -2.8 MPa/K [*Ito and Takahashi*, 1989] to -3±1 MPa/K [*Akaogi and Ito*, 1993a]. To infer the minimum temperature anomalies of slabs when they reach the CMB, we overestimated the influence of the post-spinel phase change. We used phase change parameters corresponding to an ambient depth of 660 km with Clapeyron slope of -3.5 MPa/K and a density jump of 8.5%.

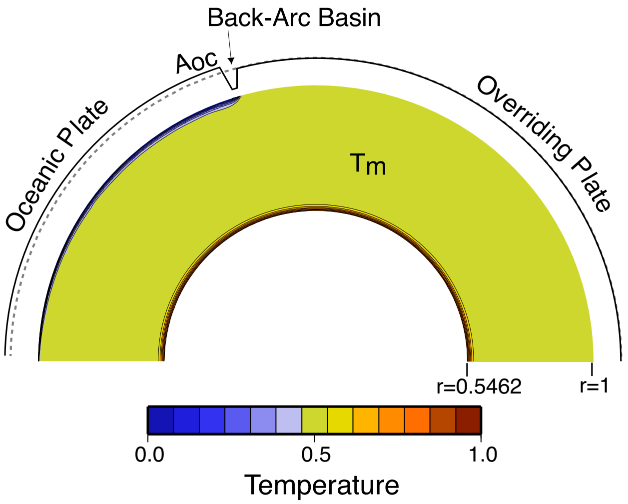

Figure 2-2. Initial configuration of 2-D large-scale models. There are three tectonic plates at the top with different velocity and temperature boundary conditions. These plates are, from left to right, the oceanic plate (OC), a plate within the back-arc basin (overshooting plate, OS), and the overriding plate (OR). The velocities of these plates are V_{OR}=-0.25 cm/yr, V_{OS}=-5V_{OC}, and V_{OC} is a model parameter. The plate boundaries between OC and OS and that between OR and OS both have the same velocity as V_{OR}. The temperature on the top surface is T_{OS}=T_{OR}=0.5 and T_{OC}=0. The age of the oceanic plate at the trench, A_{OC}, is another model parameter. On the bottom surface, free-slip velocity boundary conditions are used and temperature is 1. Reflection boundary conditions are used for both sidewalls. The mantle has an initial uniform temperature T_m=0.5.

The computations were performed within a half annulus (Figure 2-2) in a cylindrical coordinate system (r, φ), where the inner radius corresponds to the CMB and the outer radius corresponds to the surface of the Earth. This domain is divided into 400 elements in the φ direction and 100 elements in the r direction. The mesh was refined vertically and horizontally to increase the resolution in the TBLs and in the area of subduction, with a minimum grid spacing of 15 km. Reflecting boundary conditions were used for both sidewalls. At the bottom, free-slip velocity boundary conditions were used and temperature was kept constant at 1. At the top, plates were simulated by imposing piecewise constant velocity boundary conditions. There were three plates along the top. Each had different velocity and temperature boundary conditions. These plates were, from left to right, the oceanic plate, a plate within the back-arc basin, and the overriding plate. The back-arc basin was introduced to initiate subduction and to prevent the slab from being sucked up under the overriding plate [*Christensen*, 1996]. The thickness of the oceanic plate progressively increased from the ridge (left margin) to the trench (right margin) and was concordant with the plate age A_{OC}. The mantle was initially isothermal, with T_m=0.5, except for the bottom TBL. These calculations were meant to model an oceanic plate descending through an initially isothermal mantle with a hot TBL at the CMB. In one model, a different initial condition is used; the slab descends through a mantle with preexisting convection. All models were integrated forward in time until slabs reached and spread along the top of the CMB.

2.2.2 Large-scale Model (3-D)

With a somewhat simpler mantle structure, we explored the influence of a realistic evolving plate boundary on slab morphology. Using CitcomS, a spherical finite element code [*Moresi et al.*, 2000], we set up a regional model, which encompassed the evolution of the western boundary of North America from the Cretaceous to the present.

The mantle was purely heated from below and was initially isothermal at T_m=1. This configuration only resulted in a small amount of basal heating such that no plumes formed. There was one phase change in the model, representing the 660 km discontinuity. The phase change parameters corresponded to an 8.5% density jump. The values of all parameters in Equation (2.4)–(2.6) are listed in Table 2-2. Both the thermal expansivity and thermal diffusivity were constant through the mantle, while the viscosity was temperature- and depth-dependent. The temperature-dependent part of viscosity was expressed as Equation (2-8).

Table 2-2. Values of parameters used in large-scale models (3-D).

Symbol	**Value**
ρ_0	3500 kg/m^3
g	10 m/s^2
ΔT	1500 K
R_0	6371 km
α_0	2x10^{-5} K^{-1}
κ_0	10^{-6} m^2/s
η_0	2x10^{21} Pa·s
$\Delta\rho_{ph}$	340 kg/m^3
w_{ph}	5.8x10^{-3}
d_{ph}	0.875
T_{ph}	1
R_a	1.357x10^7
R_b	3.846x10^8

The mantle was divided into four layers with a different set of constants (η^*, c_1, c_2) in each layer (Table 2-3). The Clapeyron slopes and viscosity of lower mantle are varied in different models (Table 2-4).

The model domain was 220° to 310°E and 0° to 45°N, extending from the surface to the CMB. On these four vertical boundaries, the shear stress was set to zero. The bottom surface had free-slip and isothermal boundary conditions, with temperature kept at T_m. The top surface, like the 2-D large-scale model just described, had imposed velocity boundary conditions. The top surface had a constant temperature T=0.

Three different plate evolutionary models were used. The coordinates of plate boundaries and poles of rotations are from *Lithgow-Bertelloni and Richards* [1998]. For the first evolutionary model (used for NA1–NA3), the calculations started at 119 Ma with an evolving set of plate motions. Since this model started with an isothermal mantle, subduction essentially initiated at the western boundary of the North American plate at 119 Ma. In a

Table 2-3. Viscosity in each layer used in large-scale models (3-D).

Depth (km)	**Viscosity (Pa·s)**	**Viscosity Variation**
0–90	$2x10^{23}$	100
90–410	$4x10^{18}$	200
410–660	$4x10^{21}$	10
660–CMB	varying	10

Table 2-4**.** Large-scale (3-D) models.

Model	**Clapeyron slope (MPa/K)**	**Lower mantle viscosity (Pa·s)**	**Plate evolutionary model (see text)**
NA1	3.5	$2x10^{22}$	Model 1
NA2	1.75	$2x10^{22}$	Model 1
NA3	1.75	$4x10^{22}$	Model 1
NA4	1.75	$2x10^{22}$	Model 2
NA5	1.75	$2x10^{22}$	Model 3

second evolutionary model (used only for NA4), the plate evolution from 119 Ma to the present was identical to that used for NA1–NA3. However, prior to 119 Ma, we continuously imposed the 119 Ma plate reconstruction for 70 Myrs; since the model started with an isothermal mantle, subduction essentially initiated at 189 Ma along the western boundary of the North American plate. Finally, in a third evolutionary model (used only for NA5), we incorporated evolving plate boundaries back to 150 Ma while also incorporating the distributed (non–plate tectonic) strain of western United States from 20 Ma to the present using the reconstructions in *Atwater and Stock* [1998].

2.2.3 Fine-scale Model

Lastly, we formulated a series of fine-scale 2-D Cartesian models to investigate the interaction between a slab and the CMB using the finite element program ConMan [*King et al.*, 1990]. The models had a dimension of 3000 km in width and 1500 km in height and were

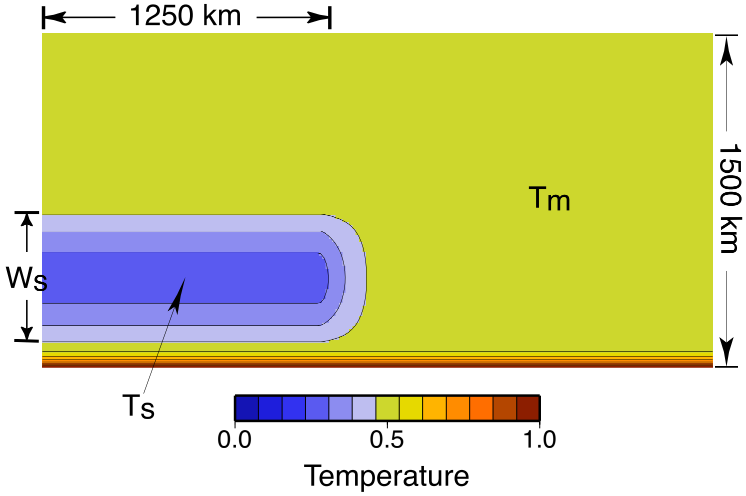

Figure 2-3. Initial configuration of fine-scale models. A slab with a constant length, 1250 km, but variable thickness, W_s, and temperature, T_s, laid horizontally 80 km above the CMB. A TBL with a temperature profile as if developed for 100 Myrs was imposed along the bottom. The mantle was initially at a uniform temperature, T_m, of 0.5.

computed on a mesh with 300 elements in the horizontal direction and 150 elements in the vertical direction. The grid size was uneven, with a minimum grid spacing of 5 km. For this study, the dynamics were determined by the initial conditions of a slab, which consisted of slab temperature, thickness, and viscosity. A slab with an initial length of 1250 km, but variable thickness, W_s, and temperature, T_s, laid horizontally 80 km above the CMB (Figure 2-3).

The models initially started with a TBL along the bottom with a uniform mantle temperature (T_m=0.5). Reflecting boundary conditions were used for both sidewalls. At the bottom, free-slip boundary conditions were used and the temperature was kept constant at 1. At the top, permeable boundary conditions were used. These boundary conditions allowed plumes to ascend and escape from the calculation domain while the continuity equation ensured that the total volume of the domain was conserved.

Table 2-5. Values of parameters used in fine-scale models.

Symbol	Value
ρ_0	5000 km/m^3
g	10 m/s^2
ΔT	2900 K
R_0	1500 km
α_0	10^5 K^{-1}
κ_0	10^{-6} m^2/s
η_0	10^{22} Pa·s
R_a	4.89x10^5
R_b	0

The material properties used here are different from those used in the large-scale models. Because the depth variation is half of the value used in the large-scale models, we used a constant thermal expansivity and diffusivity. The viscosity is only temperature-dependent, and a two-step rheology is used

$$\eta(T) = \begin{cases} 10^{-6(T-T_m)} & \text{for } T > T_m \\ 10^{-\delta_\eta (T-T_m)/(T_s-T_m)} & \text{for } T < T_m \end{cases} \qquad (4\text{-}10)$$

where δ_η is a parameter controlling the viscosity variation in the slab. This relation allows the initial viscosity contrast between the slab and mantle to be held constant while changing the initial slab temperature. This allows us to deconvolve the influence of slab viscosity from its temperature during its subsequent evolution. The temperature dependence of viscosity gives δ_η orders of magnitude variation in viscosity between the slab and mantle and 3 orders of magnitude variations between the mantle and CMB. We did not consider internal heating because basal heating dominates the dynamics of this problem. The values of all parameters in Equations (2-4)–(2-6) are listed in Table 2-5.

Table 2-6. Results of large-scale models (2-D).

Model	V1	V2	V3	K2	K3	K4	K8	H1	P1	P2
V_{OC} (cm/yr)	5	10	2.5	5	5	5	5	5	5	5
A_{OC} (Myrs)	130	65	260	130	130	130	130	130	130	130
δ_κ	0	0	0	1	2	3	7	0	0	2
H	0	0	0	0	0	0	0	18	0	18
Phase change	No	No	No	No	No	No	No	No	Yes	Yes
W_s (km)	498	459	546	543	543	543	543	467	645	546
T_s	0.30	0.31	0.31	0.31	0.34	0.37	0.40	0.30	0.28	0.34
Temp. anomaly $(T_m-T_s)\Delta T$ (˚C)	580	551	551	551	464	377	290	580	638	464

2.3 Results

2.3.1 Large-scale Model (2-D)

For different models, we varied oceanic plate velocity and age (labeled V), thermal diffusivity (labeled K), internal heating (labeled H), and the presence of a 660 km phase change (labeled P). The parameters and results of models are listed in Table 2-6.

For all the models explored, slabs consistently descend to the CMB with substantial temperature anomalies. The animation from model P2 demonstrates the typical history of a slab (Animation 2-1; Figure 2-4). In this model, the position of subduction rolls back to the left, governed by the boundary conditions, and the slab directly penetrates the 660 km phase change. The slab only thickens slightly as it enters the more viscous and dense lower mantle.

Animation 2-1. The evolution of Model P2. The white line marks the 660 km phase boundary. The solid gray line shows the plate velocities, with dashed gray line as the baseline. Portions inside the two red boxes are magnified within the insets. Color scheme: red is warm; blue is cool.

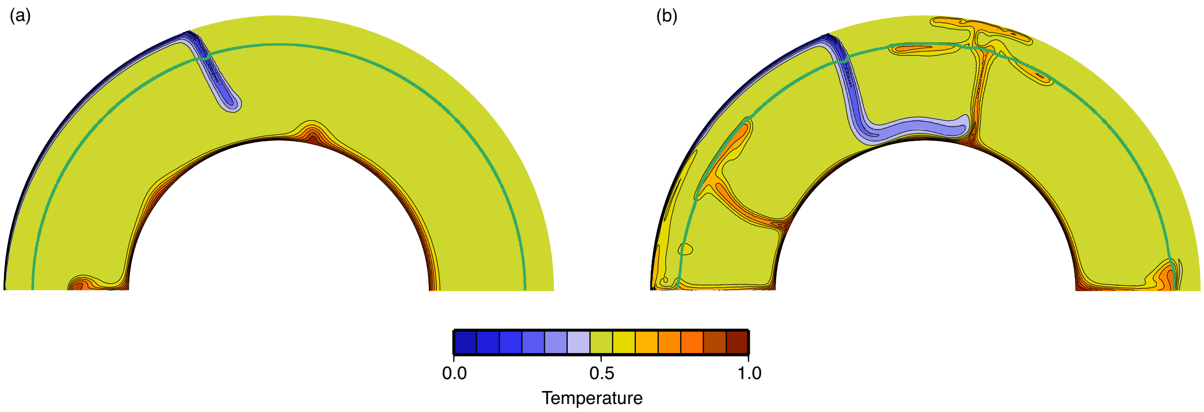

Figure 2-4. Temperature fields of Model P2. The green lines mark the 660 km phase boundary. (a) When the slab descends through the lower mantle, it induces a down welling flow. This flow depresses the thickness of the TBL directly beneath the slab and pushes hot materials aside, thus thickening the neighboring TBL, even when the slab is still relatively distant from the CMB. The thickened TBL is prone to instability and initiates the growth of a new plume. (b) As the tip of the slab reaches the CMB, the slab slides horizontally while sweeping hot material aside (including the plume root).

The near vertical dip of the slab and the simplicity of the initial and boundary conditions result in a continuous, unbroken slab. The slab, while descending through the lower mantle, induces a downwelling flow and depresses the thickness of the underlying TBL. This flow pushes hot mantle aside (left inset of Animation 2-1) so that the neighboring TBL thickens, even when the slab is hundreds of kilometers above the CMB (Figure 2-4a). The thickening TBL is prone to instability and new plumes form (right inset of Animation 2-1). As the tip of the slab reaches the CMB, the slab slides horizontally and sweeps hot mantle aside, including the plume root, until the slab comes to a rest on the CMB (Figure 2-4b). Therefore, in these 2-D models, there is always a plume on the tip of the slab. Similar phenomena have been noticed by other studies [*Weinstein et al.*, 1989; *Lenardic and Kaula*, 1994; *Lowman and Jarvis*, 1996; *Zhong and Gurnis*, 1997; *Sidorin et al.*, 1999].

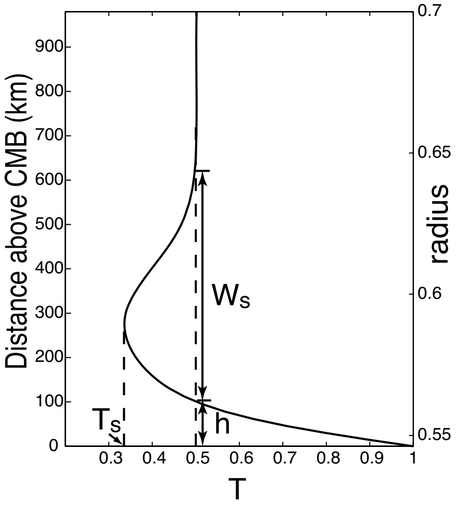

Figure 2-5. The temperature profile across the slab in the final step of model P2. T_s and W_s are the temperature and thickness of the slab. h is the height of the slab above the CMB.

The slab also folds and buckles as it approaches the CMB. Even with trench rollback, slabs near the CMB can be found under both the overriding and subducting plates. It also appears that some hot mantle can become trapped beneath the cold slab.

The temperature and thickness of the slab, T_s and W_s, are measured by taking a temperature profile (Figure 2-5) near the mid-point of the flat-lying slab, where the horizontal temperature variation is small. T_s is defined as the minimum temperature in the profile, and W_s is defined as the vertical extent of the slab (the region with $T<T_m$). The height of the slab above the CMB, h, is defined as the distance between the base of the slab (where $T=T_m$) and the CMB. The values of T_s and W_s for all models are given in Table 2-6. We find that slabs usually lie 50–80 km above the CMB and are associated with a temperature anomaly of 300˚ to 600˚C while having thicknesses of 450 to 650 km.

The results show that T_s and W_s do not change substantially in spite of the variation in the plate age. According to the half-space cooling-plate model, the oceanic plate thickness is proportional to the square root of the plate age. Model V3 has an oceanic plate four times older than model V2, thus the plate is twice as thick on the surface, but the slab in V3 is only 16% thicker and is as cold as the slab in V2. This result can be explained by the compensating effect of different plate velocities. When slabs reach the lower mantle, the vertical descent of slabs decrease and slabs thicken in response to the increase of viscous resistance. This advective thickening may have been observed in several subduction zones [*Creager and Jordan*, 1986; *Fischer et al.*, 1991; *Ding and Grand*, 1994; *Pankow and Lay*, 1999]. A fast-moving slab may experience more advective thickening, so it gets more insulated and heats less than a slow-moving slab. On the other hand, a slab attached to a fast-moving plate spends less time in the mantle before reaching the CMB and heats less.

Comparing model V1 and H1, we find that internal heating does not increase the temperature inside the slab, consistent with order of magnitude estimates. If the mantle has an internal heating number H=18, equivalent to a heat generation rate of 1.6x10^{-12} W/kg, the temperature of the slab will increase by 10˚C after 250 Myrs. If the chondritic value of heat generation rate (5.1x10^{-12} W/kg) is used instead, the temperature increase will be 32˚C. This temperature increase is negligible. Although we use a uniform H for the mantle and slab, this result suggests that using a larger H for the slab, representing a higher concentration of radioactive elements in the oceanic crust, would not change the slab temperature substantially.

The effect of depth-dependent thermal diffusivity can be significant. From model V1, and K2 to K8, the variation of thermal diffusivity, δ_η, changes from 0 to 7, and the thermal anomalies of slabs decrease as a result. The temperature anomaly of the slab in model K8 is only half of that in model V1, but the slab in model K8 is still 280˚C cooler than surrounding mantle. We conclude that an eightfold or more increase of thermal diffusivity with depth is required to diffusively dissipate the slab before reaching the CMB. The plausible value of δ_κ in the mantle will be discussed in a later section.

In our models, the 660 km phase change fails to halt the slab from sinking to the lower mantle, corroborating earlier work by others [*Christensen*, 1995; *Zhong and Gurnis*, 1995; *van Keken and Ballentine*, 1999]. We find that the slab is not obstructed by the phase change and directly penetrates into the lower mantle, possibly due to the near-vertical dip of the slab in our models. If the trench migrated faster, we would expect to get more time-dependent slab penetration. Although slabs are not halted by the phase change, hot plumes are obstructed from ascending to the upper mantle, at least temporarily [*Davies*, 1995]. Several secondary plumes may form in the upper mantle when the plumes from the CMB collide into the phase boundary and laterally spread out beneath it (Figure 2-4b).

We found there is always a plume on the tip of the slab, independent of changes in plate kinematics, internal heating, and thermal diffusivity. To determine if this phenomenon is a result of our particular initial conditions, we ran another model with a different history. The model has the same material parameters as model P2, except that the plates are stationary for the first 470 Myrs, after which several plumes develop at the CMB and ascend to the surface. Then, the same kinematical history used in P2 is imposed for 250 Myrs. We found that the slab still sinks to the CMB. When the slab slides along the CMB, it sweeps plumes to the edge of the slab, so the slab still has a plume on the edge. This suggests that plume formation on the edge of a slab is not an artifact of our simple initial conditions.

2.3.2 Large-scale Model (3-D)

The plate history in previous 2-D models was simplified considerably from typical subduction systems. In previous models, plate and margin velocities did not change over hundreds of Myrs. These time-invariant boundary conditions give continuous slabs extending from the top surface to the CMB (Animation 2-1; Figure 2-4). However, plate velocities and boundaries change with time [*Atwater,* 1970; *Ben-Avraham and Uyeda,* 1983]. It is possible that continuous slabs are not wound in every subduction zone. In dynamic models with realistic plate histories, it could turn out that continuous slabs are the exception, not the rule. Using a 3-D model with a realistic North America–Pacific plate history, we explore the influence of time-dependent plate velocities and plate boundaries on slab morphology in the lower mantle. We have not attempted to reproduce mantle structure as seen in the tomography by varying either plate history or mantle rheology.

The evolution of model NA5 is shown in Figure 2-6 and Animation 2-2. Since the plate configuration is simple before 85 Ma (similar to the large-scale 2-D models), the slab continuously extends from the surface to mid-mantle (Figure 2-6a). Between 85 and 75 Ma, the convergence angle between the Farallon and North American plates becomes considerably oblique, so the rate of subduction decreases, resulting in a gap in the continuity of the slab in the mid-mantle at 30 Ma (Figure 2-6b). The slab is lying flat underneath the over-riding continental plate. This tendency to become flat lying beneath the continent is

Animation 2-2. The evolution of Model NA5. Blue lines are plate boundaries. Black arrows are plate velocities. White lines are phase boundaries at 410 and 660 km. Two temperature cross-sections at 15˚ and 30˚N are shown. Color scheme: red is warm; blue is cool.

consistent with earlier 2-D calculations [*Zhong and Gurnis*, 1995] and is caused by the strong suction force. This shallowing of dip is partly a consequence of the trench migration to the west and partly a consequence of the decreasing age of the subducting Farallon plate, as the Farallon–Pacific ridge and Farallon–North American margin converge. Eventually, the ridge and trench coalesce [*Atwater*, 1970]. Since subduction terminates at 30˚N after 25 Ma while it continues south of 15˚N, slab structure becomes complex. This complexity is particularly evident along strike at 0 Ma (Figure 2-6c). At 30˚N, the slab is completely detached from the surface, and there is no slab in the upper mantle. However, at 20˚N, the slab is still attached to the surface. The slab thickness changes significantly at different depths and latitudes and has substantial gaps at mid-mantle depths. Other cases (NA1–NA4), with different variants of plate evolution, phase transition strengths, and lower mantle viscosity, all show complex slab structure. We conclude that slabs are not expected to be continuous between the upper and lower mantle, even in the context of whole mantle convection.

2.3.3 Fine-scale Model

Since slabs are associated with large temperature variations, and the viscosity of the hot TBL at the CMB is likely to be small, a model with a high spatial resolution is required to study the long-term evolution of slabs at the CMB. In order to minimize the computational expense, we used fine-scale models (Figure 2-3) of a small physical domain. These models have initial conditions (slab temperature and thickness) adapted from previous 2-D large-scale models, while ignoring the effect of continuing subduction.

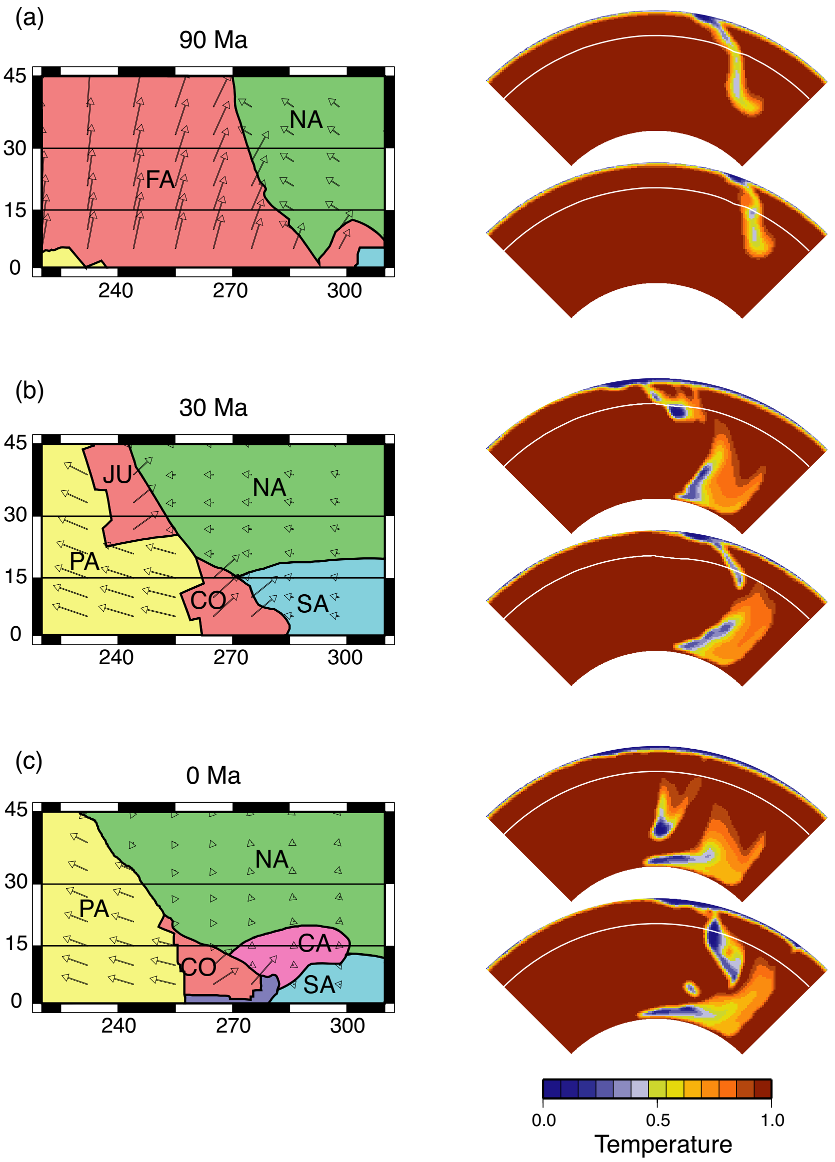

Figure 2-6. Regional spherical models with the evolution of the North American–Pacific–Farallon plate boundary. The white line is the 660 km discontinuity. (a) Left panel shows the plate configuration at 90 Ma. Right panels are the temperature cross-sections at 30˚N (above) and 15˚N (below). (b–c). The same as (a), but at 30 and 0 Ma, respectively. Plate abbreviation: CA: Caribbean; CO: Cocos; FA: Farallon; JU: Juan de Fuca; NA: North America; PA: Pacific; SA: South America.

We start with T_s=0.275, corresponding to a temperature anomaly of 650˚C, and W_s=645 km. In order to explore the parameter space, we independently vary T_s, W_s, and the viscosity

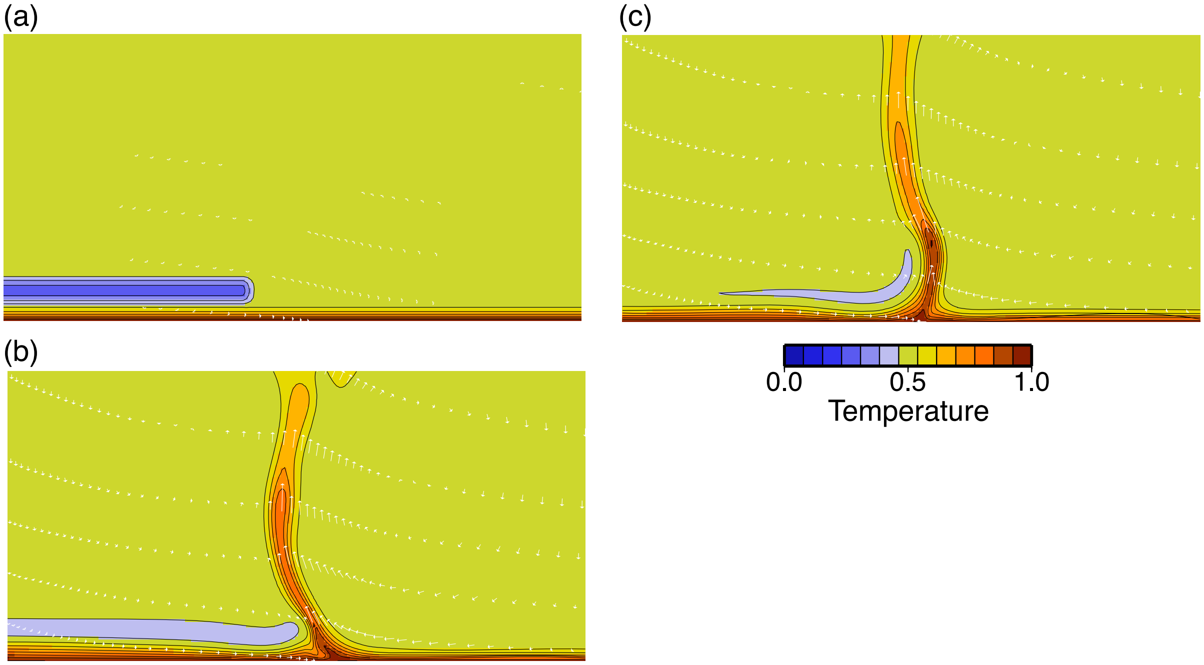

Figure 2-7. Result of model with type-1 outcome (Model F3). (a) Initial condition. (b) As the slab warms, the slab tip sinks, pushing hot materials aside, and essentially blocking the only exit for hot material to escape from beneath the slab. The hot TBL adjacent to the slab thickens while a new plume initiates. The TBL beneath the slab is thicker than the TBL in the slab-free area. (c) The thin slab quickly heats, diffuses away, and fails to keep the TBL beneath from being drained. The TBL has uniform thickness after the slab disappears.

contrast between the slab and mantle, δ_η. We define two auxiliary parameters, the initial negative buoyancy and the initial stiffness of the slab, B_s and S as

$$B_s = -\iint_{\text{slab}} (T\text{-}T_m)\ \mathrm{dV} \quad \text{at } t = 0 \tag{4-11}$$

$$S = \iint_{\text{slab}} \log(\eta)\ \mathrm{dV} \quad \text{at } t = 0 \tag{4-12}$$

We find three model outcomes. 1) For thin and less stiff slabs, slabs will heat and dissipate quickly (Animation 2-3, Figure 2-7). 2) For thick and stiff slabs, mega-plumes, with unusually large buoyancies, form beneath slabs (Animation 2-4, Figure 2-8). 3) For moderately thick and less stiff slabs, plumes with normal buoyancy form beneath slabs. (This third type is essentially a transition between the first two.) We are able to distinguish these outcomes by measuring the eruption time, t_e (defined later), and the plume buoyancy at eruption, $B_e=B(t_e)$. The plume buoyancy is defined as

$$B(t)=\iint_{T>T_m}(T\text{-}T_m)\mathrm{dV} \qquad (4\text{-}13)$$

This integral is carried out within a small region near the center of the slab (i.e., left margin of the domain) to avoid contamination from the bottom TBL and plumes in the slab-free area. t_e is the time when the plume buoyancy reaches the maximum. B_e, then, is the maximum plume buoyancy. The results of fine-scale models are listed in Table 2-7.

The demarcation between these outcomes becomes evident when we look at B_e and t_e in the space of B_s and S (Figure 2-9). The transition between type-1 and -2 outcomes is roughly delineated by a single line (dashed line in Figure 2-9). The buoyancy of the mega-plume, B_e, and the eruption time of the mega-plume, t_e, are generally positively correlated, i.e., longer eruption times lead to larger plumes. The general trend is for slabs with larger B_s and S (resulting from colder and thicker slabs, and larger δ_η and thicker slabs, respectively) to lead to larger plumes erupting after longer times. The initial slab stiffness, S, is the major limiting factor since this transition boundary is elongate along the B_s axis. An explanation will be provided below. When B_s and S are both small, the behavior is complex, and no clear

Animation 2-3. The evolution of Model F3. The thin slab is heated by the surrounding mantle and diffuses away. Color scheme: red is warm; blue is cool.

Animation 2-4. The evolution of Model F10. Upper panel: red line is the evolution of the plume buoyancy inside the black box, while blue line is the evolution of the negative slab buoyancy. Lower panel: the thick slab can trap a large amount of hot mantle beneath and lead to mega-plume formation. Color scheme: red is warm; blue is cool.

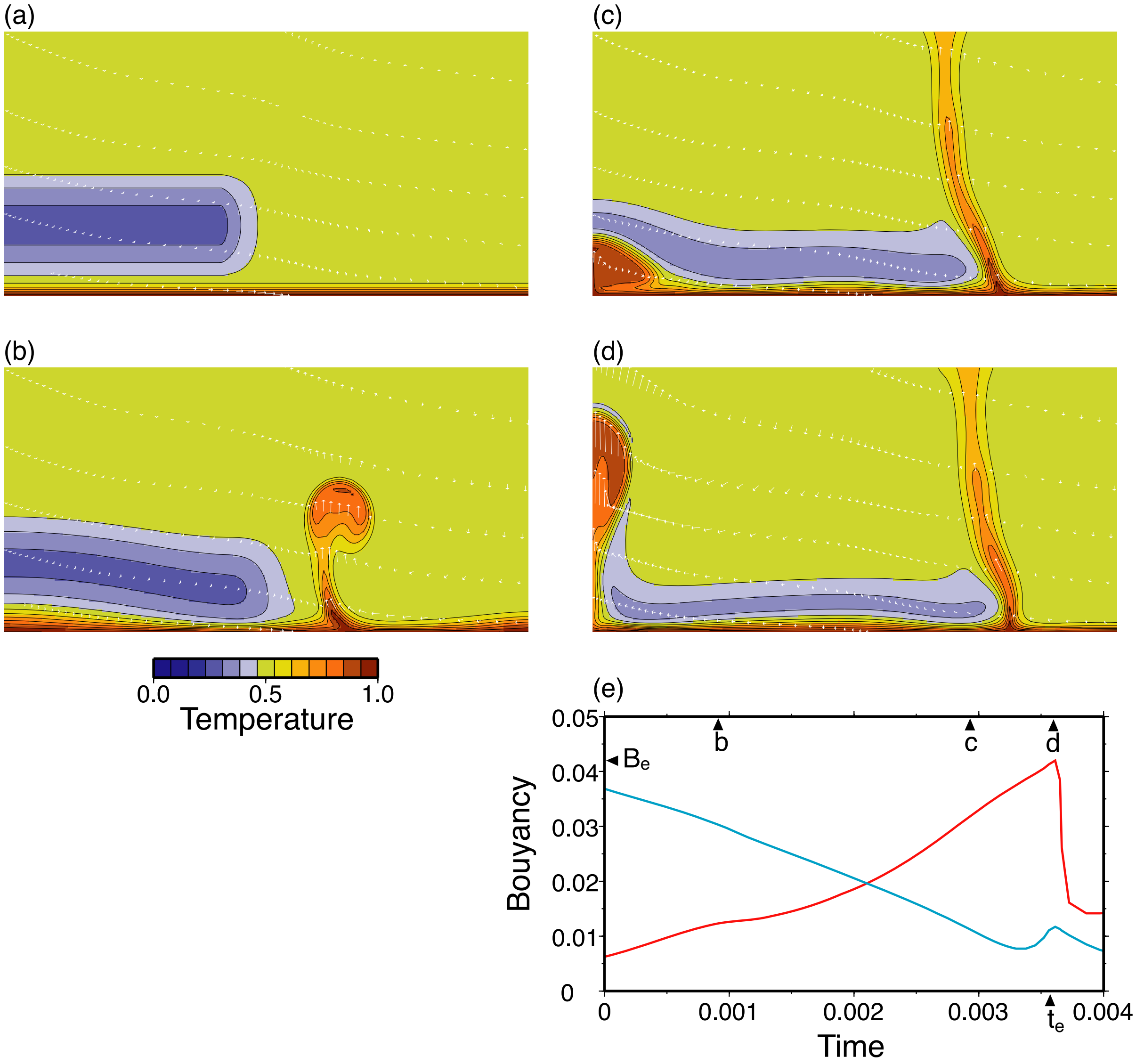

Figure 2-8. Result of model with type-2 outcome (Model F10). (a) Initial condition. (b–d) snapshots of temperature and velocity fields. (e) The buoyancy evolution of the slab and mega-plume. Blue line represents the negative buoyancy of the slab, while the red dashed line represents the positive buoyancy of the hot material. The time of frame (b), (c), and (d) is indicated. The eruption time, t_e, of the mega-plume is when the buoyancy of the hot material reaches its maximum, B_e.

boundary can be delineated.

The dynamics of models with type-1 outcomes are considered first. In these models, as a slab warms, its viscosity decreases, and it deforms more easily. The slab starts to spread out, pushes the hot materials aside, and, essentially, its tip blocks the only exit for hot material to escape from beneath the slab. The importance of this blockage will soon become evident. The hot TBL adjacent to the slab is thickened and initiates a plume. For convenience, we will call it an *ordinary plume*. This plume head ascends through the mantle and is fed by a thin conduit, which continuously drains the hot mantle near the CMB. The TBL in the slab-free area thins as a result. The TBL beneath the slab is blocked and is not drained by the plume conduit, so it is thicker than the TBL in the slab-free area at this stage (Figure 2-7b). The thin slab quickly heats, diffuses away, and fails to keep the TBL beneath from being drained. The TBL has uniform thickness after the slab disappears (Figure 2-7c).

We now consider the dynamics of models that have type-2 outcomes. During the early stage of these models, the dynamics are the same as type-1 outcomes (Figure 2-8a and 2-8b). However, the thicker slab survives longer so that a substantial amount of hot mantle has become trapped. With this trapped hot mantle, convection beneath the slab becomes vigorous (Figure 2-8c). When the trapped mantle accumulates enough buoyancy, it lifts, tilts, and finally breaks through the slab (Figure 2-8d). This plume can have a buoyancy three times larger than an ordinary plume, hence our term, *mega-plume*. The buoyancy evolution of the slab and mega-plume is plotted in Figure 2-8e. The buoyancy of the mega-plume increases with time at the expense of the negative buoyancy of the slab. We note here that most of the reheated slab material becomes incorporated into the mega-plume. The geochemical significance of this will be considered later. When the mega-plume erupts, B_e is six times larger than the negative buoyancy of the remnant slab. This disproportionality suggests that the trapped mega-plume is the result of high slab viscosity, not of high slab density. The sudden increase of the plume’s vertical velocity when it escapes the domain, as clearly seen

Table 2-7. Results of fine-scale models.

Model	**F1**	**F2**	**F3**	**F4**	**F5**	**F6**
W_s (km)	645	332	161	1000	645	645
T_s	0.275	0.275	0.275	0.275	0.431	0.155
δ_η	3	3	3	3	3	3
B_s	0.031	0.015	0.011	0.048	0.009	0.048
S	0.943	0.469	0.233	1.464	0.941	0.944
B_e	0.058	0.040	-	0.082	0.050	0.056
t_e	0.0064	0.0033	-	0.0098	0.0068	0.0064

Model	**F7**	**F8**	**F9**	**F10**	**F11**	**F12**
W_s (km)	332	161	322	645	332	161
T_s	0.431	0.431	0.215	0.275	0.275	0.275
δ_η	3	3	3	2	2	2
B_s	0.005	0.002	0.019	0.031	0.015	0.011
S	0.132	0.700	0.470	0.629	0.313	0.156
B_e	0.048	0.039	0.039	0.042	0.028	-
t_e	0.0028	0.0033	0.0035	0.0037	0.0032	-

Model	**F13**	**F14**	**F15**	**F16**	**F17**	**F18**
W_s (km)	1000	645	645	332	161	322
T_s	0.275	0.431	0.155	0.431	0.431	0.215
δ_η	2	2	2	2	2	2
B_s	0.048	0.009	0.048	0.005	0.002	0.019
S	1.976	0.626	0.629	0.085	0.047	0.314
B_e	0.050	0.056	0.028	0.038	0.044	-
t_e	0.0047	0.0038	0.0038	0.0023	0.0024	-

in Animation 2-4, is an artifact of the boundary condition, because the plume encounters no viscous resistance as it reaches the top boundary. However, this phenomenon occurs after the plume has erupted and moved away from the slab, so there is no evidence that the permeable boundary condition interferes with pre-eruption plume growth.

In models with type-3 outcomes, slabs also traps hot mantle beneath, but plumes breaking through slabs have similar buoyancies to ordinary plumes. These models have larger t_e than some models with type-2 outcomes, indicating that the smaller plumes are not resulting from insufficient time to develop, but from the inability of weaker slabs to hold large plume buoyancies down. We conclude that weak slabs cannot trap sufficient hot mantle before being drained by neighboring normal plumes.

We offer an explanation as to why slab viscosity, or stiffness, is a major factor in determining the plume buoyancy. The small-scale convection beneath slabs is actually akin to stagnant-lid convection. Stagnant-lid convection has a cold, effectively stagnant lid on the top of the convection cell due to the very large viscosity contrast between the lid and convection cell. Numerical study using Newtonian viscosity shows that stagnant-lid convection occurs when the viscosity contrast, $\Delta\eta$, exceeds 10^4 [*Solomatov*, 1995], and $\Delta\eta$ in our models is 10^5–10^6. In stagnant-lid convection, the non-dimensional temperature at the core of the convection cell is $1-1/ln(\Delta\eta)$ and is independent on the size of the cell. An examination of the temperature of the convection cells at different times in different models confirms this prediction. Since buoyancy is proportional to temperature and volume, and temperature is a constant, when the convection cell erupts, the plume buoyancy is solely determined by the size of the plume (essentially the plume head since the volume of the conduit is small). *Davies* [1993] used a simple calculation to estimate the radius of a plume head, a, when it rises from a low viscosity basal layer. He found that $a=(\eta_a/\eta_b)^{1/3}h$, where η_a is the viscosity of the ambient fluid, η_b is the viscosity of the basal layer, and h is the thickness of the basal layer. So the volume of the plume head is $\pi h^2(\eta_a/\eta_b)^{2/3}$. In our models, h and η_b are the height and viscosity of the convection cell, which are more or less constant. So η_a, the viscosity of the overlying slab, controls the volume of the plume head, hence the plume buoyancy at eruption. Ordinary plumes are overlain by the mantle, which has a constant viscosity, and have constant buoyancy in all models as a result. The two models

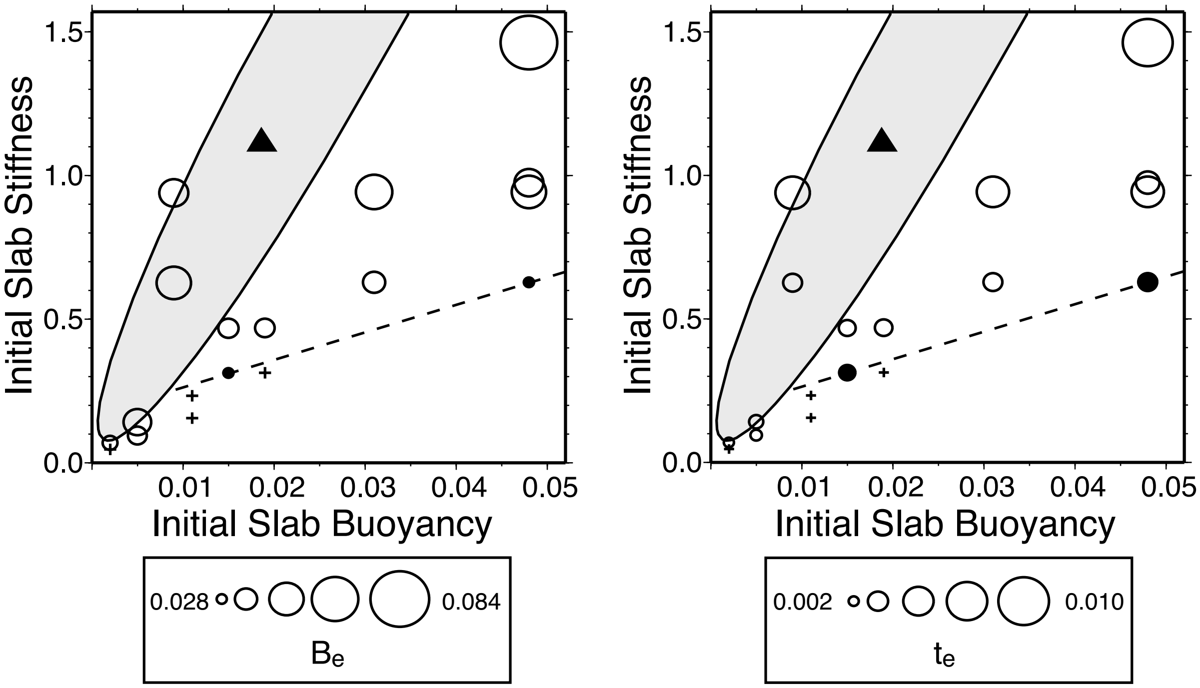

Figure 2-9. Summary of fine-scale models. Crosses denote models with type-1 outcomes, unfilled circles denote type-2, while solid circles denote type-3. The radii of the circles are proportional to B_e in the left panel and to t_e in the right panel. The transition between type-1 and -2 outcomes is delineated by the dashed line. The solid triangle indicates our best estimate for plausible slab conditions within the mantle, while the shaded ellipse indicates the uncertainty of our estimate.

with type-3 outcomes have slab viscosities comparable to ambient mantle when plumes erupt from beneath a slab, so the plume buoyancy is the same as ordinary plumes.

We summarize three important features of the dynamics of fine-scale models: a) Plumes preferentially develop on the edge and center of the slab; b) The TBL in the slab-free area is thinner than that beneath the slab, as a result of frequent plume formation and eruption in the slab-free area; and c) In models with type-2 outcomes, substantial amounts of hot material can be trapped beneath the slab, leading to mega-plume formation over long periods of time.

Slabs could also have a substantial influence on the heat flux between the mantle and core. For example, the CMB heat flux of model F10 as a function of time and space is shown

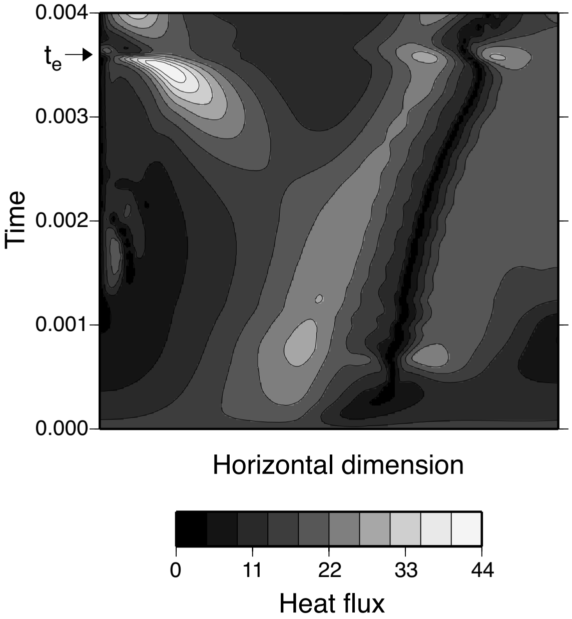

Figure 2-10. The non-dimensional heat flux at the CMB of model F10 as a function of time and horizontal dimension. The eruption time of a mega-plume is also indicated.

in Figure 2-10. The dark red strip on the central right marks the root of an ordinary plume. Near the left margin, the transition from dark red to bright yellow as a function of time corresponds to the transition from pure conduction (Figure 2-8b) to small-scale convection (Figure 2-8c) beneath the slab. The small-scale convection is so vigorous that the cold material is entrained into the bottom of the convection cell and gives a very high heat flux. Just before t_e, the heat flux in this region reaches the maximum and is twice as high as compared with the heat flux in the slab-free area at any time. After t_e, the convection cell erupts as a mega-plume, and the heat flux suddenly returns to the normal value. This shows that the heat flux variation associated with a mega-plume eruption can be very localized in space and abrupt in time, and is substantially larger than those occurring at a normal TBL. All models with type-2 outcomes exhibited these same heat flow characteristics.

2.4 Discussion

Using models with a high-viscosity lower mantle, a phase transition at 660 km depth, depth-dependent thermal expansivity, and depth-dependent thermal diffusivity, we have shown that slabs always descend to and then come to rest on the CMB. However, by incorporating viable models for evolving plate motions in regional spherical models, we find that although slabs are expected to reach the CMB, they will not necessarily be continuous between the upper and lower mantle. Large gaps in the continuity of slabs are expected as a function of both mantle depth and distance along plate margins because of the time-dependence of plate velocities and plate boundaries. The interaction between slabs and the basal TBL was further investigated by using fine-scale models, and we found this interaction would result in two types of plumes. One, called an ordinary plume, develops on the edge of the slab, drains material from the TBL, and has relatively small buoyancy. The second, called a mega-plume, develops beneath the center of ancient slabs, drains material from recycled slabs, and has relatively large buoyancy. These two types of plumes are significantly different in their location, eruption buoyancy, and geochemical signatures.

It has been suggested that enhanced thermal conductivity will cause slabs to rapidly disappear in the deep mantle. However, even in a model with thermal diffusivity increasing eightfold with depth, the slab still reaches the CMB with a significant temperature anomaly. Is a greater increase in thermal diffusivity with depth possible? To estimate the variation in thermal diffusivity, $\kappa=k/\rho C_p$, we need to determine the variation in thermal conductivity, k, density, ρ, and specific heat at constant pressure, C_p, across the mantle. A model of thermal conductivity of the mantle is given by *Hofmeister* [1999], which varies from 2 to 6.7 W/m·K from the top to the bottom of the mantle. The density of the mantle increases from 3500 kg/m^3 to 5500 kg/m^3, according to PREM. Specific heat at constant pressure, C_p, is related to specific heat at constant volume, C_v, via $C_p=C_v(1+\gamma\alpha T)$, where γ is Grüneisen ratio, α is thermal expansivity, and T is absolute temperature. When T is large, according to the rule of Dulong and Petit, C_v approaches to $3R/m$, where R is the gas constant, and m is mean atomic weight of the mineral. Using γ =1.2, T= ~1500 to ~4000 K, α=2x10^{-5} K^{-1}, and m=0.02 kg/mol, we find C_p changes from 1.3 kJ/kg·K to 1.4 kJ/kg·K. The estimated C_p is compatible with the more rigorous approach of *Akaogi and Ito* [1993b], but they did not extend their calculation to lower mantle conditions. By combining these results, κ has a range of 1.1–2.2x10^{-6} m^2/s. Although our estimate is subject to a large uncertainty, it does not seem possible to have κ increasing by a factor of 8. So we conclude that thermal diffusion cannot dissipate slabs before they reach the CMB.

At some subduction zones, high seismic velocity anomalies are only found in the upper mantle and deep mantle, but not in the mid-mantle (for example, southern Kuril and India). These gaps in the mid-mantle are often taken as evidence that slabs dissipate before reaching the CMB, disregarding the low resolution of tomography in the mid-mantle. However, we have demonstrated that slabs could be discontinuous when plate velocities are time-dependent. These gaps of slabs in the mid-mantle might result from an abrupt change in plate velocities, i.e., a plate reorganization event [*Fukao et al.*, 2001]. Moreover, changes in convergence history are also likely to play an important role. Examples include the interruption in plate convergence along the Pacific–North America boundary (Figure 2-6) or the post-Mesozoic reinitiation of subduction that occurred for the Tonga–Kermadec system [*Gurnis et al.*, 2000].

In our 2-D models, the subduction angles are always near vertical, and slabs penetrate the 660 km discontinuity directly. A slab with a shallower subduction angle, resulting from more rapid trench rollback, might become temporarily trapped in the transition zone [*Zhong and Gurnis*, 1995; *Christensen*, 1996; *Ita and King*, 1998]. However, once a slab penetrates the 660 km discontinuity, we find no compelling physical reason why it would not descend to the CMB. The possibility that slabs might be stopped by a change in chemistry or mineralogy cannot be excluded [*Kesson et al.*, 1998; *Kellogg et al.*, 1999].

When slabs reach the CMB, they will have a substantial influence on the dynamics at the CMB. The most pronounced effect is for plumes to be swept onto the edges of slabs. One piece of evidence supporting this possibility is that hotspots correlate with the boundary between high and low seismic velocity regions as determined with tomography at the CMB [*Thorne et al.*, 2001]. Furthermore, *Ni and Helmberger* [2001] and *Luo et al.* [2001] found ULVZs near sharp transitions between high and low seismic velocities beneath the South Atlantic and central Pacific. Taken together with a putative link between ULVZ and upwellings [*Williams et al.*, 1998], we suggest that the ULVZs occurring near the high-to-low seismic velocity transitions are a manifestation of ordinary plumes. Because plumes preferentially develop at the edge of slabs, and plumes may give rise to ULVZs, ULVZs are observed at the edge of slabs. However, we cannot overlook the possibility that, although 2-D models always have plumes at slab edges, plumes are more likely to be irregularly distributed around the edges of slabs in 3-D.

Another important effect of slabs at the CMB is their modulation of core-mantle heat flux. The thermal conditions at the CMB are likely to have an important influence on the geodynamo [*Zhang and Gubbins*, 1993; *Glatzmaier et al.*, 1999; *Gibbons and Gubbins*, 2000], though a consensus of whether and how the heat flux variation would affect the geodynamo is not established. *Larson and Olson* [1991] proposed that nearly simultaneous eruptions of several very large plumes from the CMB were responsible for the decrease of magnetic reversal frequency during the Cretaceous. The dramatically enhanced heat flux at the CMB before the formation of mega-plumes provides a viable mechanism to change the magnetic reversal frequency. Additionally, the large buoyancy of mega-plumes in our models is consistent with a huge production of basaltic crust during the mid-Cretaceous. These seem to support Larson and Olson's hypothesis. However, with our models, the onset of increased crustal production is likely to lag plume eruption by several tens of million years, due to the time it takes for plumes to rise through the mantle.

The result of fine-scale models showed that those with type-2 outcomes (e.g., mega-plume eruption) occupy a large part of the B_s-S domain (Figure 2-9). It is natural to ask where the Earth may lie in this space. To answer this question, we need to estimate the possible thickness and temperature anomalies associated with slabs at the CMB. Although we determined a range of thicknesses (~450 to ~650 km) and temperature anomalies (~300˚ to ~600˚C) from our models, we would like to ground our estimate with seismology. An estimate of temperature anomalies of slabs can be obtained from tomography models. Several recent tomography models have RMS-velocity variations δlnV_p=0.3% and δlnV_s=0.6% over most parts of lower mantle [*Fukao et al.,* 2001]. Recent molecular dynamics simulation on $MgSiO_3$ perovskite leads to $(\partial lnV_p/\partial T)_p$=-1.98x$10^{-5}$ K^{-1} and $(\partial lnV_s/\partial T)_p$=-3.78x$10^{-5}$ K^{-1} at a depth of 2000 km [*Oganov et al.,* 2001]. Therefore, such an RMS-velocity variation would correspond to an RMS-temperature variation of 150˚C. The temperature anomalies in the center of slabs would be much higher than the RMS value, so

150˚C gives a lower bound. The regional tomography model in the lowermost mantle beneath the southwestern Pacific from *Wysession* [1996] has a maximum δlnV_p=4%, which is a fairly large velocity variation among tomography models. If we attribute all of the variation to a thermal origin, we get a temperature anomaly of 1000˚C as an upper bound. The thickness of slabs cannot be inferred from seismology because tomography tends to smooth mantle structure. A rough estimate of 200–700 km is used here. Assuming an activation energy of 520 kJ/mol·K and an ambient temperature of 2000 K, the viscosity variation is estimated to be δ_η=1.1~13.6. We mark the range of our estimate as the shaded area in Figure 2-9. Also plotted is the mid-point of our estimate (temperature anomaly 550˚C and thickness 450 km). The shaded area lies almost entirely within the mega-plume regime, suggesting that mega-plumes are relevant to Earth.

If mega-plumes had occurred in the past, what kind of signature would they have left? Because of their large buoyancies, mega-plumes are likely to penetrate the 660 km discontinuity, reach the surface, and produce hotspots. Since most recycled slab material is incorporated into mega-plumes, we suggest that mega-plumes could be the source of HIMU OIB. The slab would provide a crustal component to the mega-plume while being stiff enough to hold the buoyant plume at the CMB for a long interval of time. It is an efficient way to keep enriched crustal material from mixing with depleted mantle. We suggest that HIMU hotspots may be found above ancient slabs. This implication is difficult to test since slabs under HIMU hotspots might have been thermally dissipated after nucleating a mega-plume.

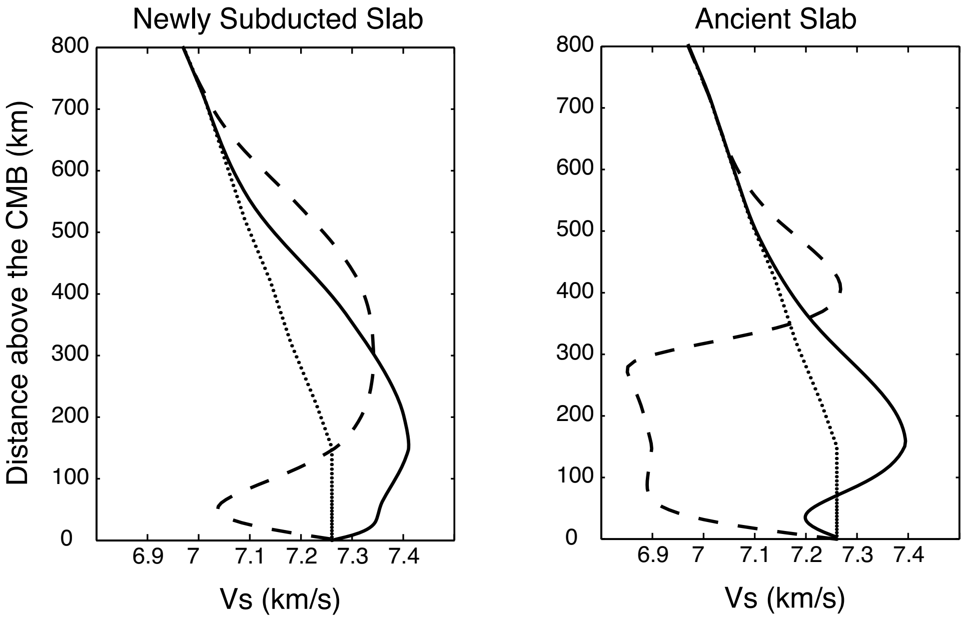

Figure 2-11. Shear wave velocity profiles above the CMB. Left panel shows profiles from a newly subducted slab (Figure 2-8b), while right panel shows profiles from an ancient slab (Figure 2-8c). Dashed lines indicate profiles taken at the center of slabs, while solid lines indicate profiles taken at the edge of slabs. The dotted line is PREM.

On the other hand, if mega-plumes are developing on the CMB today, could we find their signatures? Using a thermal profile from a slab-free area as a reference, we convert thermal profiles to shear wave velocity at the center and edge of slabs of different ages (Figure 2-11). This conversion is based on temperatures variation only, without including the possible influence of partial melting and variations in chemistry. The thermal structures of slabs produce high seismic velocity anomalies capping low velocity anomalies The extent of low velocity anomaly changes substantially with slab location and age. The low velocity anomaly is more profound beneath the center of a slab than beneath a slab edge. An ancient slab is expected to cap a larger low velocity anomaly than a newly subducted slab. The signature of this low velocity anomaly is likely to be compensated by the surrounding high velocity anomalies. This structure is essentially two-dimensional and may be hidden in previous 1D

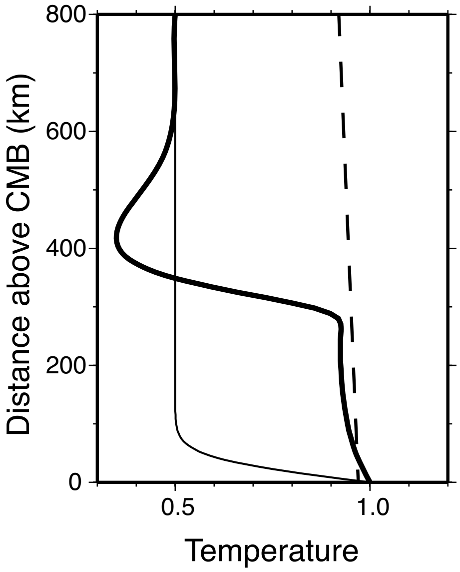

Figure 2-12. Temperature profiles across the slab (thick line) and across the slab-free area (thin line) along with a hypothetical solidus (dashed line).

studies of D’’. Substantial low velocity anomalies are expected beneath the large volume, seismically fast structures at the CMB. The differential travel time of *S* and *ScS* at large epicenter distance (70° to 90°) might be used to detect these regions.

Another possible signature of a developing mega-plume is a ULVZ within the geographic center of a slab. We show temperature profiles across slab and slab-free areas and a hypothetical solidus (Figure 2-12). If the solidus intersects the geotherm, following the suggestion that ULVZs result from presence of partial melting [*Williams and Garnero*, 1996], our model predicts that a larger degree of partial melting could occur under ancient slabs, and by implication ULVZs could be larger under old slabs.

The CMB regions beneath the Siberia and the Caribbean, which have strong high seismic velocity anomalies and a long subduction history, are the most likely places to find developing mega-plumes. The anomalous structure beneath Central America [*Fisher and*

Wysession, 2001; *Wysession et al.*, 2001] is a possible candidate in this regard. We suggest a detailed study on these regions to test our predictions.

References

Akaogi, M., and E. Ito, (1993a) Refinement of enthalpy measurement of MgSiO3 perovskite and negative pressure-temperature slopes for perovskite-forming reactions, *Geophys. Res. Lett.*, *20*, 1839–1842.

Akaogi, M., and E. Ito (1993b), Heat-capacity of MgSiO3 perovskite, *Geophys. Res. Lett.*, *20*, 105–108.

Atwater, T. (1970), Implications of plate tectonics for the Cenozoic tectonic evolution of western North America, *Geol. Soc. Am. Bull.*, *81*, 3513–3536.

Atwater, T., and J. Stock (1998), Pacific North America plate tectonics of the Neogene southwestern United States: An update, *Int. Geol. Rev.*, *40*, 375–402.

Ben-Avraham, Z., and S. Uyeda (1983), Entrapment origin of marginal seas, in *Geodynamics of the Western Pacific–Indonesian Region*, edited by T. W. C. Hilde, et al., pp. 91–104, AGU, Washington DC.

Chopelas, A. (1996), Thermal expansivity of lower mantle phases MgO and MgSiO3 perovskite at high pressure derived from vibrational spectroscopy, *Phys. Earth Planet. Inter.*, *98*, 3–15.

Christensen, U. (1995), Effects of phase-transitions on mantle convection, *Annu. Rev. Earth Planet. Sci.*, *23*, 65–87.

Christensen, U. R. (1996), The influence of trench migration on slab penetration into the lower mantle, *Earth Planet. Sci. Lett.*, *140*, 27–39.

Creager, K. C., and T. H. Jordan (1986), Slab penetration into the lower mantle beneath the Mariana and other island arcs of the northwest Pacific, *J. Geophys. Res.*, *91*, 3573–3589.

Davies, G. F. (1989), Effect of a low viscosity layer on long-wavelength topography, upper mantle case, *Geophys. Res. Lett.*, *16*, 625–628.

Davies, G. F. (1993), Cooling the core and mantle by plume and plate flows, *Geophys. J. Int.*, *115*, 132–146.

Davies, G. F. (1995), Penetration of plates and plumes through the mantle transition zone, *Earth Planet. Sci. Lett.*, *133*, 507–516.

Ding, X. Y., and S. P. Grand (1994), Seismic structure of the deep Kurile subduction zone, *J. Geophys. Res.*, *99*, 23767–23786.

Dziewonski, A. M., and D. L. Anderson, Preliminary reference earth model, *Phys. Earth Planet. Inter.*, *25*, 297–356.

Fischer, K. M., K. C. Creager, and T. H. Jordan (1991), Mapping the Tonga slab, *J. Geophys. Res., 96,* 14403–14427.

Fisher, J. L., and M. E. Wysession (2001), Small scale seismic attenuation within D", *Eos Trans. AGU, 82,* Fall Meet. Suppl., Abstract T21A-0849.

Fukao, Y., S. Widiyantoro, and M. Obayashi (2001), Stagnant slabs in the upper and lower mantle transition region, *Rev. Geophys., 39,* 291–323.

Garnero, E. J., and D. V. Helmberger (1996), Seismic detection of a thin laterally varying boundary layer at the base of the mantle beneath the central-Pacific, *Geophys. Res. Lett., 23,* 977–980.

Gibbons, S. J., and D. Gubbins (2000), Convection in the Earth's core driven by lateral variations in the core-mantle boundary heat flux, *Geophys. J. Int., 142,* 631–642.

Glatzmaier, G. A., R. S. Coe, L. Hongre, and P. H. Roberts (1999), The role of the Earth's mantle in controlling the frequency of geomagnetic reversals, *Nature, 401,* 885–890.

Grand, S. P., R. D. van der Hilst, and S. Widiyantoro (1997), Global seismic tomography: a snapshot of convection in the Earth, *GSA Today, 7,* 1–7.

Gurnis, M., J. Ritsema, H. J. van Heijst, and S. Zhong (2000), Tonga slab deformation: The influence of a lower mantle upwelling on a slab in a young subduction zone, *Geophys. Res. Lett., 27,* 2373–2376.

Hager, B. H. (1984), Subducted slabs and the geoid - constraints on mantle rheology and flow, *J. Geophys. Res., 89,* 6003–6015.

Hager, B. H., R. W. Clayton, M. A. Richards, R. P. Comer, and A. M. Dziewonski (1985), Lower mantle heterogeneity, dynamic topography and the geoid, *Nature, 313,* 541–546.

Hauck, S. A., R. J. Phillips, and A. M. Hofmeister (1999), Variable conductivity: Effects on the thermal structure of subducting slabs, *Geophys. Res. Lett., 26,* 3257–3260.

Hofmann, A. W. (1997), Mantle geochemistry: The message from oceanic volcanism, *Nature, 385,* 219–229.

Hofmann, A. W., and W. M. White (1982), Mantle plumes from ancient oceanic crust, *Earth Planet. Sci. Lett., 57,* 421–436.

Hofmeister, A. M. (1999), Mantle values of thermal conductivity and the geotherm from phonon lifetimes, *Science, 283,* 1699–1706.

Ita, J., and S. D. King (1998), The influence of thermodynamic formulation on simulations of subduction zone geometry and history, *Geophys. Res. Lett., 25,* 1463–1466.

Ito, E., and E. Takahashi (1989), Postspinel transformations in the system Mg2SiO4-Fe2SiO4 and some geophysical implications, *J. Geophys. Res.*, *94*, 10637–10646.

Kellogg, L. H., B. H. Hager, and R. D. van der Hilst (1999), Compositional stratification in the deep mantle, *Science*, *283*, 1881–1884.

Kesson, S. E., J. D. F. Gerald, and J. M. Shelley (1998), Mineralogy and dynamics of a pyrolite lower mantle, *Nature*, *393*, 252–255.

King, S. D., A. Raefsky, and B. H. Hager (1990), Conman - vectorizing a finite-element code for incompressible 2-dimensional convection in the Earth's mantle, *Phys. Earth Planet. Inter.*, *59*, 195–207.

Lambeck, K., C. Smither, and P. Johnston (1998), Sea-level change, glacial rebound and mantle viscosity for northern Europe, *Geophys. J. Int.*, *134*, 102–144.

Larson, R. L., and P. Olson (1991), Mantle plumes control magnetic reversal frequency, *Earth Planet. Sci. Lett.*, *107*, 437–447.

Lenardic, A., and W. M. Kaula (1994), Tectonic plates, D’’ thermal structure, and the nature of mantle plumes, *J. Geophys. Res.*, *99*, 15697–15708.

Lithgow-Bertelloni, C., and M. A. Richards (1998), The dynamics of Cenozoic and Mesozoic plate motions, *Rev. Geophys.*, *36*, 27–78.

Lowman, J. P., and G. T. Jarvis (1996), Continental collisions in wide aspect ratio and high Rayleigh number two-dimensional mantle convection models, *J. Geophys. Res.*, *101*, 25485–25497.

Luo, S. N., S. D. Ni, and D. V. Helmberger (2001), Evidence for a sharp lateral variation of velocity at the core-mantle boundary from multipathed PKPab, *Earth Planet. Sci. Lett.*, *189*, 155–164.

Megnin, C., and B. Romanowicz (2000), The three-dimensional shear velocity structure of the mantle from the inversion of body, surface and higher-mode waveforms, *Geophys. J. Int.*, *143*, 709–728.

Mitrovica, J. X., and A. M. Forte (1997), Radial profile of mantle viscosity: Results from the joint inversion of convection and postglacial rebound observables, *J. Geophys. Res.*, *102*, 2751–2769.

Moresi, L., M. Gurnis, and S. Zhong (2000), Plate tectonics and convection in the Earth's mantle: Toward a numerical simulation, *Comput. Sci. Eng.*, *2*, 22–33.

Ni, S. D., and D. V. Helmberger (2001), Horizontal transition from fast to slow structures at the core- mantle boundary; South Atlantic, *Earth Planet. Sci. Lett.*, *187*, 301–310.

Oganov, A. R., J. P. Brodholt, and G. D. Price (2001), The elastic constants of MgSiO3 perovskite at pressures and temperatures of the Earth's mantle, *Nature*, *411*, 934–937.

Pankow, K. L., and T. Lay (1999), Constraints on the Kurile slab from shear wave residual sphere analysis, *J. Geophys. Res.*, *104*, 7255–7278.

Richards, M. A., and D. C. Engebretson (1992), Large-scale mantle convection and the history of subduction, *Nature*, *355*, 437–440.

Ritsema, J., and H. van Heijst (2000), Seismic imaging of structural heterogeneity in Earth's mantle: evidence for large-scale mantle flow, *Sci. Progress*, *83*, 243–259.

Shearer, P. M., and M. P. Flanagan (1999), Seismic velocity and density jumps across the 410- and 660-kilometer discontinuities, *Science*, *285*, 1545–1548.

Sidorin, I., and M. Gurnis (1998), Geodynamically consistent seismic velocity predictions at the base of the mantle, in *The Core-mantle Boundary Region*, edited by M. Gurnis, et al., pp. 209–230, AGU, Washington DC.

Sidorin, I., M. Gurnis, and D. V. Helmberger (1999), Dynamics of a phase change at the base of the mantle consistent with seismological observations, *J. Geophys. Res.*, *104*, 15005–15023.

Solomatov, V. S. (1995), Scaling of temperature-dependent and stress-dependent viscosity convection, *Phys. Fluids*, *7*, 266–274.

Thorne, M. S., E. J. Garnero, and S. P. Grand (2001), Seismic evidence for strong chemical heterogeneity at the core mantle boundary as the source of hot spot volcanism, *Eos Trans. AGU*, *82*, Fall Meet. Suppl., Abstract T12E-12.

van der Hilst, R. D., S. Widiyantoro, and E. R. Engdahl (1997), Evidence for deep mantle circulation from global tomography, *Nature*, *386*, 578–584.

van Keken, P. E., and C. J. Ballentine (1999), Dynamical models of mantle volatile evolution and the role of phase transitions and temperature-dependent rheology, *J. Geophys. Res.*, *104*, 7137–7151.

Vidale, J. E., and M. A. H. Hedlin (1998), Evidence for partial melt at the core-mantle boundary north Tonga from the strong scattering of seismic waves, *Nature*, *391*, 682–685.

Wang, Y. B., D. J. Weidner, R. C. Liebermann, and Y. S. Zhao (1994), P-V-T equation of state of (Mg,Fe)SiO3 perovskite - constraints on composition of the lower mantle, *Phys. Earth Planet. Inter.*, *83*, 13–40.

Weinstein, S. A., P. L. Olson, and D. A. Yuen (1989), Time-dependent large aspect-ratio convection in the Earth’s mantle, *Geophys. Astrophys. Fluid. Dyn.*, *47*, 157–197.

Williams, Q., and E. J. Garnero (1996), Seismic evidence for partial melt at the base of Earth's mantle, *Science*, *273*, 1528–1530.

Williams, Q., J. Revenaugh, and E. Garnero (1998), A correlation between ultra-low basal velocities in the mantle and hot spots, *Science*, *281*, 546–549.

Wysession, M. E. (1996), Imaging cold rock at the base of the mantle: The sometimes fate of slabs?, in *Subduction: Top to bottom*, edited by B. G. E., AGU, Washington DC.

Wysession, M. E., K. M. Fischer, G. I. Al-eqabi, P. J. Shore, and I. Gurari (2001), Using MOMA broadband array ScS-S data to image smaller-scale structures at the base of the mantle, *Geophys. Res. Lett.*, *28*, 867–870.

Zhang, K., and D. Gubbins (1993), Convection in a rotating spherical fluid shell with an inhomogeneous temperature boundary-condition at infinite Prandtl number, *J. Fluid Mech.*, *250*, 209–232.

Zhong, S., and M. Gurnis (1995), Mantle convection with plates and mobile, faulted plate margins, *Science*, *267*, 838–843.

Zhong, S., and M. Gurnis (1997), Dynamic interaction between tectonics plates, subducting slabs, and the mantle, *Earth Interaction*, *1*, 1–18.

Chapter 3

Coupling multiple models of mantle convection within a computational framework

In press in *Geochemistry, Geophysics, Geosystems* (2006) by Eh Tan, Eun-seo Choi, Pururav Thoutireddy, Michael Gurnis, and Michael Aivazis, **7**, doi: 10.1029/2005GC001155.

Abstract

Solver coupling can extend the capability of existing modeling software and provide a new venue to address previously intractable problems. A software package has been developed to couple geophysical solvers, demonstrating a method to accurately and efficiently solve multi-scale geophysical problems with reengineered software using a computational framework (Pyre). Pyre is a modeling framework capable of handling all aspects of the specification and launch of numerical investigations. We restructured and ported CitcomS, a finite element code for mantle convection, into the Pyre framework. Two CitcomS solvers are coupled to investigate the interaction of a plume at high resolution with global mantle flow at low resolution. A comparison of the coupled models with parameterized models demonstrates the accuracy and efficiency of the coupled models and illustrates the limitations and utility of parameterized models.

3.1 Introduction

Geological processes encompass a broad spectrum of length and time scales, often with different physical processes dominating at either different locations or scales. Traditionally, a modeling code (a solver) is developed for a problem of specific length and time scale, but its utility beyond the original purpose is often limited. Modeling the dynamics of geophysical systems of all relevant scales is challenging with present-day tools. Writing a completely new solver covering such broad temporal and spatial scales is a substantial investment and may be undesirable. Leveraging existing, benchmarked, single-scale solvers and coupling them to solve multi-scale problem would be a more viable alternative. The GeoFramework software addresses this need through creating and maintaining a suite of reusable and combinable tools for solid Earth problems.

GeoFramework extends Pyre, a Python-based modeling framework. Pyre is originally developed to link solid (Lagrangian) and fluid (Eulerian) solvers, as well as mesh generators, visualization packages, and databases, with one another for engineering applications [*Cummings et al.*, 2002]. Within the Pyre framework, a solver is aware of the presence of other solvers, and they can all interact with each other via exchanging information across adjacent mesh boundaries. Such interaction is termed “solver coupling.” There are four advantages of solver coupling for multi-scale problems in geophysics:

(1) Natural boundary conditions (BCs): Often BCs are set *a priori* on only one of the multi-boundaries available (such as sidewalls). Reflecting or periodic BCs can result in unrealistic deformation. However, if a regional solver is coupled with a solver of a larger domain (but of coarser resolution), the deformation

field of the later solver can be used as the BCs of the former solver, while the response of the former solver can be fed back to the later solver. Therefore, the regional solver can have more natural BCs. Alternatively, an uncoupled model with traditional mesh refinement, i.e., the study area in high resolution and a vast surrounding area in low resolution, can achieve similar goals.

(2) Computational efficiency: The stable time step size is proportional to the smallest grid resolution, linear in hyperbolic equations and quadratic in parabolic equations. In an uncoupled model with mesh refinement, each step can advance in time only by a small amount, dictated by the finest grid. Computation on the coarser grid, which does not require such a small time step, must use the same small time step as the finest grid. In the case of a coupled, multi-resolution model, since different solvers can have time steps of different sizes, the coarser-resolution solver can have a larger time step, resulting in a substantial improvement in computational efficiency over traditional mesh refinement.

(3) Multi-physics models: A geophysical process can involve the coupling of a wide suite of physical processes. For example, the mechanism of post-seismic deformation can be either elastic or plastic. A solver that can handle all aspects of the relevant physics may not be available, or if available, the code would be complicated and difficult to maintain and develop. On the other hand, the problem can be handled by multiple solvers coupled together, with each solver responsible for fewer physical processes, so that the code for each solver is simple and manageable.

(4) Data assimilation and prediction: Data output by one solver can be seamlessly passed as the input to another solver. For example, the result of a mantle convection model, when converted to seismic velocity with the aid of a mineral physics database, can be fed into a seismological code to generate synthetic seismograms, which can be compared with observation to further improve the convection model.

In geodynamics, one can imagine several examples where solver coupling would have considerable utility. Solver coupling can simulate the interaction between large-scale and small-scale mantle convection, the viscous mantle and elastic crust, mantle flow and the thermodynamics of mineral phase relations, tectonic stress loading and earthquake rupture, and earthquake rupture and seismic wave propagation. In this paper, we approach the problem of mantle convection interacting at two different length scales. In a companion paper (*Choi et al.*, manuscript in preparation), we will demonstrate the linkage between long-term crustal deformation and mantle convection.

A challenging mantle convection problem is the tilting of a plume conduit in large-scale mantle flow. Hot material rising from a hot thermal boundary layer forms a low viscosity plume conduit. The tilting of a plume conduit has a substantial influence on the location of a hotspot. Global flow models, in which the motions of plumes are parameterized, show that hotspot locations are influenced by large-scale flow [*Steinberger and O'Connell*, 1998]. However, the parameterized model assumes that the presence of plumes does not change the background mantle flow. It also assumes that the motion of a plume conduit can be parameterized by the vector sum of the ambient flow and the rising velocity of the plume conduit, which is inversely proportional to the ambient viscosity and not affected by the presence of the top or bottom boundaries. The validity of these assumptions is unclear and unverified, because of several difficulties. Since the rising velocity of a plume conduit is not easy to measure, the effect of boundaries on the flow is difficult to quantify. On the other hand, numerical calculation of whole mantle flow with sufficient resolution to resolve a plume conduit remains beyond the capability of the most powerful computers, while numerical calculation of regional models is inadequate because of the missing large-scale flow. This motivates us to apply the Pyre framework to this geophysical problem. Here, we use the interaction of a plume at high resolution with global mantle flow (each computed by an instance of the finite element code, *CitcomS*) as a test case demonstrating the utility of the Pyre framework.

In this paper, we describe the science-neutral Pyre framework and then introduce a new software package that has been developed for coupling geophysical solvers. We then present the results from the plume–global flow coupling. In the appendices, we demonstrate the numerical veracity of the methods.

3.2 Overview of Pyre

Pyre is a full-featured, object-oriented environment that is capable of handling all aspects of the specification and launch of numerical investigations. Pyre operates on massively parallel supercomputers including both shared memory computers and Beowulf clusters. Pyre is written in the Python programming language, an open-source, well-maintained and widely used interpretive environment.

Pyre leverages the extensibility of the Python interpreter to allow for the seamless integration of rather diverse computational facilities. The framework provides enough flexibility to allow the dynamic discovery of available facilities as part of simulation staging. There is a well-defined and well-documented method by which a new solver or a new material model can be made available to the framework, while the flexibility allows the user to specify solvers and algorithms in the simulation script, without the need for recompilation or relinking. The combination promotes experimentation with new algorithms by lowering the overall overhead associated with trying out new approaches.

Each simulation model under Pyre is called an *Application.* An *Application* could contain one or more *Solvers*. An *Application* and its *Solver(s)* can run on multiple processors, but each processor has only one *Application* and one *Solver* on it (Figure 3-1). The role of the *Application* is to assign each processor a *Solver* and orchestrate the simulation staging of the *Solver(s)*, such as initialization (including memory allocation and variable assignment), time marching, and output (Appendix C.l).

3.3 CitcomS.py

We restructured *CitcomS*, a finite element code for mantle convection in a 3-D full spherical shell [*Zhong et al.*, 2000], and its regional variant (a cutout bounded by lines of constant latitude and longitude) [*Tan et al.*, 2002; *Conrad and Gurnis,* 2003], ported to Pyre, and renamed the code to *CitcomS.py* (available under the GNU General Public License at http://geodynamics.org). The ported version can execute as a stand-alone program, like the old version, or as a *Solver* under a Pyre *Application* (Appendix C.2). The later case is a

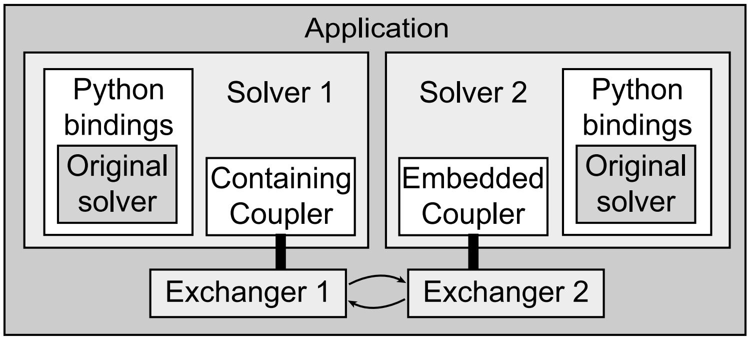

Figure 3-1. The architecture of a coupled *Application*. The *Application* has two *Solvers*. The original code of the solver (in C/C++/Fortran) is complied into a library, which is called by the Pyre *Solver* via the Python bindings. *Solver 1* is the containing solver and has a *ContainingCoupler*, *Solver 2* is the embedded solver and has an *EmbeddedCoupler*. The *Couplers* communicate via the *Exchangers*, which are external to the *Solvers*.

prerequisite of coupled models. The restructuring involves a few top-level functions, leaving the numerical algorithm and internal data structure unchanged.

3.4 Coupler and Exchanger

To restrict the scope of this paper, we assume that two *Solvers* are coupled in a Pyre *Application* (Figure 3-1). The domain of one *Solver* is completely immersed within the domain of the other *Solver* (Figure 3-2A). The former is called the *embedded Solver*, and the later the *containing Solver*. The containing *Solver* has a *ContainingCoupler*, while the embedded *Solver* has an *EmbeddedCoupler*. The interactions between the *Solvers* are simulated by sharing physical quantities (such as velocity, temperature, or traction) on the interfaces, which has the form of sending and receiving information between *Solvers*. The *Couplers* drive the information exchange and synchronize the *Solvers* (Appendix C.3).

The actual information exchange occurs in the *Exchanger* (Figure 3-1), which consists of a number of C++ classes. The *Exchanger* of a *Solver* can communicate with another

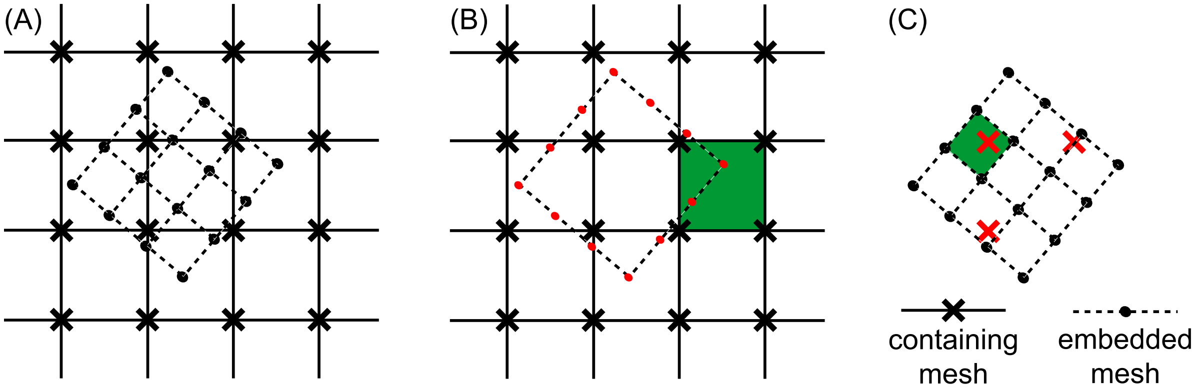

Figure 3-2. An example of a 2-D embedded mesh and a portion of the containing mesh. (A) The embedded grid is in dash line, and the containing grid in solid line. The embedded nodes are shown as dots, and the containing nodes as crosses. The meshes reside on separated *Solvers* but overlap in the modeling space. The embedded mesh is completely immersed within the containing mesh. The two meshes are not required to be parallel to each other. Two scenarios of *BoundedMesh* are presented. (B) The embedded *Solver* is *Solver B*. Its *BoundedMesh* consists of twelve boundary nodes (red). The coordinates of these nodes are sent to *Solver A* (the containing *Solver*) to find the corresponding elements (green, only one element is colored) and shape functions. (C) The containing *Solver* is *Solver B*. Its *BoundedMesh* is the three nodes (red) in the overlapping region. One corresponding element is shown in green.

Exchanger of a different *Solver*. An *Exchanger* is specific to its host *Solver*, but independent from the *Solver* that it is coupled to. The detail and complexity of the coupling mechanism is isolated inside the *Coupler*, leaving the *Exchanger* flexible and extensible. For example, although the *Exchanger* of *CitcomS.py* is developed to couple with another *CitcomS.py*, it can couple with an elastic *Solver* for crustal dynamics problems (*Choi et al.*, manuscript in preparation). Since a goal is to leverage existing modeling code, the *Exchanger* is external to the *Solver* and not required for uncoupled applications.

For simplicity, let us first consider the case of a single-processor *Solver* coupled with another single-processor *Solver*. *Solver A*, which is going to send a message, has an *Outlet*, while *Solver B*, which is going to receive, has an *Inlet*. First, *Solver B* has a *BoundedMesh*. The *BoundedMesh* contains a set of nodes at the interfaces of coupling *Solvers* and maintains a bounding box of those nodes, hence its name. Here we use “interface” in a loose sense. The set can be the whole collection of boundary nodes of an embedded *Solver* (Figure 3-2B), or only part of it, or the nodes in the overlapping region (Figure 3-2C). The *Inlet* sends the *BoundedMesh* to the *Outlet*. The *Outlet* uses the bounding box as an efficient check on whether the *BoundedMesh* overlaps with the domain of *Solver A*. The *Outlet* then assembles the requested data (usually by interpolation of a local field variable to the nodes in the *BoundedMesh*) and sends them to the *Inlet*. With finite-elements, the interpolation involves finding the corresponding element and computes the shape functions of each node in the *BoundedMesh* and is the most time-consuming procedure. If both meshes are static (Eulerian), this procedure is computed only once and the shape functions are stored for subsequent use. If one of the meshes changes with time (i.e., Lagrangian), this procedure repeats at every time step. The *Inlet* then imposes the data received to the interface nodes. Depending on the use of the data, the action of “impose” can have different meanings. If it is used as BCs, the BC arrays are updated; otherwise, it might simply replace the field variable.

In the case of multi-processor coupling, the procedure becomes more complicated (see function *initialize* in Appendix C.3). Each processor still has an *Inlet* (for *Solver B*) or an *Outlet* (for *Solver A*). Additionally, each processor of *Solver A* has a *Source*, but only the leading processor of the *Solver B* has a *Sink*. Each processor of *Solver B* constructs a *BoundedMesh* according to its local mesh. Those local *BoundedMeshes* are broadcast out by the *Sink* to all *Sources*. Each *Source* passes the received *BoundedMesh* coordinates to the *Outlet*, which performs the same interpolation procedure as the single-processor case. The *Outlet* passes the interpolated results to the *Source*. The *Sink* collects the results from all *Sources* in *Solver A* and distributes the collected data to all *Inlets*. *Inlets* then impose these data to the interface nodes. In general, *Solvers* have their own domain decomposition scheme, and the decomposition boundaries of two *Solvers* do not coincide. Therefore, nodes in a local *BoundedMesh* of an *Inlet* might be interpolated by different *Outlets*. The *Sources* and *Sink* maintain the bookkeeping of overlapping nodes.

During different stages of a coupled computation, a *Solver* can act as *Solver A* or *Solver B*, i.e., either to send or receive data. One advantage of coupled computation is for the containing *Solver* sending the BCs to the embedded *Solver*. If data are sent from the containing *Solver* to the embedded *Solver* only, it is called *one-way communication*. If data are sent from the embedded *Solver* to the containing *Solver* as well, it is called *two-way communication*. For one-way communication, there is no feedback from the embedded *Solver* to the containing *Solver*, and the containing *Solver* nearly executes like a stand-alone computation, but providing BCs to the embedded *Solver*. Only for two-way communication is the response of the embedded *Solver* fed back to the containing *Solver*.

Different *Solvers*, depending on their design, usually have different coordinate systems and units to represent the physical quantities internally. To facilitate information exchange, we require that any quantities be exchanged in Cartesian coordinates and SI units. Conversion from and to the native coordinate system and units is carefully handled within the *Inlet* and *Outlet*. An option of skipping conversion is available if the *Solvers* use the same coordinate system and units.

During a coupled computation, the *Coupler* monitors the model times of both *Solvers* (see function *clip_stable_time_step* in Appendix C.3). If the model times of both *Solvers* are equal, they are *synchronized*. For example, in Figure 3-3, step *M+3* and step *N+1* are

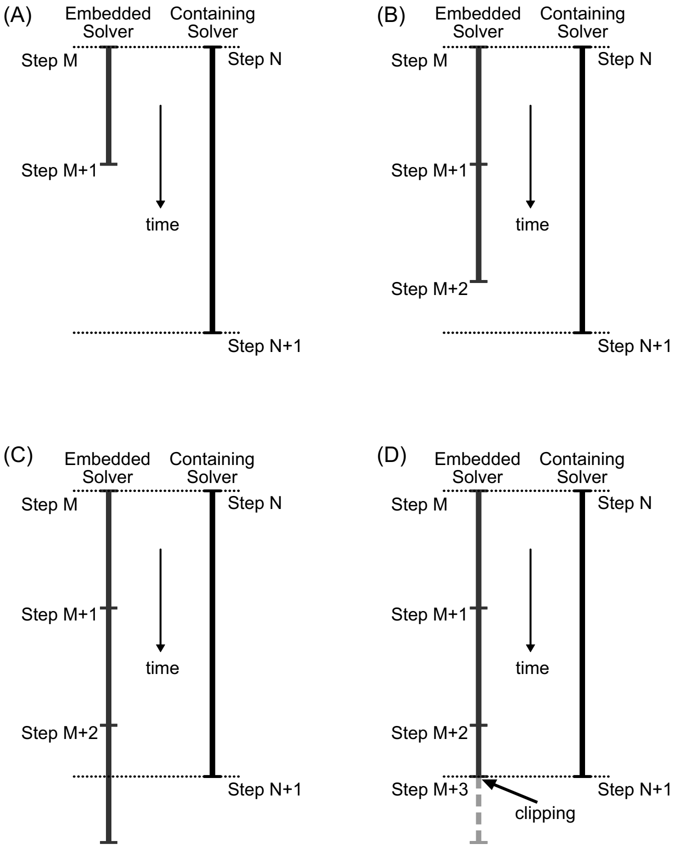

Figure 3-3. Synchronizing time steps of two *Solvers*. (A) After a synchronized step, the containing *Solver* will be ahead of the embedded *Solver*. (B) and (C) The embedded *Solver* keeps marching forward. The containing *Solver* waits until the embedded *Solver* catches up. (D) The embedded *Solver* clips the size of its stable time step so as to synchronize with the containing *Solver*.

synchronized, but step *M+2* and step *N+1* are not. Only when the times are synchronized, is the containing *Solver* allowed to march forward to the next time step. Generally, the containing *Solver* has a coarser mesh than the embedded *Solver* and has a larger stable time step. As a result, at the end of a time step, the containing *Solver* will be ahead of the embedded *Solver* (Figure 3-3A). The containing *Solver* must wait until the embedded *Solver* catches up (Figure 3-3B-C). The embedded *Solver*, if necessary, will clip the size of its stable time step so as to synchronize with the containing *Solver* (Figure 3-3D).

3.5 CitcomS-CitcomS Coupling

Having examined the coupling mechanism in general, we now describe the physical quantities exchanged for a specific application of *CitcomS-CitcomS* coupling. For the embedded solver, velocity or traction BCs are required to solve the continuity and momentum equations (see function *solve_velocity* in Appendix C.2). We found that imposing three components of velocity as BCs on all boundary nodes leads to poor convergence because of mesh locking [*Hughes*, 2000]. With normal velocity and shear traction imposed as BCs, the stiffness matrix is the same as those of uncoupled problems, and we can find convergent solutions. The embedded *Solver* also needs temperature BC to solve the energy equation. We impose temperature on every boundary node. For the two-way communication, we use the temperature field of the embedded *Solver*, which is more accurate, to override the temperature field of the containing *Solver* (see function *new_time_step* in Appendix C.2). The veracity of the coupling method has been extensively tested in a series of benchmarks. The results of the benchmarks are given in Appendix A and B.

3.6 Model Setup

We will show an example of two *CitcomS.py Solvers* coupled in two-way communication (Figure 3-4). The embedded *Solver* is a high-resolution regional *CitcomS.py*. The containing *Solver* is a global *CitcomS.py*. The resolution of the containing mesh is 180 km horizontally and 40–100 km vertically with mesh refinement near the bottom boundary. The embedded mesh has a resolution of 40 km in each direction and is centered near Hawaii. Both meshes have an inner radius 0.55 and an outer radius 1. The ambient viscosity, η_a, is 100 for the lithosphere (with the base at 90 km depth), 1 for the upper mantle, and 30 for the lower mantle. The non-dimensional viscosity is temperature-dependent according to $\eta=0.1\eta_a \exp(1.74/(T+0.5)-1.74/1.5)$, where T is the temperature. The model has a Rayleigh number $3\text{x}10^7$. The temperature BC at the core-mantle boundary (CMB) is $T=0$ except in a small region beneath Hawaii, where a circular region centered at 20°N, 155°W has elevated temperature $T=\exp(-s/s_0)$, where s is the distance to the center, and $s_0=750/6371$. The temperature BC at the surface is $T=0$. The mantle is isothermal ($T=0$) with a no-slip top surface initially. A plume develops from the heated region and rises vertically. After the plume impinges the surface, we impose plate motion from 80 Ma to the present using the plate motion model of *Lithgrow-Bertelloni and Richards* [1998]. The resultant mantle temperature is zero everywhere except the plume. Since two-way communication is used, the temperature fields are consistent across the meshes.

We defined the hotspot position by locating the temperature maxima at 160 km depth, implicitly assuming that partial melting occurs at this depth and the melt rises and escapes to the surface through a vertical conduit. At shallower depth, the temperature anomaly tends to be attached to the lithosphere and translates with the plate, which is not representing the motion of the plume.

The two-way communication model is compared with another two models. One model is similar to the two-way communication model, except using one-way communication. The containing mesh in the one-way communication model is driven purely by the plate motion and has no temperature heterogeneity. The comparison between the two-way and one-way communication models will address the influence of the plume buoyancy on the global mantle flow, which, in turn, affects the motion of the plume conduit. The plume only resides in the embedded mesh. Therefore, the temperature fields are inconsistent with one another.

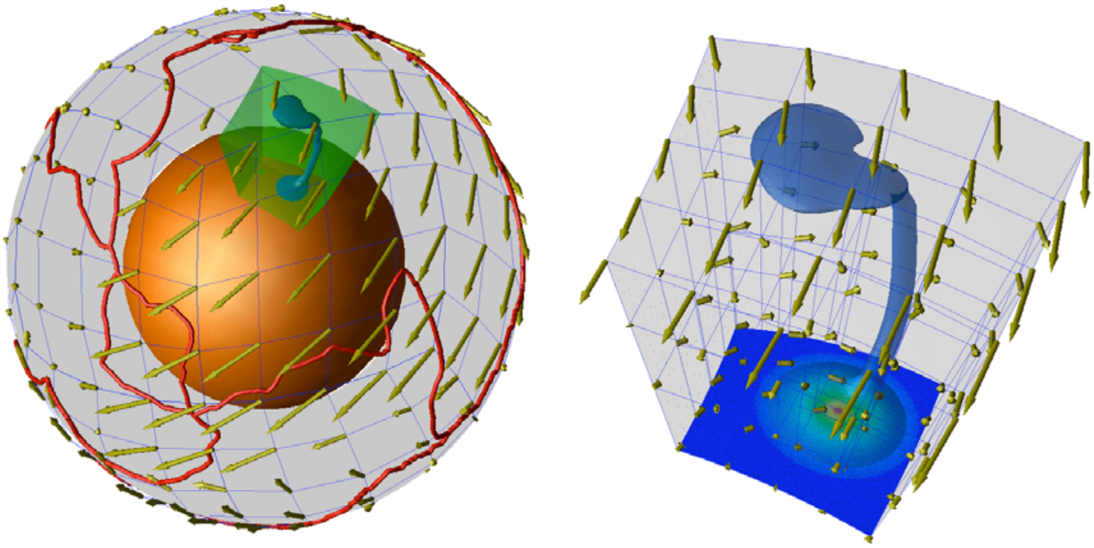

Figure 3-4. *CitcomS-CitcomS* coupling. The containing *Solver* (left) is a global model, with plate motion imposed on the top surface. The view is centered on the western Pacific. Red lines are plate boundaries. Yellow arrows are imposed plate motion. The orange sphere is the core. The small green box is the domain of the embedded *Solver*. The embedded *Solver* (right) is a high-resolution regional model, with boundary conditions retrieved from the containing *Solver*. The black line is the past hotspot location. The red segment is the assumed melt conduit, starting at 160 km depth. The velocity vector is in yellow. The temperature BC at the CMB is shown in color. The plume is visualized as an iso-surface ($T=0.08$). The numbers of grid points of both meshes are reduced for visualization purpose.

Another model is the parameterized model of plume ascent, following the method of *Steinberger and O'Connell* [1998]. The plume conduit starts from a fixed point at 20°N, 155°W and 200 km above the CMB and ends at 180 km below the top surface. The conduit is advected according to the vector sum of the ambient flow and the rising velocity of a plume conduit, $w=w_0/\eta_a$, which is inversely proportional to the ambient viscosity. Since w_0 is difficult to determine from a dynamic model, we use a range of w_0 to find the best fitting model. The ambient flow is taken from an uncoupled global-scale dynamic model. This global flow model is identical to that in the one-way communication model. The comparison between the one-way communication and parameterized models will address the validity of the parameterized plume motion.

3.7 Results

The evolution of the plume conduit in the two-way communication model is shown in Animation 3-1. The initial plume conduit is vertical. When the plate motion is imposed at 80 Ma, the plume is swept laterally by the mantle flow. The hotspot progresses to the northwest during 80–74 Ma, then, it progresses to the north until 65 Ma (thick solid line in Figure 3-5). At this stage, the movement of the hotspot is parallel to the plate motion, and the plume conduit is tilted towards the northwest too. Between 65–43 Ma, the plate motion is generally to the north, while the hotspot progresses to the northeast. The plume conduit, which was tilted to the northwest, becomes tilted to the north. This readjustment causes the apparent eastward hotspot motion. After 42 Ma, the plate motion changes to the northwest, but with reduced northward component. The readjustment of the plume conduit induces a southward movement to the hotspot. As a result, the hotspot motion becomes westward. At the end of simulation, the hotspot has been displaced 1000 km northwest away from its original location.

The results of the one-way communication model (thin solid line in Figure 3-5) are close to the results of two-way communication model. The former model slightly overestimates the hotspot motion by about 110 km in the 80–74 Ma period, when the plume head has not yet

Animation 3-1. The evolution of plume conduit in the two-way communication model. See the caption of Figure 3-4 for detailed description.

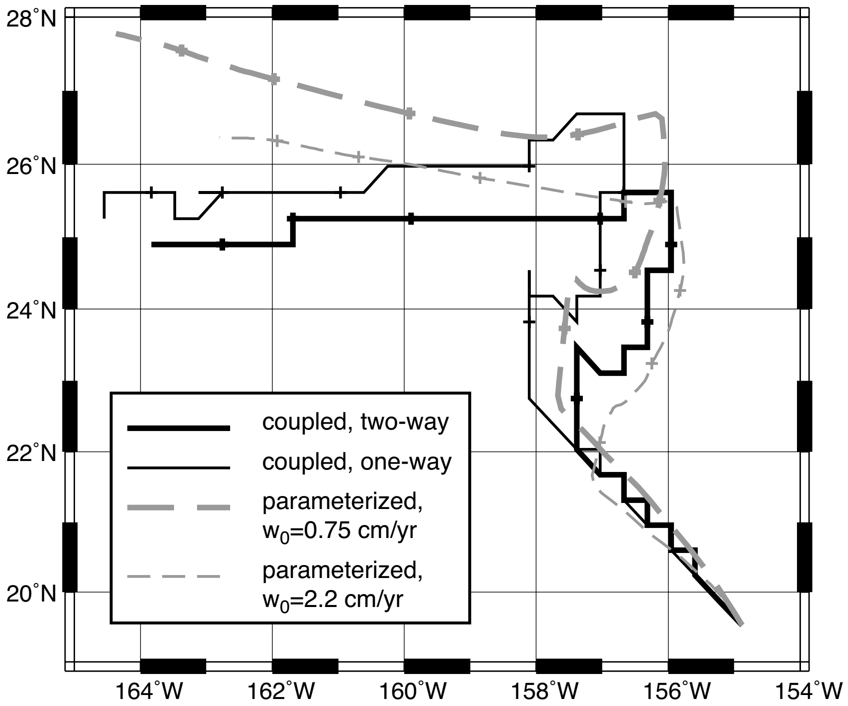

Figure 3-5. The hotspot locations from different models. Each line represents the motion of the hotspot, starting from the lower right corner, over 80 Myrs. A tick (+ symbol) is plotted at intervals of 10 Myrs. The zigzagged hotspot locations of the coupled models are artifacts from locating temperature maxima on a discrete grid.

dissipated. After the period, both models agree well if the prior overestimate is removed. At the final step, the separation between the hotspots is about 110 km, and the azimuths to the original location are similar. This suggests that the global flow is not significantly altered by the presence of the plume conduit. The result is not surprising. When the temperature field is interpolated from the embedded mesh and fed back to the containing mesh, the plume conduit is not well-resolved by the containing mesh. As a consequence, the temperature anomaly of the plume is weak and perturbs the flow only slightly.

Two parameterized models with different w_0 are shown (dashed lines in Figure 3-5). The model with w_0=0.75 cm/yr best fits with the one-way communication model. Both hotspot locations generally agree with each other during 80–40 Ma, with a separation of about 50 km, but diverge after that. At the final step, the separation is about 270 km, and the azimuths are off by about 10°. If we use w_0=2.2 cm/yr, which is used in *Steinberger and O'Connell* [1998] too, the final hotspot will be off by about 210 km and 10°. On the other hand, this model agrees better with the two-way communication model. We consider this agreement fortuitous, because the models are driven by different global flows. The hotspot separation between the parameterized and coupled models is a metric to the accuracy of the parameterized model. The relative error of the parameterized model, defined as the ratio between the separation to the total displacement of hotspots, is about 20%. We find the accuracy of the parameterized models acceptable, considering its small requirement in computational cost.

From the comparisons, we conclude: 1) The plume conduit in our model does not change the plate-driven flow significantly; 2) the parameterized model can approximate the hotspot location with an appropriate w_0. Nevertheless, the choice of w_0 is not self-evident and should best be guided by the coupled model.

The uncoupled global flow model required ≈40 hours of computation on a Beowulf cluster, while the coupled model requires ≈64 hours. With a 60% increase in computation time, we find a solution with a 4-fold increase in resolution in the plume region of the coupled model. To achieve the same resolution, an uncoupled model with mesh refinement would have required a time step size 1/4 the size of the coupled case and would have taken ≈256 hours to compute. With such large savings in computational resources, problems that were too expensive can become manageable with solver coupling.

3.8 Conclusion

As our understanding of Earth's deformation improves, more sophisticated models are needed to explore the deformation process. However, the growing complexity of future models will exceed the capabilities of current generation solvers. Solver coupling can extend the capability of existing solvers with moderate investment. We have developed a software package to couple geophysical solvers and demonstrated the feasibility to solve a multi-scale problem efficiently via solver coupling. In a companion paper, we will demonstrate the feasibility to solve multi-scale, multi-physics problems using the same technique (*Choi et al.*, manuscript in preparation). We believe that this new technique will provide a new venue to address problems that were too expensive or too complicated to solve before. The software is freely available to the community.

References

Conrad, C. P., and M. Gurnis (2003), Seismic tomography, surface uplift, and the breakup of Gondwanaland: Integrating mantle convection backwards in time, *Geochem. Geophys. Geosyst.*, *4*, 1031, doi:10.1029/2001GC000299.

Cummings, J., M. Aivazis, R. Samtaney, R. Radovitzky, S. Mauch, and D. Meiron (2002), A virtual test facility for the simulation of dynamic response in materials, *J. Supercomput.*, *23*, 39–50.

Hughes, T. J. R. (2000), *The Finite element method: linear static and dynamic finite element analysis*, 682 pp., Dover Pub., Mineola, NY.

Lithgow-Bertelloni, C., and M. A. Richards (1998), The dynamics of Cenozoic and Mesozoic plate motions, *Rev. Geophys.*, *36*, 27–78.

Steinberger, B., and R. J. O'Connell (1998), Advection of plumes in mantle flow: implications for hotspot motion, mantle viscosity and plume distribution, *Geophys. J. Int.*, *132*, 412–434.

Tan, E., M. Gurnis, and L. Han (2002), Slabs in the lower mantle and their modulation of plume formation, *Geochem. Geophys. Geosyst.*, *3*, 1067, doi:10.1029/2001GC000238.

Zhong, S., M. T. Zuber, L. Moresi, and M. Gurnis (2000), Role of temperature-dependent viscosity and surface plates in spherical shell models of mantle convection, *J. Geophys. Res.*, *105*, 11063–11082.

Part II. Compressible thermo-chemical convection and the stability of mantle superplumes

Chapter 4

Sharp sides to the African superplume

Published in *Science* (2002) by Sidao Ni, Eh Tan, Michael Gurnis, and Don V. Helmberger, **296**, 1850–1852.

Abstract

Beneath southern Africa is a large structure about 1200 km across and extending obliquely 1500 km upward from the core-mantle boundary with a shear velocity reduction of about 3%. Using a fortuitous set of *SKS* phases that travel along its eastern side, we show that the boundary of the anomaly appears to be sharp, with a width less than 50 km, and is tilted outward from its center. Dynamic models that fit the seismic constraints have a dense chemical layer within an upwardly flowing thermal structure. The tilt suggests that the layer is dynamically unstable on geological time scales.

4.1 Introduction

The largest, low velocity structures in the lower mantle occur beneath southern Africa and the mid-Pacific. These low shear wave velocity structures are correlated with hot spots [*Richards et al.*, 1988], suggesting that the decrease in velocity is associated with an increase in temperature. The positive geoid anomaly and high topography over Africa [*Hager et al.*, 1985; *Lithgow-Bertelloni and Silver*, 1998], and the broad scale Cenozoic uplift [*Gurnis et al.*, 2000], are all consistent with warm, rising mantle beneath Africa. However, recent tomographic imaging of the whole mantle suggests that bulk sound velocity and shear velocity (V_s) are negatively correlated within the African and Pacific anomalies [*Masters et al.*, 2000], suggesting that the anomalies are chemical in origin, not thermal. The chemical hypothesis is supported by an inversion of normal modes [*Ishii and Tromp*, 1999], which indicates that the density of the lower mantle may increase within the two low V_s anomalies. If over large scales (scale lengths of 1000 km), high density, chemical anomalies are embedded within thermal upwellings, as found in dynamic models [*Gurnis*, 1986; *Hansen and Yuen*, 1988; *Tackley*, 1998], then we predict that there should be sharp jumps in seismic velocity, either radially or laterally, within the broad scale low V_s structures delineated by seismic tomography. Here, we test this prediction with body wave seismology.

4.2 Seismological Models

We search for rapid variations in V_s along paths between Africa and South America because of an ideal combination of earthquakes and seismic arrays that sample the African anomaly [*Ni et al.*, 2002]. Lowermost mantle structure can be distinguished from event

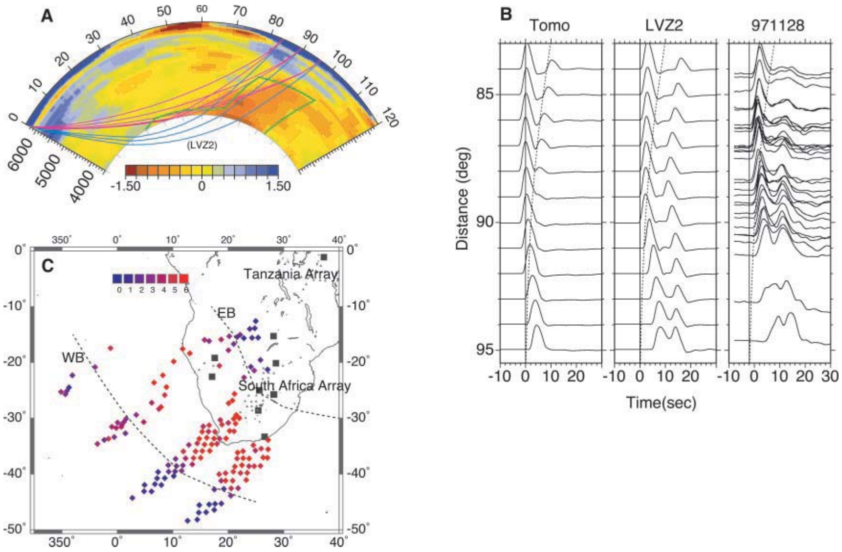

Figure 4-1. Seismological data. (A) Shear velocity from tomography [*Ritsema et al.*, 1999] (in %) from South America to South Africa. The lowest velocities are in red. Green line is idealized LVZ2 structure with sharp sides (3% velocity reduction in enclosed area). Principal ray paths *S*, S_cS (red), and *SKS* (green) sampling these structures for epicentral distances 83° to 95°. (B) Synthetics and observations for *S* and S_cS phases (horizontally polarized component, SH): Tomo for tomographic model, LVZ2 for hybrid model, and 971128 for data recorded at South African Array [*Ni et al.*, 2002]. Large delay of S_cS relative to *S* caused by ALVS structure, which disappears at the larger distances since they both sample the ALVS. (C) The *SKS* geometry showing where rays arriving at stations (Figure 4-S1) exit the core (diamonds) and sample the ALVS structure. The color of the diamonds represents the delay (in seconds) of *SKS* arrival relative to PREM. The two dashed lines indicate the western boundary (WB) and eastern boundary (EB) where the ALVS intersects with the CMB.

mislocation and upper mantle structure using differential travel times of the phases S_cS and *SKS* relative to *S* (Figure 4-1A).

Anomalous patterns in S_cS-*S*, with delays as high as 10 seconds (s) at epicentral distances beyond 90° [*Ni and Helmberger*, 2001; 2003], are not explained by tomographic models that require sharpening and enhancing to produce such strong effects (Figure 4-1B). Moreover, the travel times for the phase *SKS* can change rapidly when crossing the western and eastern boundaries of the African anomaly, with changes as large as several seconds between neighboring stations with spacings of less than 50 km (Figure 4-1C). When *SKS* data are modeled alone there is a trade-off between thickness and velocity reduction that can be removed by adding the combination of S_cS-S and *SKS*-*S* data [*Ni et al.*, 2002]. Our preferred model fitting differential times and waveforms along this corridor is the LVZ2 model (Figure 4-1A). It is a 2-D idealization of a large complex anomaly, which we will refer to as the African Low Velocity Structure (ALVS). The ALVS is aligned NW-SE and is about 1200 km wide, while the cross section LVZ2 extends at least 1000 km above D" and leans toward the east between latitudes 15° to 30°S.

These large-scale features are apparent in seismic record sections. The sharpness of the western boundary (WB) is particularly evident from a rapid jump in travel times occurring near 100˚ for events recorded by the South African Array (Figure 4-2A). Since the travel time jump occurs at different stations for other events this feature is not related to shallow structure [*Ni et al.*, 2002]. A complementary travel time anomaly occurs for phases crossing the eastern boundary (EB), except that the jump in timing occurs in reverse order (Figure 4-2B). *SKS* is delayed about 5 s for epicentral distances smaller than 97º, and becomes normal beyond 99º as recorded by the Tanzanian Array and is unlikely to be related to shallow structure [*Ni et al.*, 2002].

The steepness of the *SKS* paths and their relative sharpness in delay times when crossing the edges of the ALVS are used to map out the boundaries. Although the arrival of *SKS* for large distances (>99º) is normal, it is late for small epicentral distances (<98º), and between 97º and 100º the waveforms are broader (Figure 4-2B). This pattern of waveform complication is probably caused by multipathing. For the shear velocity profile (Figure 4-1A), the raypath of *SKS* around 97º is in the middle of the ALVS and yields a late *SKS* phase.

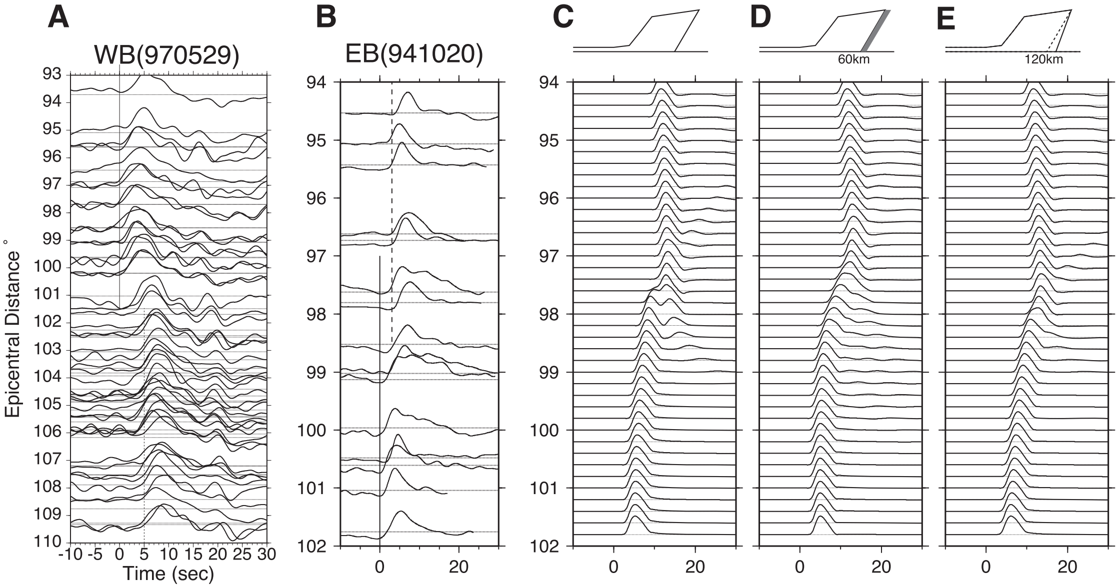

Figure 4-2. Record sections. (A) Record section sampling the WB edge for event 970903 with South African Array. The solid lines indicate the arrival times predicted by PREM, while the dotted lines are aligned with the delayed observations sampling the ALVZ. (B) Record section sampling the EB with the Tanzanian Array. The travel time jumps are about 5 s and occur abruptly where the waveform data show evidence for multipathing (more than one arrival). (C–E) This possibility is explored synthetically by allowing a smooth transition from slow-to-normal at the EB edge. A sample of EB waveform data (B) showing the apparent multipathing is compared with synthetics on the right for various test cases. When the transition is thicker than about 60 km, the *SKS* synthetics change gradually with a few fat pulses near 98°. To produce some of the most disturbed observed waveforms requires a relatively sharp transition and a fortuitous geometry.

However, for large epicentral distances (>100º), the raypath of *SKS* is outside ALVS and leads to normal arrivals. But, when the raypath of *SKS* is close to the boundary of ALVS, two arrivals are produced, one from the ALVS and one from the surrounding higher velocity. If the boundary is sharp enough and the edge is nearly parallel to the raypath of *SKS*, a complicated waveform results.

We demonstrate this phenomena with 2-D synthetic seismograms generated from the LVZ2 model (Figure 4-2C, D, E). For a sharp boundary with the edge almost parallel to a *SKS* raypath, complicated waveforms appear around 97º (Figure 4-2C). But if the boundary is gradual (60 km or more) *SKS* waveforms lose their complexity (Figure 4-2D). By comparing these synthetics with observed record sections, we estimate that the transition width should be less than 50 km. However, the slope of the edges is also important in controlling the shape of the waveforms. We explored the trade-off between width and slope and found that *SKS* waveform distortion does not occur when the edge is not well aligned with the *SKS* raypath (Figure 4-2E). While the idealized synthetics display the waveform complexity over a short epicentral interval, about 1º, the observations indicate a broad zone. Part of this is caused by geometry, where stations at the same epicentral distance are actually separated substantially in azimuth and apparently sample the wall differently.

The multipathing of *SKS* phases, which travel up the sides of the African superplume, are diagnostic of the underlying dynamics. The observations suggest five features of the LVZ2 that are relevant to understanding the origin of the structure: (i) The eastern side of the anomaly is *sharp*, having a drop in shear velocity of about 3% over a lateral length scale less than 50 km, (ii) the eastern vertical boundary of the anomaly is *inclined* or tilted away from the bulk of the anomaly, (iii) the western boundary may also be relatively sharp and tilted in the *same* direction as the eastern boundary, (iv) the location of the sharp interface is *collocated* with the larger-scale seismic anomaly, and (v) the distance between the two sides of the anomaly is between *one and two* times the height of the structure.

4.3 Geodynamic Models

We have attempted to simultaneously fit the observed sharpness and shape of the LVZ2 with models of mantle convection incorporating a plausible range of parameters. The models have a dense basal layer interacting with thermal convection. Two parameters controlling the dynamic models are defined as the following. The Rayleigh number is $Ra=\rho_0\alpha_0\Delta TgR^3/\kappa\eta$, where ρ_0, α_0, ΔT, g, R, κ, and η are the reference density, reference coefficient of thermal expansion, temperature jump across the whole layer, gravitational acceleration, radius of Earth, thermal diffusivity, and viscosity, respectively. The buoyancy number is $B = \Delta\rho_{ch}/\rho_0\alpha\Delta T$, where $\Delta\rho_{ch}$ is the density anomaly associated with the basal layer. The influence of increasing B is to stabilize the dense layer while reducing the topography of the layer [*Davies and Gurnis*, 1986; *Tackley*, 1998].

We use the marker chain method [*Gurnis and Davies*, 1986; *van Keken et al.*, 1997] to represent the boundary between ambient mantle and a homogeneous dense layer, which pre-exists at the base of the mantle. The coefficient of thermal expansion, α, has a fivefold decrease with depth, consistent with mineral physics data [*Chopelas*, 1996]. In some cases, a constant α is used. The temperature-dependent viscosity changes by four orders of magnitude across the bottom thermal boundary layer. These material properties are chosen to enhance the stability of the basal layer. The modeling geometry is a two-dimensional quarter-cylinder, with inner and outer radii equal to 0.5462 and 1, respectively. This domain is evenly divided into 300x70 elements in the azimuthal and radial directions. The surface temperature is fixed at 0, and the bottom temperature is fixed at 1. For models with imposed surface velocity, the surface boundary conditions are temperature fixed at 0.5 and velocity fixed at 1.5 cm/yr (when scaled to Earth). Additional details on our methods can be found in *Sidorin and Gurnis* [1998].

The models are initial value problems in which a dome-like dense structure is situated in the middle of the domain so as to center any subsequent instability. The topography, h, of the layer is initially given by

$$h(\phi) = \begin{cases} h_0 + b * \cos(\pi\phi/\lambda) & \text{, if } |\phi| \le \lambda \\ h_0 & \text{, if } |\phi| > \lambda \end{cases} \tag{4-1}$$

where h_0=0.02, b=0.12, λ=0.8636, and ϕ is the azimuth away from the central plane of symmetry. The initial temperature is given by: $T(r,\phi)=1-0.5*\mathrm{erf}((r-0.5462)/h(\phi))$, where r is the radius.

The chemical origin of the dense layer may be due to substitution of Mg by Fe in the mineral assemblage. Using relations between V_s and temperature and density, we transform model output into V_s. We use the method of *Sidorin and Gurnis* [1998] for temperature- and pressure-dependence of V_s, and $(\partial \ln Vs/\partial \ln\rho)_{P,T}=-1$ [*Karato and Karki*, 2001] for the composition dependence.

With no variations in chemistry and at relatively high *Ra* (10^7), seismic velocity variations occur over a length scale of 200 km with a reduction in V_s of only 2% (Figure 4-3A; profile 1 in Figure 4-3H). By assigning different seismic velocities across the chemical interface, we find a V_s decrease of almost 3% in a distance of 100 km, with half of the decrease occurring as an abrupt jump (Figure 4-3B, C; profiles 2 and 3 in Figure 4-3H). For low Rayleigh number cases (10^6), similar structures are found, but the chemical layer is embedded in a broad thermal halo (Figure 4-3D; profile 4 in Figure 4-3H). We have not been able to find a purely thermal plume that produces an interface sharp enough to give the *SKS* multipathing. We conclude that it is more likely that the interface has a chemical origin.

The inclination of the interface is also diagnostic of the dynamics. If the dense basal layer is stable, then the interface between the two layers is always tilted toward the center of the

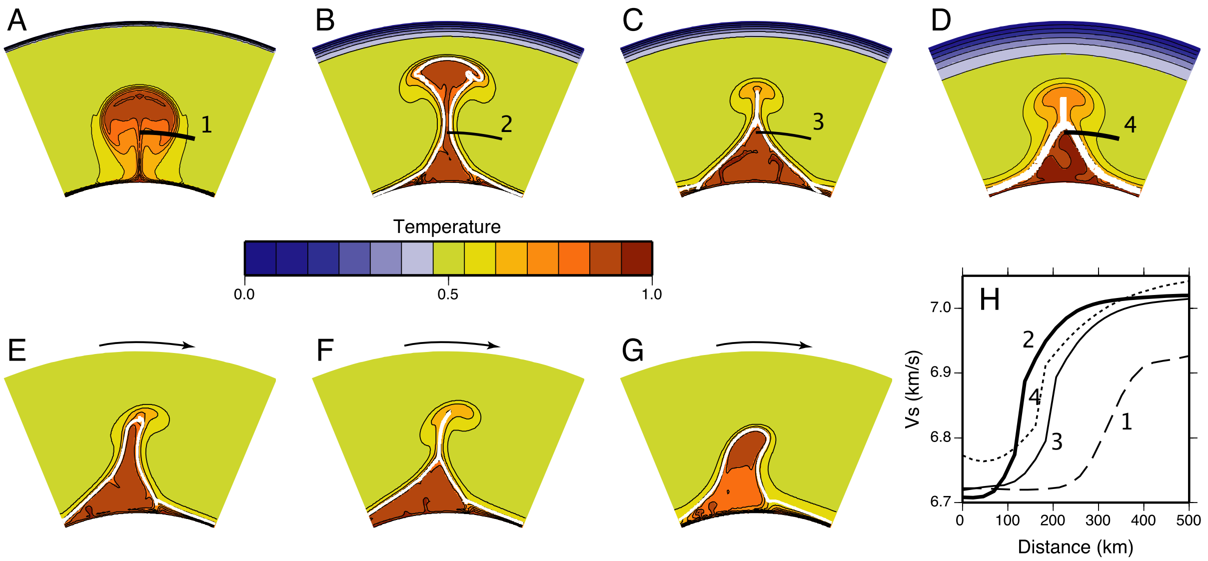

Figure 4-3. Models of thermo-chemical convection. Only central part of model domain is shown. (A–D) Models with no plate velocity. (A) $Ra = 10^7$, $B = 0$. (B) $Ra=10^7$, $B=0.21$; (C) $Ra=10^7$, $B=0.23$. (D) $Ra = 10^6$, $B = 0.23$. The white lines mark the interface of chemical layer, which becomes stable for $B > 0.22$. (D–F) Models with an imposed plate velocity of ~1.5 cm/yr (scaled to Earth). (E) $Ra=10^7$, $B=0.21$, the plume is sheared, but the right boundary is only slightly tilted outward; (F) $Ra=10^7$, $B=0.23$, a more stable chemical layer tilts less to the right. (G) $Ra=10^7$, $B=0.32$ with constant α. (H) Modeled V_s at 2000 km depth. Profile 1 (model in A) has insufficient V_s reduction. Profiles 2 (in B) and 3 (in C) reproduce the sharp V_s reduction as observed. Profile 4 (in D) has sufficient V_s reduction, but fails to reproduce *SKS* sharpness. Only very buoyant layer is capable of reproducing sharpness, tilt, and length scale of LVZ2.

anomaly (Figure 4-3C). We find that the interface becomes tilted away from the central anomaly only when the chemical layer is unstable; that is, when the thermal buoyancy is greater than the chemical. Moreover, the two sides of the rising diapir are generally not parallel (as the seismic observations of Africa suggest) as *both* sides become tilted inward near the base of the mantle and outward near the top of the diapir (Figure 4-3B).

Alternatively, the inclination could be caused by a large-scale mode of convection, including flow associated with plate motion. Over the past 100 My, Africa has moved northeastward in a hotspot frame of reference [*Muller et al.*, 1993]. This motion is in the same overall direction as the tilting of the ALVS [*Ritsema et al.*, 1999]. Although previous models have been able to reproduce the tilt of the ALVS, a tilt that may be caused by the shear associated with the African plate [*Conrad and Gurnis*, 2003], they have diffuse mantle structures inconsistent with the sharpness implied by *SKS* multipathing. This result motivates a second class of dynamic models with an imposed velocity boundary condition simulating the northeastward motion of Africa. The thermo-chemical anomaly with sharp edges can be tilted, but we have been unable to find plumes with subparallel sides (Figure 4-3F) or with widths comparable to their heights (Figure 4-3E). When the coefficient of thermal expansion, α, decreases with depth, we are unable to match the shape of LVZ2. When α decreases with depth, thermo-chemical plumes are unstable in the mid-mantle but stable in the lowermost mantle and give rise to tilts distinctly different from those observed. However, with a uniform α, we are able to reproduce the shape of the LVZ2 (Figure 4-3G). The structure has sharp boundaries tilted over in the direction of plate motion, subparalled sides, and a width comparable to its height. The better fit of cases with apparently unrealistic α suggests that a physical process is absent from the dynamic models. However, models with sharp boundaries and outwardly tilting edges are always transient because the dense chemical layer is being actively entrained upward. The implications of this result are significant for the thermal and chemical evolution of the mantle.

References

Chopelas, A. (1996), Thermal expansivity of lower mantle phases MgO and MgSiO3 perovskite at high pressure derived from vibrational spectroscopy, *Phys. Earth Planet. Inter.*, *98*, 3–15.

Conrad, C. P., and M. Gurnis (2003), Seismic tomography, surface uplift, and the breakup of Gondwanaland: Integrating mantle convection backwards in time, *Geochem. Geophys. Geosyst.*, *4*, 1031, doi:10.1029/2001GC000299.

Davies, G. F., and M. Gurnis (1986), Interaction of Mantle Dregs with Convection - Lateral Heterogeneity at the Core Mantle Boundary, *Geophys. Res. Lett.*, *13*, 1517–1520.

Gurnis, M. (1986), The effects of chemical density differences on convective mixing in the Earth's mantle, *J. Geophys. Res*, *91,* 1407–1419.

Gurnis, M., and G. F. Davies (1986), Mixing In Numerical-Models Of Mantle Convection Incorporating Plate Kinematics, *J. Geophys. Res*, *91*, 6375–6395.

Gurnis, M., J. X. Mitrovica, J. Ritsema, and H. van Heijst (2000), Constraining mantle density structure using geological evidence of surface uplift rates: The case of the African Superplume, *Geochem. Geophys. Geosyst.*, *1*, doi:10.1029/1999GC000035.

Hager, B. H., et al. (1985), Lower mantle heterogeneity, dynamic topography and the geoid, *Nature*, *313*, 541–546.

Hansen, U., and D. A. Yuen (1988), Numerical simulations of thermal-chemical instabilities at the Core Mantle Boundary, *Nature*, *334*, 237–240.

Ishii, M., and J. Tromp (1999), Normal-mode and free-air gravity constraints on lateral variations in velocity and density of Earth's mantle, *Science*, *285*, 1231–1236.

Karato, S., and B. B. Karki (2001), Origin of lateral variation of seismic wave velocities and density in the deep mantle, *J. Geophys. Res.*, *106*, 21771–21783.

Lithgow-Bertelloni, C., and P. G. Silver (1998), Dynamic topography, plate driving forces and the African superswell, *Nature*, *395*, 269–272.

Masters, G., et al. (2000), The relative behavior of shear velocity, bulk sound speed, and compressional velocity in the mantle: implications for chemical and thermal structure, in *Earth's Deep Interior,* edited by S. Karato, et al., pp. 63–87, AGU, Washington DC.

Muller, R. D., et al. (1993), Revised Plate Motions Relative to the Hotspots from Combined Atlantic and Indian-Ocean Hotspot Tracks, *Geology*, *21*, 275–278.

Ni, S. D., and D. V. Helmberger (2001), Horizontal transition from fast to slow structures at the core-mantle boundary; South Atlantic, *Earth Planet. Sci. Lett.*, *187*, 301–310.

Ni, S., E. Tan, M. Gurnis, and D. Helmberger (2002), Sharp sides to the African superplume, *Science*, *296*, 1850–1852.

Ni, S. D., and D. V. Helmberger (2003), Ridge-like lower mantle structure beneath South Africa, *J. Geophys. Res.*, *108*, 2094, doi:10.1029/2001JB001545.

Richards, M. A., et al. (1988), Dynamically supported geoid highs over hotspots - Observation and theory, *J. Geophys. Res*, *93*, 7690–7708.

Ritsema, J., et al. (1998), Evidence for strong shear velocity reductions and velocity gradients in the lower mantle beneath Africa, *Geophys. Res. Lett.*, *25*, 4245–4248.

Ritsema, J., et al. (1999), Complex shear wave velocity structure imaged beneath Africa and Iceland, *Science*, *286*, 1925–1928.

Sidorin, I., and M. Gurnis (1998), Geodynamically consistent seismic velocity predictions at the base of the mantle, in *The Core-Mantle Boundary Region*, edited by M. Gurnis, et al., pp. 209–230, AGU, Washington DC.

Tackley, P. J. (1998), Three-dimensional simulations of mantle convection with a thermo-chemical basal boundary layer: D"?, in *The Core-Mantle Boundary Region*, edited by M. Gurnis, et al., pp. 231–253, AGU, Washington DC.

van Keken, P. E., et al. (1997), A comparison of methods for the modeling of thermochemical convection, *J. Geophys. Res.*, *102*, 22477–22495.

Chapter 5

Metastable superplumes and mantle compressibility

Published in *Geophysical Research Letters* (2005), by Eh Tan and Michael Gurnis, **32**, L20307, doi:10.1029/2005GL024190.

Abstract

Seismically, the African superplume is known to have a sharp lateral transition in V_S and an interface between seismic anomalies with high relief. Such a structure is usually unstable in conventional thermo-chemical convection models. Using a compressible thermo-chemical convection model in which each material has a distinct equation of state, we find an expanded regime of metastable superplumes. In the preferred model, superplume material has a bulk modulus 6% higher and density 2.25% higher than ambient mantle. The inferred physical properties of the superplume are consistent with subducted oceanic crust, simultaneously satisfying seismological, geodynamical, mineralogical, and geochemical constraints.

5.1 Introduction

The African and Pacific superplumes are the most prominent features in the lower mantle. Both superplumes have low shear velocity (V_S), large shear-to-compressional velocity (V_P) heterogeneity ratio ($\delta V_S/\delta V_P > 2.5$) [*Su and Dziewonski*, 1997], anti-correlated bulk sound velocity (V_Φ) and V_S [*Masters et al.*, 2000], and sharp lateral V_S transition [*Wen*, 2001; *Wen et al.*, 2001; *Ni et al.*, 2002; *To et al.*, 2005]. Together, these observations indicate that superplumes are compositionally distinct [*Karato and Karki*, 2001; *Wen et al.*, 2001; *Ni et al.*, 2002]. The superplumes are expected to be warmer than background mantle, as inferred from their low shear velocity, correlation with hotspots and the restored position of Large Igneous Provinces [*Burke and Torsvik*, 2004], and anti-correlation with regions of long term subduction (cool mantle). The confinement of chemical anomalies at the base of upwellings is consistent with the dynamics of thermo-chemical convection [*Gurnis*, 1986; *Jellinek and Manga*, 2002].

From seismological observations, the African superplume has a sharp lateral boundary extending steeply above the CMB for 1000 km and has an ~1000 km width in the mid-mantle [*Ni and Helmberger*, 2003; *Wang and Wen*, 2004; *To et al.*, 2005]. Geodynamic models suggest that high Rayleigh number, thermo-chemical convection is required in order to reproduce such sharp lateral boundaries. Moreover, high relief (steep sides) and a broad width have only been found for unstable structures. Our former conclusion that the African superplume is a hot, chemical anomaly that is unstable and short-lived [*Ni et al.*, 2002] is, however, unsatisfying. The conclusion implies that two mantle layers are being stirred together, which raises questions on the origin and uniqueness of the layers: If the density difference between layers is only marginally stable, how could the dense layer form? Are we observing a turnover event, potentially geologically unique, in which an old dense layer is overturning? Given these problems, a new formulation of compressible convection is advanced that provides an alternative dynamic route to metastability consistent with observed structure.

5.2 Analytical prediction

The stability of a dense layer below ambient mantle has been investigated [*Hansen and Yuen*, 1988; *Davaille*, 1999; *Tackley*, 1999; *Jellinek and Manga*, 2002; *Ni et al.*, 2002; *McNamara and Zhong*, 2004], mostly under the assumption that the density difference between the materials, $\Delta\rho_{ch}$, is depth-independent. Considering a chemical structure with an isothermal interior, because of the depth-dependence of thermal expansion, the lower portion of the structure would be denser than the surrounding mantle while the upper less dense. The upper portion will rise and become a plume, while the lower portion will sink and become a flat layer with cusps. It is difficult to produce stable thermo-chemical structures with high topography and steep sides when thermal expansion decreases with depth. Past models of stable superplumes all assumed constant thermal expansion [*Davaille*, 1999; *McNamara and Zhong*, 2004]. On the other hand, if $\Delta\rho_{ch}$ is not constant, but decreases with depth, the upper portion of the chemical structure can become denser and stable, while the lower less dense and unstable. Under this scenario, a heated dense material can form a metastable superplume with high topography.

Seismological observations provide hints that $\Delta\rho_{ch}$ may decrease with depth. Inside the African superplume, the average V_S reduction is -3%, but the average V_P reduction is -0.5%

Table 5-1. Estimates on the elastic moduli. From the δV_S and δV_P observations, $\delta\mu$ and δK_S of the superplume material can be estimated by assuming $\delta\rho$ (based on V_S and V_P of PREM model at 2500 km depth). The bulk modulus observed in seismology underestimates the bulk modulus at normal geotherm, because of the elevated temperature inside the superplume.

$\delta\rho$	1%	0%	-1%	-2%
$\delta\mu$	-5%	-6%	-7%	-8%
δK_S	3%	2%	1%	0%

[*Ni and Helmberger*, 2003; *Wang and Wen*, 2004]. A V_S reduction of similar amplitude is found inside the Pacific superplume [*To et al.*, 2005], but the V_P reduction and vertical extent of the Pacific superplume remain poorly constrained. The density structure of the African superplume is not well constrained by seismology [*Ishii and Tromp*, 1999; *Romanowicz*, 2001], but is unlikely to be 1% denser than the ambient mantle due to the observed high topography. A simple calculation of the shear and bulk moduli (μ and K_S) anomalies (Table 5-1) shows that unless the African superplume has very low density (<-2%), which has previously been explored [*Ni et al.*, 2002] and will not be considered further in this paper, its K_S must be larger than the values in PREM [*Dziewonski and Anderson*, 1981].

Materials with different K_S have different adiabatic density profiles. The adiabatic density profile of ambient mantle (material 1), $\rho_{1,ad}$, can be calculated by integrating the equations for self-compression

$$\begin{aligned} dP_H &= -\rho_{1,ad} g dz \\ d\rho_{1,ad} &= \frac{Di}{\gamma}\frac{\rho_{1,ad}}{K_{S1}} dP_H \end{aligned} \tag{5-1}$$

where P_H is the hydrostatic pressure; g is the gravity; Di is the dissipation number; γ is the Grüneisen parameter; K_{S1} is the adiabatic bulk modulus of the ambient material. A compositionally distinct material (material 2) with a bulk modulus K_{S2} will have an adiabatic

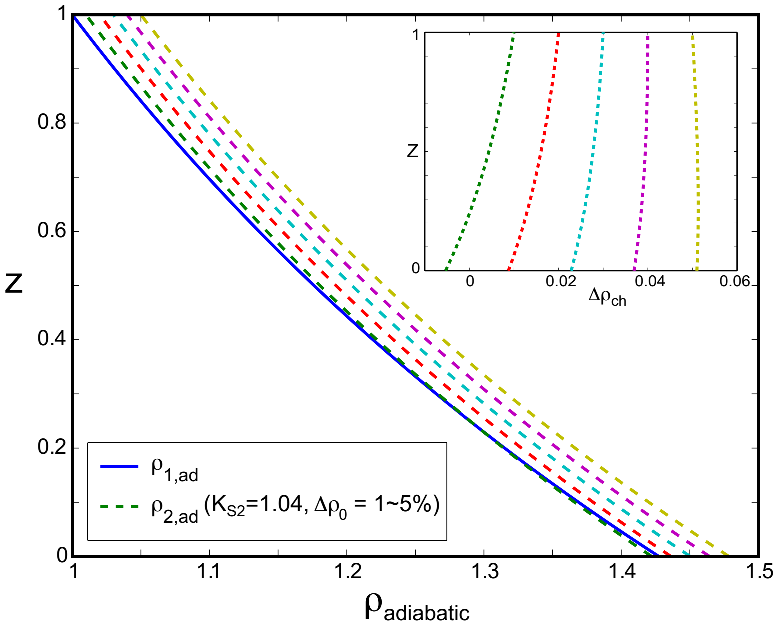

Figure 5-1. Adiabatic density profiles. The solid line is the adiabatic density profile of ambient mantle (K_{S1}=1, ρ_0=1). The dashed lines are adiabatic density profiles of superplume material for K_{S2}=1.04, but variable $\Delta\rho_0$ (1%-5%). The inset shows the chemical density anomaly (compared to ambient mantle) of the superplume material.

density, $\rho_{2,ad}$, given by

$$d\rho_{2,ad} = \frac{Di}{\gamma}\frac{\rho_{2,ad}}{K_{S2}}dP_H \tag{5-2}$$

The compositional density anomaly, $\Delta\rho_{ch}$, is the difference between $\rho_{2,ad}$ and $\rho_{1,ad}$, and can decrease with depth if K_{S2} is significantly higher than K_{S1} (Figure 5-1).

The thermal density anomaly is $\Delta\rho_{th}$=-$\rho\alpha dT$, where dT is the excess temperature and α is the coefficient of thermal expansion and is depth-dependent. We define a "height of neutral buoyancy" (HNB) as the height above the core-mantle boundary where the density is neutral, i.e., $\Delta\rho_{total}$=$\Delta\rho_{ch}$+$\Delta\rho_{th}$=0. By assuming a constant dT with depth (Figure 5-2), we can calculate HNB and predict the stability of the dense layer for range of zero-pressure densities and bulk moduli.

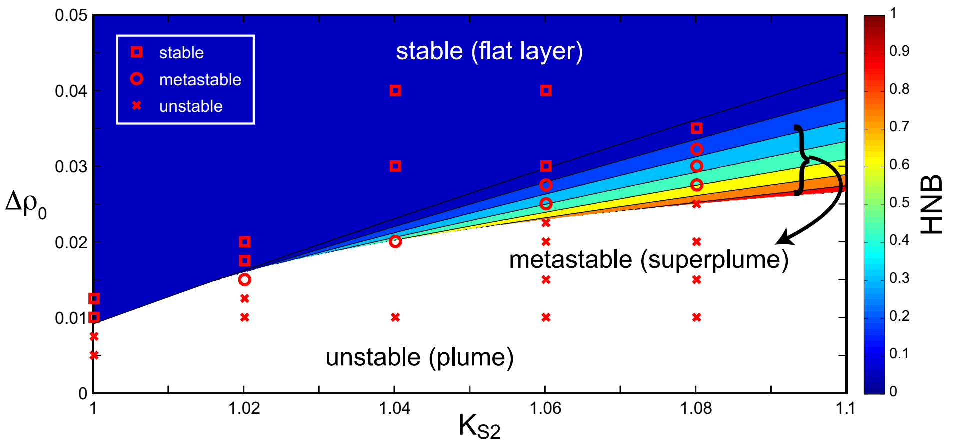

Figure 5-2. Predicted (color contours) and calculated (symbols) domains for stability of thermo-chemical convection with two materials of differing equations of state. Assuming the excess temperature of the anomalous material dT=0.7, the predicted height of neutral buoyancy (HNB) is contoured. For K_{S2}<1.02, all of the contours converge, such that the transition between stability and instability is abrupt. For K_{S2}>1.02, a domain of metastability becomes possible and expands with higher K_{S2}. Outcomes of finite amplitude calculations in which the convective mode and stability are inferred from morphology and density structure are plotted as symbols.

5.3 Numerical method

We modified the finite-element code ConMan [*King et al.*, 1990], using the Truncated Anelastic Liquid approximation [*Ita and King*, 1994] for the governing equations. The continuity and momentum equations are solved using a mixed method formulation [*Hughes*, 2000]. We adapted the pressure correction algorithm [*Ramage and Wathen*, 1994] and used the Bi-Conjugate Gradient Stabilized method [*Barrett et al.*, 1994] to iteratively solve the equations. The algorithm and benchmark are described separately [*Tan and Gurnis, in prep.*]. The interface of distinct materials is traced by a marker chain [*Sidorin and Gurnis*, 1998]. The non-dimensional parameters used in the models are Rayleigh number ($Ra=\rho g\alpha\Delta Th^3/\kappa\eta$=2.2x$10^5$ to 2.2x10^6), dissipation number ($Di=\alpha gh/C_P$=0.4), Grüneisen parameter ($\gamma=\alpha K_S/\rho C_P$=1.333), normalized surface temperature ($T_0/\Delta T$=0.75), fraction of density change due to thermal expansion ($\varepsilon_T = \alpha \Delta T$=0.054), initial thickness of dense layer (d_0=0.08 to 0.125), and rate of internal heating of the anomalous material (H=0 to 100). The coefficient of thermal expansion is $(1+3.2(1\text{-}z)^{8.5})^{-1}$ for most cases, which is obtained from thermodynamic calculation [*Sidorin and Gurnis*, 1998], or is linear in z in some cases. The viscosity is temperature-dependent (changing by a factor of 100) and mildly depth-dependent (to compensate for the adiabatic temperature gradient). The side walls have reflecting boundary conditions. The horizontal boundaries have free-slip and isothermal boundary conditions. The initial temperature is an adiabatic temperature gradient with small perturbations.

5.4 Results

We computed a series of 2D thermo-chemical convection models, in which the zero-pressure density anomaly, $\Delta\rho_0$, and bulk modulus, K_{S2}, of the chemically distinct material is systematically varied between $\Delta\rho_0$ of 0.0 and 0.04 and K_{S2} between 1.0 and 1.08. We find a wide range of thermo-chemical structures that we classify in terms of the morphology and evolution (Figure 5-2).

First, when $\Delta\rho_0$ is sufficiently large for all K_{S2} investigated, the anomalous material forms a layer with small relief in which sharp cusps occur at the highest elevations of the layer interface (square symbols in Figure 5-2; Figure 5-3A-C). The HNB is either too low (lower than the initial layer thickness) or non-existent ($\Delta\rho_{total}$ is always positive). In no cases has the layer been regionally swept off the bottom. This structure is stable with the most significant exchange occurring at the aforementioned cusps. This is a dynamic mode previously well

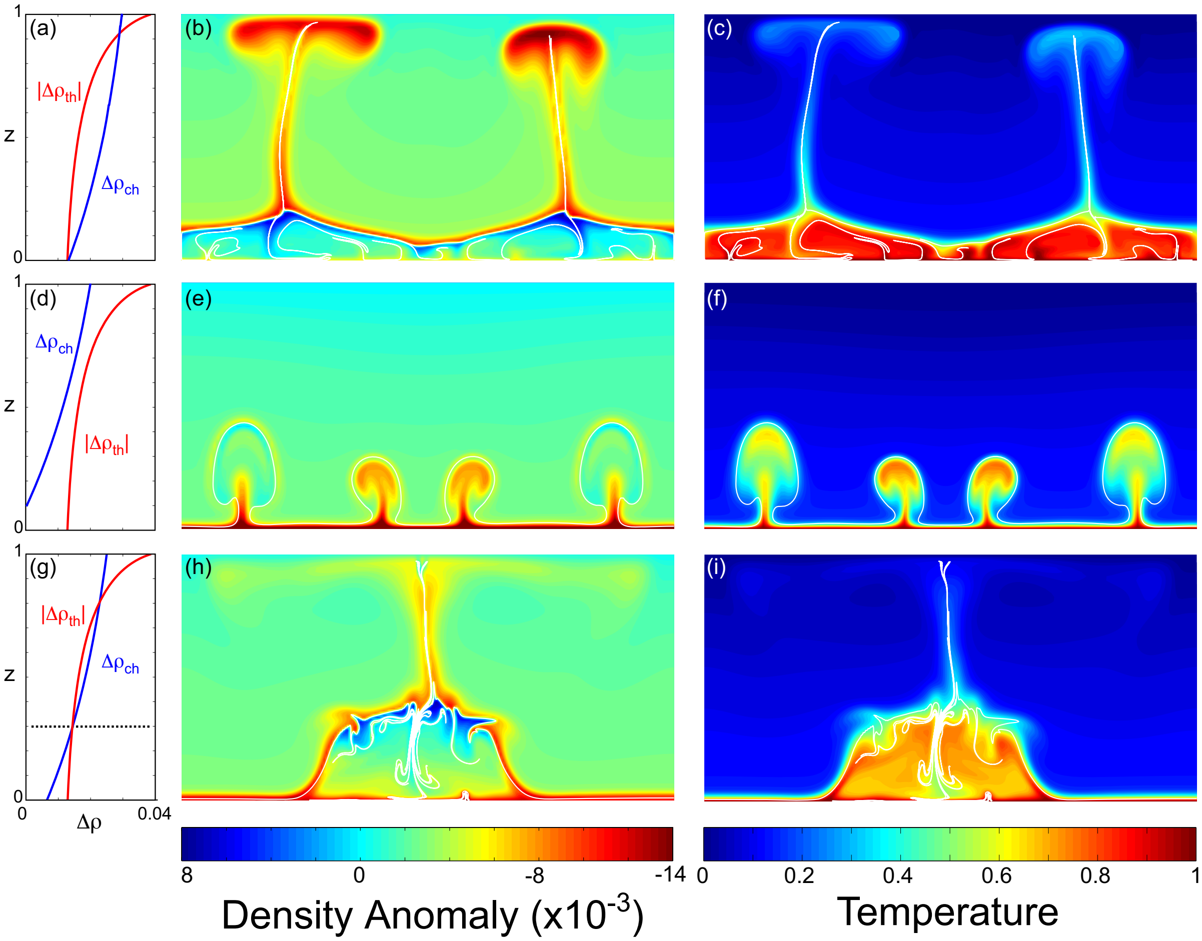

Figure 5-3. Three calculations with K_{S2}=1.06 and variable $\Delta\rho_0$. Top row: $\Delta\rho_0$=0.03; middle row: $\Delta\rho_0$=0.02; bottom row: $\Delta\rho_0$=0.025. Left column: predicted thermal (red) and chemical (blue) density anomalies; central column: density anomaly field; right column: temperature field. (a–c) The anomalous material forms a flat layer with cusps. These structures occur within the stable domain. (d–f) The anomalous material forms several plumes. These structures occur within the unstable domain. (g–i) The anomalous material forms a superplume with steep sides. These structures occur within the metastable domain.

studied since it occurs even when the bulk moduli of the two materials are identical. This domain is judged to be stable.

Second, when $\Delta\rho_0$ is sufficiently small for all K_{S2} investigated, even for moderate fractions of overturn times, the lower layer becomes quickly stirred into the upper layer (cross symbols in Figure 5-2; Figure 5-3D–F). The HNB is non-existent because $\Delta\rho_{total}$ is always negative. A range of morphological states can be found during a period when the dense layer is swept off of the bottom. Some of the morphology resembles that of a metastable superplume (Figure 5-3H) but can be distinguished by the unstable density structure. This regime has also been studied previously since it is well-expressed when the bulk moduli of the two material are identical.

Finally, for K_{S2} larger than 1.02, as $\Delta\rho_0$ is systematically increased, we find a zone of metastability between the two aforementioned states (circle symbols in Figure 5-2; Figure 5-3G–I). The dense layer is regionally swept off of the base and into a single superplume with steep sides and a roughly flat top slightly higher than the HNB. Thermal plumes emerge from the top of the superplume and entrain some of the anomalous material. The thermal plumes root either along the top of the superplume or along its edge, depending on initial conditions. Because $\Delta\rho_{ch}$ dominates over $\Delta\rho_{th}$ at depths above the HNB, the anomalous material near the top is denser and tends to descend to the HNB, while the opposite is true at the base of the superplume as the anomalous material tends to rise upward. The dynamic effect stabilizes the height of the superplume near the HNB and keeps the average density of the superplume close to neutral. Although the height of the superplume rises and lowers by about 10% as a function of time, the oscillation is not nearly as large as that found in the plume mode and so does not cause the two layers to rapidly stir together. There is a trade-off between $\Delta\rho_0$ and K_{S2}. Similar HNB and superplume morphology can be found by varying the two parameters simultaneously (Figure 5-2).

We find that Rayleigh number, initial thickness, and the rate of internal heating of the dense layer do not substantially influence the stability of the layer. The effect of internal heating is to increase the internal temperature of the superplume and, therefore, raise the HNB. Even for cases with substantial internal heating, the superplume remains metastable and only raises the level of its top surface. This means that superplumes can be metastable for a wide range of temperatures and persist for long periods of geological time as the mantle temperature and rate of internal heat generation decrease.

For a given $\Delta\rho_0$ and K_{S2}, the domain of metastability is greatly expanded compared with that from models with constant thermal expansion, in which the metastable regime exists only when thermal and chemical density anomalies nearly cancel each other. However, the metastable regime we find is particularly sensitive to the depth-dependence of the coefficient of thermal expansion, $\alpha(z)$. Using different $\alpha(z)$, in some cases the metastable regime shrinks and only exists when K_{S2} is greater than 1.1, while in other cases the metastable regime broadens, and metastable superplumes reach almost to the top of the convecting box.

5.5 Conclusion

From the dynamics, it seems likely that a range of lithologies might satisfy the increased density and bulk modulus we require. We show that the inferred physical properties of superplume material are plausible. For example, pyroxenite, commonly associated with subducted oceanic crust [*Hauri*, 1996], has been shown to be 2% denser with a 5% higher K_S than the PREM value under high pressure-temperature conditions [*Lee et al.*, 2005]. The trade-off between $\Delta\rho_{ch}$ and K_{S2} in our dynamic model and the uncertainty in the high pressure experiment preclude us from uniquely identifying pyroxenite as the material of superplumes.

However, if superplumes consist of subducted oceanic crust, it could explain the spatial correlation of superplumes with the DUPAL geochemical anomaly [*Hart*, 1984]. In order for a large mass of oceanic crust to have accumulated at the core-mantle boundary without mixing with oceanic lithosphere, an efficient mechanism for the separation of oceanic crust with lithosphere is required [*Christensen and Hofmann*, 1994]. The hypothesis that superplumes consist of subducted oceanic crust can satisfy seismological, geodynamical, mineralogical, and geochemical constraints simultaneously.

References

Burke, K., and T. H. Torsvik (2004), Derivation of Large Igneous Provinces of the past 200 million years from long-term heterogeneities in the deep mantle, *Earth Planet. Sci. Lett., 227*, 531–538.

Christensen, U. R., and A. W. Hofmann (1994), Segregation of subducted oceanic-crust in the convecting mantle, *J. Geophys. Res.*, *99*, 19867–19884.

Davaille, A. (1999), Simultaneous generation of hotspots and superswells by convection in a heterogenous planetary mantle, *Nature, 402*, 756–760.

Dziewonski, A. M., and D. L. Anderson (1981), Preliminary reference earth model, *Phys. Earth Planet. Inter.*, *25*, 297–356.

Gurnis, M. (1986), The effects of chemical density differences on convective mixing in the Earth's mantle, *J. Geophys. Res., 91*, 1407–1419.

Hansen, U., and D. A. Yuen (1988), Numerical simulations of thermal-chemical instabilities at the core mantle boundary, *Nature*, *334*, 237–240.

Hart, S. R. (1984), A large-scale isotope anomaly in the southern-hemisphere mantle, *Nature*, *309*, 753–757.

Hauri, E. H. (1996), Major-element variability in the Hawaiian mantle plume, *Nature, 382*, 415–419.

Ishii, M., and J. Tromp (1999), Normal-mode and free-air gravity constraints on lateral variations in velocity and density of Earth's mantle, *Science*, *285*, 1231–1236.

Ita, J., and S. D. King (1994), Sensitivity of convection with an endothermic phase-change to the form of governing equations, initial conditions, boundary conditions, and equation of state, *J. Geophys. Res.*, *99*, 15919–15938.

Jellinek, A. M., and M. Manga (2002), The influence of a chemical boundary layer on the fixity, spacing and lifetime of mantle plumes, *Nature*, *418*, 760–763.

Karato, S., and B. B. Karki (2001), Origin of lateral variation of seismic wave velocities and density in the deep mantle, *J. Geophys. Res.*, *106* , 21771–21783.

King, S. D., A. Raefsky, and B. H. Hager (1990), Conman - vectorizing a finite-element code for incompressible 2-dimensional convection in the Earth's mantle, *Phys. Earth Planet. Inter.*, *59*, 195–207.

Lee, K. K., P. D. Asimow, and O. Tschauner (2005), Phase assemblage and stability of pyroxenite at Lower-Mantle conditions, *Eos Trans. AGU, 86*, Jt. Assem. Suppl., Abstract V42A-02.

Masters, G., G. Laske, H. Bolton, and A. M. Dziewonski (2000), The relative behavior of shear velocity, bulk sound speed, and compressional velocity in the mantle: implications for chemical and thermal structure, in *Earth's Deep Interior*, edited by S. Karato, A.M. Forte, R.C. Liebermann, G. Masters, and L. Stixrude, pp. 63–87, AGU, Washington DC.

McNamara, A. K., and S. Zhong (2004), Thermochemical structures within a spherical mantle: Superplumes or piles? *J. Geophys. Res.*, *109*, B07402, doi:10.1029/2003JB002847.

Ni, S., E. Tan, M. Gurnis, and D. Helmberger (2002), Sharp sides to the African superplume, *Science*, *296*, 1850–1852.

Ni, S., and D. V. Helmberger (2003), Further constraints on the African superplume structure, *Phys. Earth Planet. Inter.*, *140*, 243–251.

Romanowicz, B. (2001), Can we resolve 3D density heterogeneity in the lower mantle? *Geophys. Res. Lett.*, *28,* 1107–1110.

Sidorin, I., and M. Gurnis (1998), Geodynamically consistent seismic velocity predictions at the base of the mantle, in *The Core-Mantle Boundary Region*, edited by M. Gurnis, M.E. Wysession, E. Knittle, and B.A. Buffett, pp. 209–230, AGU, Washington DC.

Su, W. J., and A. M. Dziewonski (1997), Simultaneous inversion for 3-D variations in shear and bulk velocity in the mantle, *Phys. Earth Planet. Inter.*, *100*, 135–156.

Tackley, P. J. (1998), Three-dimensional simulations of mantle convection with a thermo-chemical basal boundary layer: D"?, in *The Core-Mantle Boundary Region*, edited by M. Gurnis, et al., pp. 231–253, AGU, Washington DC.

To, A., B. Romanowicz, Y. Capdeville, and N. Takeuchi (2005), 3D effects of sharp boundaries at the borders of the African and Pacific Superplumes: Observation and modeling, *Earth Planet. Sci. Lett.*, *233*, 137–153.

Wang, Y., and L. Wen (2004), Geometry and P- and S- velocity structures of the "African Anomaly", *Eos Trans. AGU*, *85,* Fall Meet. Suppl., Abstract S53B-0221.

Wen, L. (2001), Seismic evidence for a rapidly varying compositional anomaly at the base of the Earth's mantle beneath the Indian Ocean, *Earth Planet. Sci. Lett.*, *194,* 83–95.

Wen, L., P. Silver, D. James, and R. Kuehnel (2001), Seismic evidence for a thermo-chemical boundary at the base of the Earth's mantle, *Earth Planet. Sci. Lett.*, *189*, 141–153.

Chapter 6

Compressible thermo-chemical convection and application to lower mantle superplumes

Abstract

A new finite element code for compressible thermo-chemical convection is developed to study the stability of a chemical layer at the base of the mantle. Using composition-dependent compressibility and density at the surface, a composition-dependent density profile is derived. Together with depth-dependent thermal expansion, this combination of parameters yields a wide range of dynamic evolutions for the chemical layer. The chemical structures are classified in five major categories, classical plumes, mushroom-shaped plume, metastable domes, ridges, and continuous layers, and a few abnormal cases, such as hourglass-shaped plumes and columnar plumes. The dynamic evolution of each category is described in detail. Several models have a chemical structure morphologically similar to the superplumes at a single time. Correspondingly, several dynamic scenarios are proposed for the dynamic nature of the superplumes, including plumes at early stage, plume clusters, ridges, passive piles, sluggish domes, and metastable domes. We convert these dynamic models into seismic velocity anomalies. The thermo-elastic parameters used in the conversion are additional constraints. We compare the density structure with normal mode inversion, the seismic signature of the converted seismic anomalies with seismic observations, and the required thermo-elastic parameters with mineral physics data. Among the proposed scenarios, only the scenario of metastable domes satisfies all constraints simultaneously. The implication on the geochemistry and mineralogy of the superplumes is discussed.

6.1 Introduction

The large density contrast between the mantle and core, the largest in Earth's interior, facilitates the accumulation of chemical heterogeneity. Seismic image shows strong seismic velocity variations at the base of the mantle (cf. reviews by *Lay et al*. [1998] and *Garnero* [2000]). The seismic velocity variation is too strong to be explained solely by temperature variation [*Karato and Karki*, 2001] and must involve phase or compositional variations, or some combination. There are three possible phase changes in the lower mantle. Two of them have been associated with seismic observations. The D'' discontinuity [*Lay and Helmberger*, 1983], attributed to the perovskite to post-perovskite phase change [*Sidorin et al.*, 1999b; *Murakami et al.*, 2004; *Oganov and Ono*, 2004], and the ultra-low velocity zones (ULVZs) [*Garnero and Helmberger*, 1996], attributed to partial melting [*Williams and Garnero*, 1996; *Wen and Helmberger*, 1998; *Rost et al.*, 2005] are evidences of phase heterogeneity. The third phase change, the high to low spin transition of Fe [*Badro et al.*, 2004], is another potential source of phase heterogeneity. The transition of this phase change may span a broad range of pressures [*Sturhahn et al.*, 2005]. If so, this phase change will not constitute a sharp seismic discontinuity and will be difficult to observe seismologically.

Chemical heterogeneity in the lower mantle has been proposed as an explanation for observed isotopic heterogeneity in oceanic basalts [*Allegre et al.*, 1980]. To satisfy isotopic observations, chemical reservoirs must be isolated from the upper mantle for billions of years [*Brooks et al.*, 1976]. Earlier, much of this chemical heterogeneity was thought to be associated with the seismic discontinuity at 660 km depth [*Jacobsen and Wasserburg*, 1979]. Advances in seismic tomography, showing images of subducted slabs penetrating into the lower mantle, excludes chemical layering at 660 km depth [*Grand et al.*, 1997; *van der Hilst et al.*, 1997]. A deeper chemical boundary, at 1000–1500 km depth, with high relief was later proposed [*Kellogg et al.*, 1999]. Such a chemical boundary, accompanied with a hot thermal boundary layer, should be observable by seismic tomography [*Tackley*, 2002], but none has been observed at this depth [*Castle and van der Hilst*, 2003].

Tomography reveals a degree-2 pattern of seismic velocity anomalies near the bottom of the mantle [*Grand et al.*, 1997; *Su and Dziewonski*, 1997; *van der Hilst et al.*, 1997; *Ritsema et al.*, 1999; *Kuo et al.*, 2000; *Masters et al.*, 2000; *Megnin and Romanowicz*, 2000; *Montelli et al.*, 2004; *Trampert et al.*, 2004]. Two prominent regions with low seismic velocity are found beneath the southern Africa and the southwestern Pacific, surrounded by high seismic velocities. The high velocity anomalies, whose geographic location matches ancient subduction zones, have been interpreted as subducted slabs [*Richards and Engebretson*, 1992] and thought to be colder than the regions they surround. On the other hand, both low velocity regions display large positive geoid anomalies, shallow seafloor and elevated topography, and extensive hotspot volcanism [*Nyblade and Robinson*, 1994; *McNutt*, 1998]. Together with a correlation with the erupted location of Large Igneous Provinces [*Burke and Torsvik*, 2004], these observations suggest that the low velocity seismic structures are warmer than surrounding mantle. These regions have been called “superplumes”, although uncertainties remain as to their nature. We will adopt the term “superplume” to describe these regions, although the regions may not be buoyant upwellings.

The anti-correlation of shear wave velocity anomaly δV_S with bulk sound velocity anomaly δV_ϕ [*Su and Dziewonski*, 1997; *Ishii and Tromp*, 1999; *Masters et al.*, 2000], anti-correlation of δV_S and density anomaly $\delta\rho$ [*Ishii and Tromp*, 1999; *Resovsky and Trampert*, 2003; *Ishii and Tromp*, 2004], spatially sharp reductions in shear wave velocity V_S [*Wen*, 2001; *Ni et al.*, 2002; *To et al.*, 2005], and spatial correlation with geochemical anomalies [*Castillo*, 1988] suggest that the superplumes have a composition distinct from ambient mantle. The sharp reduction in V_S indicates the presence of a chemical boundary. Moreover, the chemical boundary of the southern African superplume is found to extend 1200 km above the core-mantle boundary (CMB) with a width of 1000 km and a length of 7000 km [*Ni et al.*, 2002; *Ni and Helmberger*, 2003a; 2003b; 2003c]. The average δV_S of the southern African superplume is about -3%, while the average compressional wave velocity anomaly δV_P is about -0.5%. The morphological and seismic signatures of this part of African superplume are diagnostic of its dynamics. Another important diagnostic is that superplumes are denser than its surroundings [*Ishii and Tromp*, 1999; *Ishii and Tromp*, 2004; *Trampert et al.*, 2004]. The African superplume is sometimes described as a "ridge" based on its elongated horizontal extent [e.g., *Ni and Helmberger*, 2003b]. However, in this paper, we reserve the word "ridge" to a structure with a triangular vertical cross-section.

The fate of a dense chemical layer at the base of the convecting mantle has been investigated extensively [*Christensen*, 1984; *Gurnis*, 1986; *Hansen and Yuen*, 1988; *Olson and Kincaid*, 1991; *Farnetani*, 1997; *Tackley*, 1998; *Davaille*, 1999; *Montague and Kellogg*, 2000; *Gonnermann et al.*, 2002; *Jellinek and Manga*, 2002; *Ni et al.*, 2002; *Namiki*, 2003; *McNamara and Zhong*, 2004]. A chemical layer, stabilized by an intrinsic density anomaly $\Delta\rho_{ch}$ tends to remain at the CMB. Later, as the layer heats up, its density decreases by $\Delta\rho_{th}$. The (negative) thermal density anomaly $\Delta\rho_{th}$, which is proportional to $\rho_r \alpha \delta T$, depends on the reference density ρ_r, the coefficient of thermal expansion α, and the temperature anomaly of the material δT. The net density anomaly is $\Delta\rho_{ch}$-$\Delta\rho_{th}$. The chemical and thermal effects compete in controlling the stability of the layer. Consider a parcel of chemically anomalous material at the CMB: As the parcel heats up, δT increases, and so does $\Delta\rho_{th}$. When $\Delta\rho_{th}$ becomes equal to or greater than $\Delta\rho_{ch}$, the parcel becomes unstable and rises upward. The parcel can lose heat by thermal diffusion or adiabatic cooling during ascent and subsequently restabilize. The change in stability depends on the rate of heat loss and the depth dependence of various aforementioned parameters.

When $\Delta\rho_{ch}$ is small, the layer becomes unstable with a small temperature increase, eventually forming a thermo-chemical plume, such that the layer becomes stirred with the rest of the mantle. On the other hand, when $\Delta\rho_{ch}$ is sufficiently large, the layer remains stable with small topography on the interface between the intrinsically dense and ambient regions. Only when $\Delta\rho_{ch}$ is within a narrow range of intermediate values can the layer have high topography on its interface.

In most previous studies, the reference density and coefficient of thermal expansion were assumed to be constant with depth. However, the compression at the large pressure of the lower mantle increases the density and decreases the coefficient of thermal expansion. From the PREM model [*Dziewonski and Anderson*, 1981], the average density increases from 3380 kg/m^3 at the base of lithosphere to 5560 kg/m^3 at the CMB. The coefficient of thermal expansion of the mantle is 5x10^{-5} K^{-1} at the base of lithosphere. The magnitude of the coefficient of thermal expansion in the lower mantle is not as well-known. At 2000 km depth, for example, the coefficient of thermal expansion for perovskite is estimated to be 1.5x10^{-5} K^{-1} [*Oganov et al.*, 2001] or 1.3x10^{-5} K^{-1} [*Marton and Cohen*, 2002]. The coefficients of thermal expansion of several types of mantle rock have been estimated to have

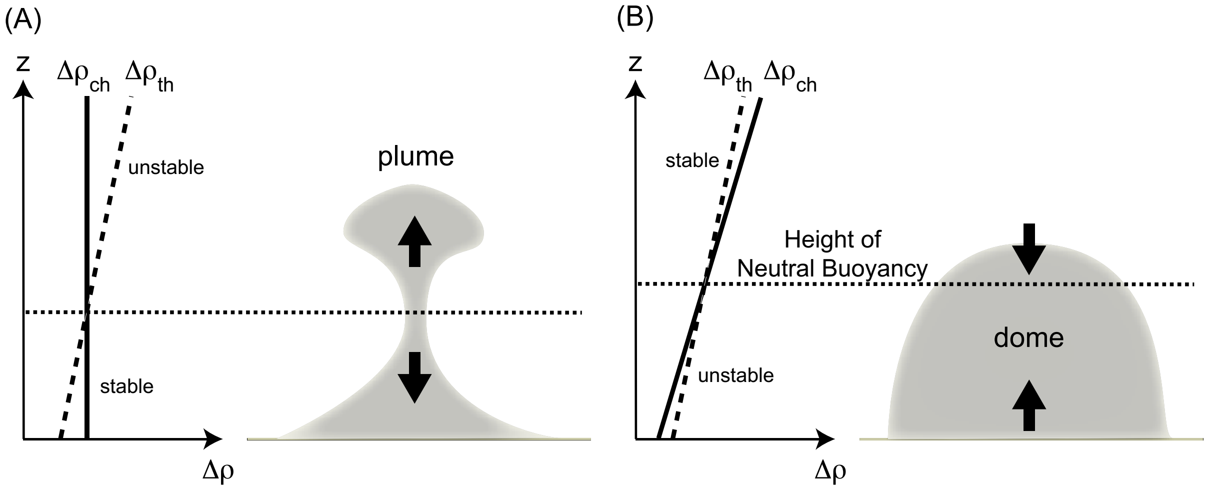

Figure 6-1. Density anomaly profiles. (A) When $\Delta\rho_{ch}$ is constant with depth, at some depth, the chemical and thermal density anomalies are equal and the net density anomaly is 0. The net density anomaly is negative above the depth and positive below. (B) When $\Delta\rho_{ch}$ is also depth-dependent, and changes faster than $\Delta\rho_{th}$, the trend of the density profile can be reversed. The net density anomaly is positive above the HNB and negative below.

a similar value of $1.3\text{x}10^{-5}$ K^{-1} [*Hama and Suito*, 2001]. Consequently, the product of $\rho_r\alpha$ decreases with depth and the stability of chemically anomalous material will be depth-dependent.

In most previous studies, the chemical density anomaly is assumed to be constant with depth. However, materials with different compressibility will have different adiabatic density profiles. Highly compressible (low bulk modulus) material has a steeper adiabatic density profile than less compressible (high bulk modulus) material. The difference between the density profiles is the chemical density anomaly profile. As a result, after accounting for compressibility, the chemical density profile can be depth-dependent.

Considering a mantle with an anomalous chemical composition, which has a depth-dependent thermal density anomaly and is warmer than its surroundings, the lower portion of the structure is denser than the surrounding mantle while the upper portion less dense (Figure 6-1A). At some depth, the chemical and thermal density anomalies are equal and the net density anomaly is 0. The net density anomaly is negative above that depth but positive below. Material above this depth tends to move upward and becomes even less stable as it does so. Material below this depth tends to move downward, becoming more stable. As a result, the upper portion of the chemical structure will become a plume, while the lower portion will become a flat layer with a cusp. The conclusion of this simple analysis suggests that a stable thermo-chemical structure with high topography is difficult to produce with an Earth-like thermal expansion profile [*Ni et al.*, 2002].

On the other hand, if $\Delta\rho_{ch}$ is not constant and changes faster than $\Delta\rho_{th}$, the trend of density profile can reverse. The height above the CMB where the chemical and thermal density anomalies are equal is called the height of neutral buoyancy (HNB). The net density anomaly is positive above the HNB but negative below. The lower portion of the chemical structure is less dense and rises. Both the thermal and chemical density anomalies increase during the ascent. If the later increases faster than the former, upon rising above the HNB, the chemically anomalous material becomes denser than the surrounding mantle and starts sinking (Figure 6-1B). With this scenario, a heated dense material can form a metastable dome with high relief [*Tan and Gurnis,* 2005].

Although the mantle is compressible, most dynamic models utilize the Boussinesq approximation (an approximation for incompressible flow) for mathematical and numerical simplicity. Various compressible convection models have been developed [*Jarvis and McKenzie*, 1980; *Baumgardner*, 1985; *Glatzmaier*, 1988; *Machetel and Yuen*, 1989; *Schmeling*, 1989; *Steinbach et al.*, 1989; *Leitch et al.*, 1991; *Quareni et al.*, 1991;

Balachandar et al., 1992; *Bercovici et al.*, 1992; *Ita and King*, 1994; *Solheim and Peltier*, 1994; *Tackley*, 1996; *Zhang and Yuen*, 1996; *Bunge et al.*, 1997]. The main effect of compressibility is to introduce adiabatic density and temperature gradients, which reduce the vigor of convection. However, when variation in chemical composition is included, another effect of compressibility can significantly change the pattern of the convection. The density contrast between materials of different compressibility and, therefore, of different density profiles, can vary in magnitude and sign as a function of depth. As a result, compressible thermo-chemical convection models exhibit complex dynamics not seen in incompressible thermo-chemical convection models [*Xie and Tackley*, 2004; *Nakagawa and Tackley*, 2005; *Farnetani and Samuel*, 2005; *Tan and Gurnis*, 2005].

In this paper, we will describe our numerical methods for compressible thermo-chemical convection. We will systematically explore the effect of composition-dependent density profiles and depth-dependent thermal expansion on the stability of a basal dense chemical layer. We find a wide range of dynamic evolution for the chemical layer. Several models have a chemical structure with similar morphology to that of the superplumes. We convert these dynamic models into seismic velocity anomalies. The thermo-elastic parameters used in the conversion are additional useful constraints. We compare the seismic signature of the converted model with seismic observation and the required thermo-elastic parameters with mineral physics data to find the preferred dynamic models.

6.2 Methods

We use the Truncated Anelastic Liquid Approximation (TALA) [*Ita and King*, 1994] as the governing equations in 2D (x, z) Cartesian coordinate system. The continuity equation is

$$\nabla \cdot (\rho_r \mathbf{u}) = 0 \qquad (6\text{-}14)$$

where $\mathbf{u}=(u_x, u_z)$ is the velocity vector, and $\rho_r=\rho_r(z)$ is the reference density profile.

The momentum equation is

$$-\nabla P + \nabla \cdot \underline{\tau} = \mu^{-1}(\Delta\rho_{ch}C - \mu\rho_r \alpha T) g Ra\, \mathbf{e}_z \qquad (6\text{-}15)$$

where P is the dynamic (non-hydrostatic) pressure; $\underline{\tau}$ is the deviatoric stress tensor; μ is a non-dimensional number related to thermal expansion (defined later); $\Delta\rho_{ch}=\Delta\rho_{ch}(z)$ is the chemical density anomaly profile; C is the concentration (between 0 to 1) of the anomalous material; $\alpha=\alpha(z)$ is the coefficient of thermal expansion; T is the temperature; g is the gravity; Ra is the Rayleigh number; $\mathbf{e}_z$ is the unit vector in the vertical direction. The term inside the parentheses is the net density anomaly $\Delta\rho$. In TALA, the effect of the dynamic pressure on the density is ignored, as justified previously [*Jarvis and McKenzie*, 1980].

The energy equation is

$$\rho_r C_P \frac{\partial T}{\partial t} = -\rho_r C_P \mathbf{u} \cdot \nabla T \;+\; \nabla \cdot (k_T \nabla T) + Di(T + T_s)\rho_r \alpha g u_z + \frac{Di}{Ra}\underline{\tau} : \underline{\varepsilon} + \rho_r H \qquad (6\text{-}16)$$

where C_P is the heat capacity at constant pressure; t is the time; k_T is the thermal conductivity; Di is the dissipation number; T_s is the surface temperature; $\underline{\varepsilon}$ is the deviatoric strain rate tensor; H is the internal heating rate. The right-hand side terms are the advection, diffusion, adiabatic cooling, viscous dissipation, and internal heating, respectively.

The constitutive relationship is

$$\underline{\tau} = 2\eta\left(\underline{\varepsilon} - \frac{1}{3}(\nabla \cdot \mathbf{u})\underline{I}\right) \qquad (6\text{-}17)$$

where η is the viscosity, and $\underline{I}$ is the identity tensor. The components of the deviatoric strain rate tensor are

$$\begin{aligned}\varepsilon_{xx} &= \frac{\partial u_x}{\partial x}\\ \varepsilon_{zz} &= \frac{\partial u_z}{\partial z}\\ \varepsilon_{xz} = \varepsilon_{zx} &= \frac{1}{2}\left(\frac{\partial u_x}{\partial z} + \frac{\partial u_z}{\partial x}\right)\end{aligned} \qquad \text{(6-18)}$$

The Rayleigh number is $Ra=\rho_0 g_0 \alpha_0 \Delta T_{total} h^3/\kappa_0 \eta_0$, where ρ_0 is the characteristic density; g_0 is the characteristic gravity; α_0 is the characteristic coefficient of thermal expansion; ΔT_{total} is the total temperature contrast; h is the depth of the computation domain; κ_0 is the characteristic thermal diffusivity; η_0 is the characteristic viscosity. The dissipation number is $Di=\alpha_0 g_0 h/C_{P0}$, where C_{P0} is the characteristic heat capacity at constant pressure. Two other useful non-dimensional parameters are the Gruneisen parameter $\gamma= \alpha_0 K_{S0}/\rho_0 C_{P0}$, where K_{S0} is the characteristic bulk modulus; and the fraction of volume change due to thermal expansion $\mu=\alpha_0 \Delta T_{total}$.

We modified the finite-element code ConMan [*King et al.*, 1990] by incorporating compressibility. The original code uses the penalty function formulation [*Hughes*, 2000], where pressure is treated as a dependent variable of velocity, and the stiffness matrix is penalized by the pressure term. Our modified code uses the mixed method formulation [*Hughes*, 2000], where velocity and pressure are treated as independent variables. The stiffness matrix is assembled from each element stiffness matrix k^e. k^e can be written as

$$k^e = \underset{\substack{a,b\\ i,j}}{\mathbf{A}}\left[e_i^T\left(\int_{element} B_a^T D_\eta B_b \, d\Omega\right)e_j\right] \qquad \text{(6-19)}$$

where $\mathbf{A}$ is the assembling operator; indices a and b are elemental node indices; indices i and j are directional indices; e_i and e_j are unit direction vectors. B_a and D_η are defined as

$$B_a = \begin{bmatrix} N_{a,x} & 0 \\ 0 & N_{a,y} \\ N_{a,z} & N_{a,x} \end{bmatrix} \tag{6-20}$$

$$D_\eta = \eta \begin{bmatrix} 4/3 & -2/3 & 0 \\ -2/3 & 4/3 & 0 \\ 0 & 0 & 1 \end{bmatrix} \tag{6-21}$$

where N_a and N_b are the shape functions of node *a* and *b*, respectively; $N_{a,x}$ and $N_{a,y}$ are the partial derivatives of N_a in x and y direction, respectively. Note that the element stiffness matrix is different from the formulation of *King et al.* [1990] in two ways. The element stiffness matrix is not penalized by the pressure term and contains the contribution of volumetric change due to compression.

Equation (6-1) can be rearranged as

$$\nabla \cdot \mathbf{u} + \frac{1}{\rho_r}\frac{\partial \rho_r}{\partial z} u_z = 0 \tag{6-22}$$

After discretization, the resultant matrix equations of Equation (6-2) and (6-9) become

$$\begin{bmatrix} K & B^T \\ B + C_\beta & 0 \end{bmatrix} \begin{bmatrix} u \\ p \end{bmatrix} = \begin{bmatrix} b \\ 0 \end{bmatrix} \tag{6-23}$$

where K is the stiffness matrix; B is the divergence operator, whose transpose B^T is the gradient operator; C_β is a constant matrix corresponding to the second term in Equation (6-9); b is the force vector. This matrix system is asymmetric because of the non-zero C_β. We adapted the pressure correction algorithm [*Ramage and Wathen*, 1994] and used the Bi-Conjugate Gradient Stabilized method [*Barrett et al.*, 1994] to solve the equations iteratively. The algorithm is described in Table 6-1. The inverse of the stiffness matrix K^{-1} is calculated outside the iteration loop. As a result, computing each iteration involves only matrix-vector

Table 6-1. Algorithm to solve Equation (6-10). Symbols used here are not related to symbols in other equations.

```
$p_0 = 0$                                  initialize pressure vector
$u_0 = K^{-1} b$                           initial guess of velocity
$r_0 = (B+C_\rho) u_0$                     calculate initial residual
$z = r_0$                                  choose conjugate residual
$i = 1$                                    initialize iteration count
$\rho_0 = 1$
begin loop                                 start iteration
    $\rho_i = (z, r_{i-1})$                compute convergence criterion
    if $\rho_i = 0$, method fails
    if $\rho_i < \varepsilon$, stop loop   $\varepsilon$ is a small positive number
    if $i = 1$
        $q_i = r_{i-1}$                    initial search direction for pressure
    else
        $\beta = (\rho_i / \rho_{i-1})(\alpha_{i-1}/\omega_{i-1})$
        $q_i = r_{i-1} + \beta (q_{i-1} - \omega_{i-1} d_{i-1})$    update pressure search direction
    end if
    $v_i = K^{-1} B^T q_i$                 new search direction for velocity
    $d_i = (B+C_\rho) v_i$                 new search direction for pressure
    $\alpha_i = \rho_i / (z, d_i)$         set step length
    $s = r_{i-1} - \alpha_i d_i$           update residual
    if norm($s$) is too small, stop loop   if the norm of $s$ is too small, further
                                           update won't be beneficial
    $w_i = K^{-1} B^T s$                   new search direction for velocity
    $t = (B+C_\rho) w_i$                   new search direction for pressure
    $\omega_i = (t, s)/(t, t)$             set step length
    $p_i = p_{i-1} + \alpha_i q_i + \omega_i s$    update pressure
    $u_i = u_{i-1} - \alpha_i v_i - \omega_i w_i$  update velocity
    $r_i = s - \omega_i t$                 update residual
    $i = i+1$                              update iteration count
end loop
```

and vector-vector contractions. We developed an analytical solution for compressible convection and benchmarked our numerical result with the analytical result (Appendix D).

The energy equation (6-3) is solved using a Streamline Upwind Petrov-Galerkin scheme [*Brooks and Hughes*, 1982]. Each term on the right-hand side of Equation (6-3), except the viscous dissipation, is computed on the element level. The viscous dissipation is calculated using nodal stress and strain rate to improve numerical accuracy. The solution of the energy equation is benchmarked in Appendix E.

The composition field is computed using the marker chain method [*Davies and Gurnis*, 1986; *van Keken et al.*, 1997]. The marker chain is advected using a fourth order predictor-corrector scheme. If the distance between two adjacent markers is greater than a predefined threshold, a new marker is inserted in between them. The marker chain defines the material interface. Because of material entrainment, the length of the marker chain grows exponentially with time. The computational efficiency of the marker chain method severely deteriorates if there is substantial material entrainment, in which case we halt the computation. For some halted models, the marker chain is trimmed to remove excess entrainment, and the computation restarted in order to proceed further. The trimming of the marker chain introduces error in the composition field, but the magnitude of the error is estimated to be small and does not influence the stability of the chemical layer.

Potentially, thermodynamics and transport properties of chemically distinct materials could be composition-dependent. For the sake of simplicity, only the bulk modulus and density are assumed compositionally dependent. The adiabatic density of the ambient mantle (material 1) ρ_{S1} is calculated by integrating the self-compression equation

$$\begin{aligned} & dP_H = -\rho_r g dz \\ & d\rho_{S1} = \frac{Di}{\gamma} K_{S1} \rho_{S1} dP_H \\ & \rho_{S1} = 1, \text{ at } z = 1 \end{aligned} \qquad (6\text{-}24)$$

where $P_H=P_H(z)$ is the hydrostatic pressure; $K_{S1}=1$ is the bulk modulus of the ambient mantle. The reference density profile ρ_r is set as ρ_{S1}. The adiabatic density ρ_{S2} of the anomalous material (material 2) with bulk modulus K_{S2} is calculated by

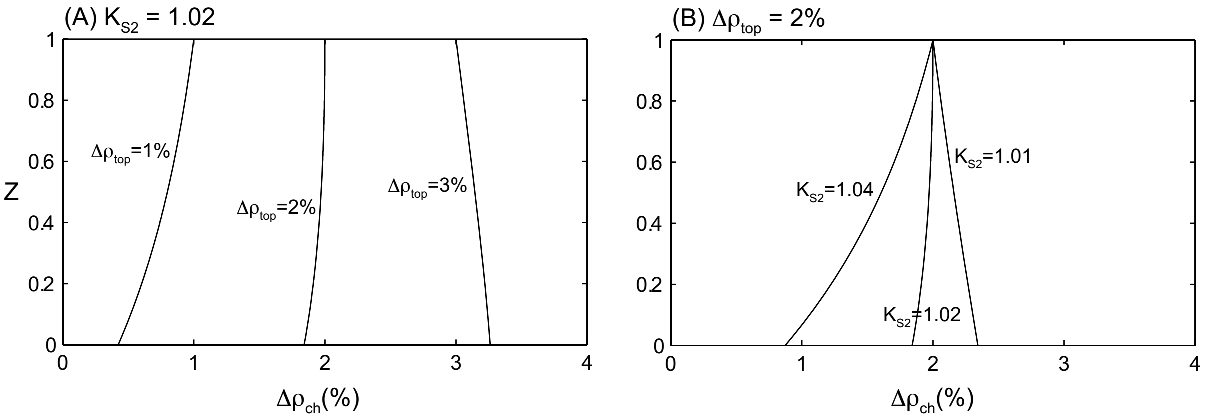

Figure 6-2. Various chemical density profiles. (A) $K_{S2}=1.02$, $\Delta\rho_{top}=1\text{-}3\%$. The slope of $\Delta\rho_{ch}$ changes from positive to vertical and finally to negative. (B) $\Delta\rho_{top}=2\%$ $K_{S2}=1.01\text{-}1.04$. The slope of $\Delta\rho_{ch}$ changes from negative to vertical and finally to positive.

$$\begin{aligned} d\rho_{S2} &= \frac{Di}{\gamma} K_{S2}\rho_{S2} dP_H \\ \rho_{S2} &= 1 + \Delta\rho_{top}, \text{ at } z = 1 \end{aligned} \qquad (6\text{-}25)$$

The density difference at the top surface $\Delta\rho_{top}$ and K_{S2} vary between models. The chemical density profile $\Delta\rho_{ch}=\rho_{S2}-\rho_{S1}$ is the difference between ρ_{S2} and ρ_{S1}. The non-dimensional parameter $\Delta\rho_{top}/\rho_0\varepsilon_T$ is commonly referred to as the Buoyancy number.

Different combinations of ρ_{top} and K_{S2} can produce chemical density profiles of different slopes $d\Delta\rho_{ch}/dz$. For example, fixing K_{S2} while increasing $\Delta\rho_{top}$ will change the slope of $\Delta\rho_{ch}$ from positive to zero and finally to negative (Figure 6-2A). On the other hand, fixing $\Delta\rho_{top}$ while increasing K_{S2} will change the slope from negative to zero and finally to positive (Figure 6-2B). We do not consider cases of $K_{S2}<1$ because seismic observations require the superplumes to have high K_S (see Discussion).

The coefficient of thermal expansion varies linearly in z in the models, $\alpha=\alpha_{CMB}+m_\alpha z$, instead of as an anharmonic equation [*Anderson*, 1967], for simplicity. The coefficient of thermal expansion at the CMB, α_{CMB}, is fixed in all models, corresponding to 0.9x10^{-5} K^{-1} [Table 7.3 in *Davies*, 1999]. We fix the value of α_{CMB} because of the direct trade-off with $\Delta\rho_{top}$. Increasing both α_{CMB} and $\Delta\rho_{top}$ will increase $\Delta\rho_{th}$ and $\Delta\rho_{ch}$, respectively. Since the stability is affected by the difference between $\Delta\rho_{th}$ and $\Delta\rho_{ch}$, changing both density anomalies in the same direction will not affect the dynamics substantially. Therefore, we vary $\Delta\rho_{top}$ while fixing α_{CMB}. The value of m_α varies between models. We did not incorporate composition-dependent thermal expansion in the models because α of the lower mantle materials remain poorly constrained.

The viscosity is temperature and depth dependent according to the equation

$$\eta = \exp\left(\frac{E_\eta + V_\eta (1 - z)}{T + T_\eta} - \frac{E_\eta}{T_\eta} \right) \tag{6-26}$$

where E_η is the activation energy; V_η is the activation volume; T_η is the temperature offset. The magnitude of this depth-dependence is chosen to compensate for the effect of adiabatic temperature gradients. The viscosity has a minimum cutoff of 10^{-3}.

In this study, we only consider variation in the adiabatic density profile ρ_r and the coefficient of thermal expansion α. Other physical properties are assumed constant with depth and composition. The difference between the thermal and chemical buoyancies drives the convection. Variations in the depth- and composition-dependence of ρ_r and α change the chemical and thermal buoyancies, respectively. These parameters potentially can reverse the sign of the buoyancy and greatly change the flow pattern. Other material properties (e.g., thermal diffusivity, heat capacity, and viscosity) are not directly involved in the buoyancy term. Although these material properties can be depth- and composition-dependent, they can affect the flow through changing the local Rayleigh number. The magnitude of the buoyancy might change, but not the sign. Therefore, the profiles of ρ_r and α have a profound influence on the flow pattern.

We have not incorporated any phase change into our calculation. The existence of partial meltings, inferred from ULVZs, is confined at the very base of the mantle, maybe ~40 km above the CMB, and localized horizontally. The dynamic consequence of partial meltings on lower mantle convection is probably insignificant. Another phase change, the post-perovskite (PPV) phase change, has a positive Clapeyron slope (8-10 MPa/K) and a 120 GPa transition pressure (corresponding to 200 km above the CMB) [*Tsuchiya et al.*, 2005]. Inside the chemical layer, the temperature could be so high that the PPV phase transition pressure is higher than that at the CMB. Actually, the D’’ discontinuity, thought to be caused by the PPV phase change, is rarely observed in the superplume region [*Helmberger et al.*, 2005]. The compositional dependence of the PPV phase change is actively being studied [*Mao et al.*, 2004; *Akber-Knutson et al.*, 2005; *Caracas and Cohen*, 2005; *Murakami et al.*, 2005; *Ono and Oganov*, 2005; *Hirose et al.*, 2006]. This phase change will destabilize the basal thermal boundary layer [*Sidorin et al.*, 1999a; *Nakagawa and Tackley*, 2004].

The computation domain is a 2x1 box with its bottom corresponding to the CMB. The top of the box, when scaled to the earth, is 2000 km above the CMB. The size of the box allows us to concentrate on lower mantle dynamics without the complexity of transition zone phase changes or subducted slabs. The top and bottom boundaries are free-slip and isothermal, with fixed temperature at 0 and 1, respectively. The sidewalls are reflecting. The initial temperature is adiabatic with a thin, basal thermal boundary layer. The chemical layer is initially flat with a thickness *d*. The values of all parameters are listed in Table 6-2.

Table 6-2. Values of parameters in models.

Symbol	Description	Value
ρ_0	characteristic density	4000 kg/m^3
g_0	characteristic gravity	10 m/s^2
α_0	characteristic coefficient of thermal expansion	3x10^{-5} K^{-1}
ΔT_{total}	total temperature contrast	1800 K
h	depth of computation domain	2000 km
κ_0	characteristic thermal diffusivity	1.27x10^{-6} m^2/s
η_0	characteristic viscosity	10^{22} Pa·s
C_{P0}	characteristic heat capacity at constant pressure	1500 kJ/kg
K_{S0}	characteristic bulk modulus	266.6 GPa
H	internal heating	0
Ra	Rayleigh number	2.2x10^6
Di	dissipation number	0.4
γ	Gruneisen parameter	1.333
T_s	surface temperature	0.75
μ	fraction of volume change due to thermal expansion	0.054
α_{CMB}	coefficient of thermal expansion at the CMB	0.3
E_η	activation energy of viscosity	11
V_η	activation volume of viscosity	-1.8
T_η	temperature offset of viscosity	-1.5
d	initial thickness of chemical layer	0.125

6.3 Results

We systematically explore the effect of K_{S2}, $\Delta\rho_{top}$, and m_α on the stability of the dense chemical layer. To gauge the parameter space, we estimate the height of neutral buoyancy (HNB) from a simple heuristic calculation. We calculate $\Delta\rho_{ch}$ using Equation (6-11) and (6-12) and $\Delta\rho_{th}=\mu\rho_{S2}\alpha\delta T$ by assuming δT=0.7. In dynamic models, δT varies with depth and between models, so the estimated HNB may not coincide with the real HNB. Nevertheless, this calculation represents a useful gauge of the parameter space. The two density anomaly profiles are compared. The HNB is defined as the height from the CMB where $\Delta\rho_{ch}$ and $\Delta\rho_{th}$ are equal. Another requirement of the HNB is that $\Delta\rho_{ch}$ must be less than $\Delta\rho_{th}$ below the height. We do not refer to this height as HNB when $\Delta\rho_{ch}$ is greater than $\Delta\rho_{th}$ below the cross-over. For example, there is no HNB is Figure 6-1A. We compute the estimated HNB in the 3D parameter space (Figure 6-3A). Later, we will see that the dynamic evolution of the chemical layer is primarily determined by the HNB and the value of $\Delta\rho_{ch}$ at the CMB, $\Delta\rho_{CMB}$.

It is clear from Figure 6-3A how the estimated HNB is affected by the three parameters. The estimated HNB is sensitive to the value of $\Delta\rho_{top}$. Increasing $\Delta\rho_{top}$, the HNB will move to a lower level. For any given K_{S2} and m_α, there is a $\Delta\rho_{top}$ above which $\Delta\rho_{ch}$ is greater than $\Delta\rho_{th}$ for all depths, and another $\Delta\rho_{top}$ below which $\Delta\rho_{ch}$ is less than $\Delta\rho_{th}$ for all depths. Between the two extremes, $\Delta\rho_{ch}$ intersects with $\Delta\rho_{th}$ in the mid-mantle, and the estimated HNB has a value between 0 and 1. The range of estimated HNB's expands significantly at large K_{S2} or small m_α.

Guided by Figure 6-3A, 130 numerical thermo-chemical convection models were calculated, each with distinct values of K_{S2}, $\Delta\rho_{top}$, and m_α. The range of parameter space explored is $1.02 \leq K_{S2} \leq 1.08$, $1.25\% \leq \Delta\rho_{top} \leq 3.75\%$, and $0.1 \leq m_\alpha \leq 0.7$. We find a wide range of thermo-chemical structures that we categorize in terms of morphology and evolution (Table 6-3). We calculate $\delta T = \delta T(z)$ by taking the horizontal temperature average in the region of $C > 0.8$ and use δT to infer $\Delta\rho_{th}$. We divide the result into three groups in terms of how the profiles of $\Delta\rho_{th}$ and $\Delta\rho_{ch}$ intersect: 1) the profiles never intersect, 2) they intersect and $\Delta\rho_{ch}$ dominates below the intersection, and 3) they intersect and $\Delta\rho_{th}$ dominates below the intersection. Within each group, two or more categories of evolution can be found. We will

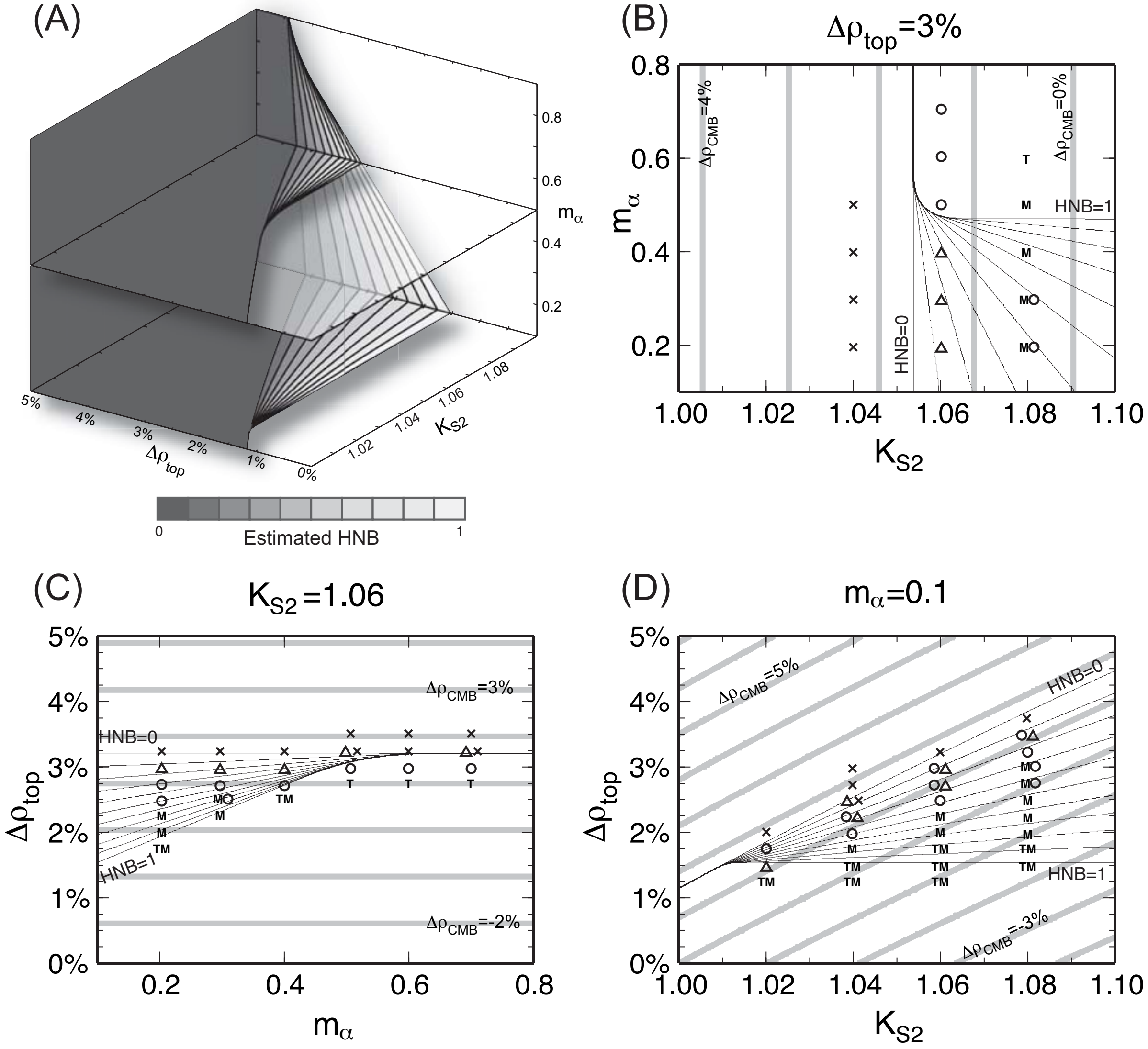

Figure 6-3. Parameter space. (A) Estimated HNB in the 3D (K_{S2}, $\Delta\rho_{top}$, m_{α}) parameter space. (B–D) Cross sections of the parameter space. (B) $\Delta\rho_{top}=3\%$ (C) $K_{S2}=1.06$ (D) $m_{\alpha}=0.1$. The thin contours are for the estimated HNB with an interval of 0.1. The thick, gray contours are for $\Delta\rho_{\mathrm{CMB}}$ with an interval of 1%. The outcomes of models are plotted with symbols. T: classical thermo-chemical plumes. M: mushroom-shaped plumes. ○: domes. Δ: ridges. ×: continuous layers.

present one model in each category, showing temperature, composition, and density fields and will describe the dynamic evolution of each.

Table 6-3. Summary of converted seismic models.

Category	**Plume**	**Mushroom**	**Dome**	**Ridge**	**Layer**
Preferred parameters	small $\Delta\rho_{top}$ small K_{S2} large m_α	small $\Delta\rho_{top}$ large K_{S2}	Intermediate $\Delta\rho_{top}$ and large m_α	Intermediate $\Delta\rho_{top}$ and small m_α	Large $\Delta\rho_{top}$ and small m_α
δT	variable	<0.6	0.7	0.8	>0.8
$\Delta\rho$	very buoyant	buoyant	neutral	neutral	dense
Stability	unstable	unstable	metastable	metastable	stable
HNB	>*d* or N/A	>*d*	>~*d*	~*d*	<*d* or N/A

6.3.1 No intersection

When the profiles of $\Delta\rho_{th}$ and $\Delta\rho_{ch}$ never intersect, two outcomes exist. If $\Delta\rho_{th}$ is always greater than $\Delta\rho_{ch}$, a small temperature increase in the chemical layer is sufficient to destabilize it. Several thermo-chemical plumes form and reach the top of domain. The plume heads impinge the top boundary and spread horizontally. All of the anomalous material is entrained into the plumes and transported to the top of the domain. The plumes have highly variable δT (Figure 6-4A). We call this category "classical thermo-chemical plumes" and labeled it "T" in Figure 6-3, mimicking the shapes of plume conduits and spreading plume heads. This category occurs at small $\Delta\rho_{top}$ and K_{S2} or at large m_α. This category should be very common at the parameter space of small $\Delta\rho_{top}$ and K_{S2} but is under-represented in our sampling of the parameter space. There are a few models of large K_S and m_α also produce classical thermo-chemical plumes. The early evolution of these models is similar to the evolution of models of "mushroom-shaped plumes" (described below). However, the large m_α in these models controls whether the plumes eventually rise to the surface.

On the other hand, if $\Delta\rho_{th}$ is always smaller than $\Delta\rho_{ch}$, the anomalous material forms a hot, continuous layer with δT greater than 0.8. The layer interface has small topography.

Thermal plumes rising above the layer entrain small amounts of anomalous material. Sharp cusps of the layer interface occur at the roots of thermal plumes (Figure 6-4B). We call this category "continuous layer" and label it with a cross (×) in Figure 6-3. This category occurs at large $\Delta\rho_{top}$ and small m_α.

6.3.2 $\Delta\rho_{ch}$ dominates below the intersection

When $\Delta\rho_{ch}$ dominates $\Delta\rho_{th}$ below the intersection, depending on the height of intersection, there are mainly two kinds of structures. First, if the height of intersection is low and close to the CMB, the whole layer can erupt as a plume, like the "classical thermo-chemical plumes" category above. Second, if the height of intersection is sufficiently high, such that the anomalous material never rises to this level, the layer remains at the CMB, akin to the "continuous layer" category.

6.3.3 $\Delta\rho_{th}$ dominates below the intersection

When $\Delta\rho_{th}$ dominates over $\Delta\rho_{ch}$ below the intersection, the height of intersection is the HNB. A broad range of dynamic evolutionary sequences can be found, depending on HNB and the magnitude of $\Delta\rho_{ch}$ at the CMB, $\Delta\rho_{CMB}$. If HNB is near the top of the computational domain, the whole layer can erupt as a plume, like the "classical thermo-chemical plumes" category. If HNB is near the CMB, the whole layer remains near the CMB, like the "continuous layer" category. In the intermediate range of HNB, three typical states exist, which will be described below.

The first category is the "mushroom-shaped plume" (Figure 6-4C). In this category, the HNB is significantly higher than the initial thickness of the chemical layer *d*, and $\Delta\rho_{CMB}$ is small, typically less than 0.8%. Several thermo-chemical plumes form with δT usually less than 0.6. Unlike the classical thermo-chemical plumes, the bulk of the mushroom-shaped plumes never reach to the top of the domain. The plume head of a mushroom-shaped plume entrains cold material during its ascent. Subsequently, some of the cold material in the plume head starts to descend in the mid mantle, forming dripping side lobes. Simultaneously, the plume conduit continues to bring warm material into the rising plume conduit. All of the anomalous material is entrained in the plumes. Although a small amount of anomalous material with exceptionally high temperature reaches the top boundary, most of the anomalous material reaches the mid-mantle. The dripping side lobes and rising conduit together have a mushroom shape. This category is labeled “M” in Figure 6-3. This category occurs at the combination of small $\Delta\rho_{top}$ and large K_{S2}.

The second category is the “dome” (Figure 6-4D). In this category, the HNB is higher than d, and $\Delta\rho_{CMB}$ is between 0.8% to 1.2%. Small-scale convection first develops within the chemical layer, but eventually several small convection cells coalesce into a few large cells. The coalesced convection cells are well-separated from each other. The size of the convection cells continues growing until they reach the HNB, where the positive density anomaly caps their tops. The domes are rounded or flat-topped with very steep sidewalls. The bulk of the anomalous material remains confined to the domes. The thermal plumes, developed on the top of the domes, entrain only a small fraction of the anomalous material. δT of the dome is about 0.7, agreeing with the temperature upon which the HNB was estimated in Figure 6-3. This category is labeled with circles (○) in Figure 6-3. This category occurs at intermediate $\Delta\rho_{top}$ and prefers larger m_α.

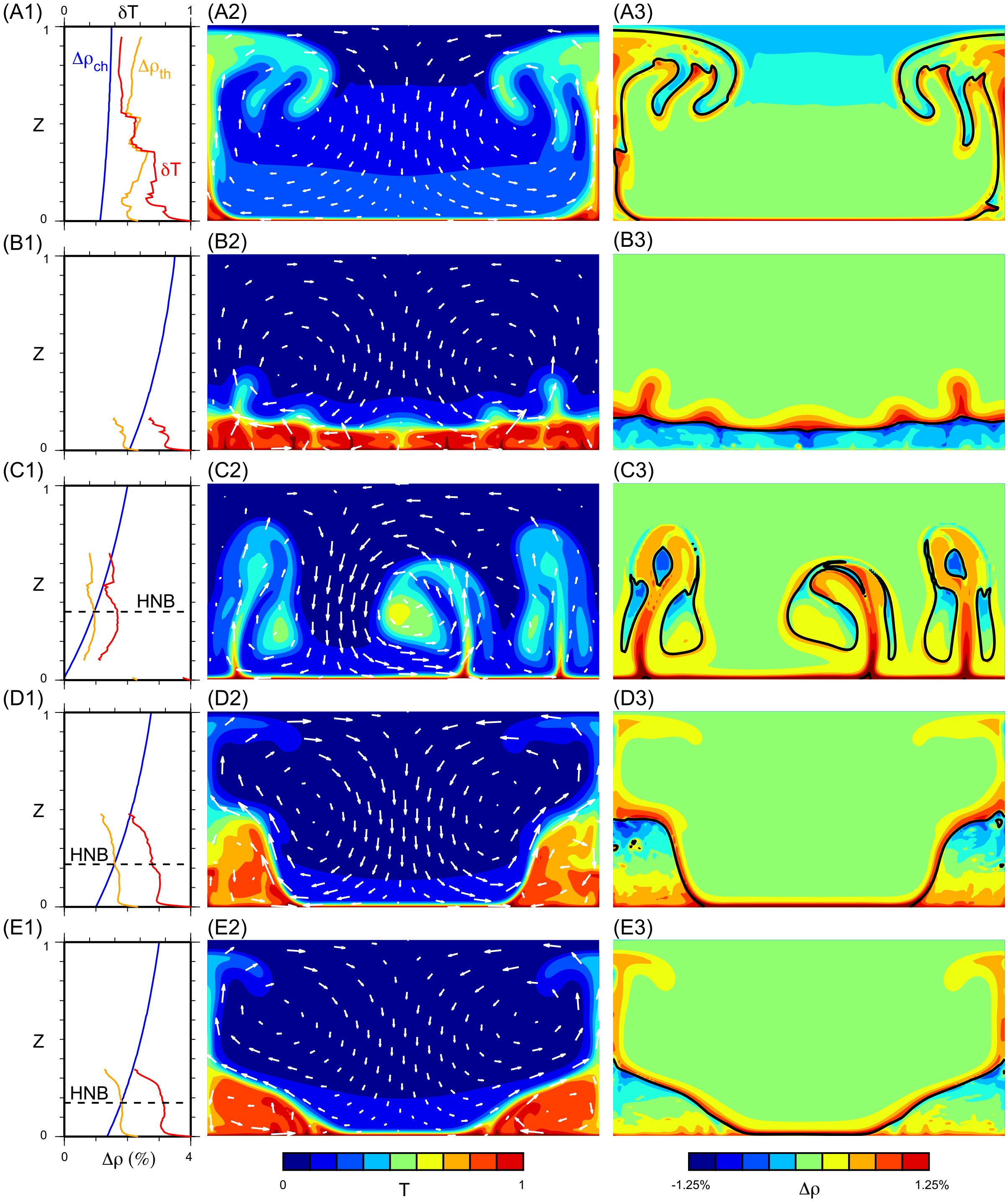

Figure 6-4. Results of various models. The left column shows the profiles of $\Delta\rho_{ch}$, $\Delta\rho_{th}$, and δT. The central column shows the temperature and velocity field. The right column shows the density and composition field. The black line is the contour of C=0.5. (A1–3) Classical thermo-chemical plume. K_{S2}=1.02. $\Delta\rho_{top}$=1.5%. m_α=0.7. (B1–3) Continuous layer. K_{S2}=1.06. $\Delta\rho_{top}$=3.5%. m_α=0.1. (C1–3) Mushroom-shaped plume. K_{S2}=1.06. $\Delta\rho_{top}$=2%. m_α=0.1. (D1–3) Dome. K_{S2}=1.06. $\Delta\rho_{top}$=2.75%. m_α=0.1. t=0.456498E-02 (E1–3) Ridge. K_{S2}=1.06. $\Delta\rho_{top}$=3%. m_α=0.1.

The third category is the “ridge” (Figure 6-4E). The HNB is lower than but close to d, and $\Delta\rho_{CMB}$ is between1.2% to 1.8%. The evolution is similar to the “dome” category above. However, the structure is like a triangular ridge, with gentle-sloping sidewalls. The temperature of the ridges is uniform with δT greater than 0.7. This category is labeled with triangles (Δ) in Figure 6-3. This category occurs at intermediate $\Delta\rho_{top}$ and prefers smaller m_{α}.

The distinction between these three later categories deserves detailed analysis. When the HNB is significantly higher than d, model outcomes will fall in either the mushroom or the dome category, depending on the magnitude of $\Delta\rho_{CMB}$. If $\Delta\rho_{CMB}$ is less than 0.8%, a small temperature increase is sufficient to destabilize the layer. Short-wavelength instability within the chemical layer grows quickly and detaches from the bottom, forming several small plumes with small δT. On the other hand, if $\Delta\rho_{CMB}$ is greater than 0.8%, a large temperature increase is required to destabilize the layer. Instabilities at short wavelengths within the chemical layer merge, forming long wavelength structures, so that the layer further accumulates heat. This leads to larger domes compared to detached mushroom-shaped plumes.

When the HNB is comparable to d, the chemical structure of the model outcome will be either a dome or a ridge. If $\Delta\rho_{CMB}$ is less than 1.2%, the base of the structure is buoyant. Strong active upwellings inside the structure rise along the sidewalls. The buoyancy of the upwellings maintains the steep sidewalls, forming a dome. On the other hand, if $\Delta\rho_{CMB}$ is greater than 1.2%, $\Delta\rho_{ch}$ is close to $\Delta\rho_{th}$. The net density anomaly is small, and the buoyancy force is less important in controlling the shape of the structure. Instead, the shape of the structure is controlled by the viscous stress of the background flow. The background flow near the CMB pushes the structure into a triangular ridge. The magnitude of density heterogeneity inside a ridge is significantly less than that inside a dome.

6.3.4 Remarks

The division between the five categories is gradual and not sharp. A chemical structure can exhibit morphology akin to two categories. For a model at the transition between the classical thermo-chemical plume and the mushroom-shaped plume, part of the plume head forms dripping side lobes that fall, while the other part of the plume head impinges the top boundary. For a model at the transition between the mushroom-shaped plume and the dome, the dripping side lobes of various plumes are swept by the background flow and merge, forming a large dome (Figure 6-5A). For a model at the transition between the dome and ridge, its shape is between that of a triangular ridge and a rounded dome. For a model at the transition between the ridge and the continuous layer, the bases of the ridges interconnect. These transitional models are labeled in double symbols in Figure 6-3.

We must emphasize the importance of presenting the density field for discerning the dynamics of thermo-chemical convection. Chemical structures with different evolutionary pathways can exhibit similar morphologies at a single time; temperature alone cannot predict subsequent evolution. Such ambiguity is removed by showing the density field, which directly relates to the driving force of convection. For example, a classical thermo-chemical plume at its early stage can resemble a dome in morphology (Figure 6-5B), but the density field clearly reveals its buoyant nature.

The five categories cover most model outcomes. However, there were a few models that did not fit within the five categories. One example is the “hourglass-shaped plume” (Figure

6-5C). The profiles of $\Delta\rho_{th}$ and $\Delta\rho_{ch}$ intersect at the mid-mantle. Below the intersection point, $\Delta\rho_{ch}$ dominates over $\Delta\rho_{th}$, and the anomalous material is stable. But occasionally parcels of anomalous material can rise above the intersection point, where $\Delta\rho_{th}$ dominates. The parcel will rise to the top of the computational domain as a plume. The base of the anomalous material remains at the bottom. The shape of the detached plume and remaining base is similar in appearance to an hourglass, with a narrow "neck" in the mid-mantle, similar to the structure in Figure 6-1A. Another example is the "columnar plume" (Figure 6-5D). The profiles of $\Delta\rho_{th}$ and $\Delta\rho_{ch}$ are sub-parallel. The anomalous material accumulates into a pile and coherently rises as a column slowly. There might be an HNB, but the dense material above the HNB could not stabilize the column. The column can reach the top of the convection box. Unlike a classical thermo-chemical plume, a columnar plume has a broad plume conduit and no plume head.

The occurrences of hourglass-shaped and columnar plumes are rare and isolated in the parameter space. Of the 130 cases explored, only one hourglass-shaped and three columnar plumes were found. *Farnetani and Samuel* [2005] found similar types of plumes, but they did not mention how frequently these structures occurred. Due to their restricted range in the parameter space, the significance of hourglass-shaped and columnar plumes in the context of the Earth's mantle is questionable. In contrast, each of the five categories (classical thermo-chemical plumes, mushroom-shaped plumes, domes, ridges, and continuous layers) spans a well-defined and significant range in the parameter space. As a result, we will concentrate our attention on these five categories in the Discussion section.

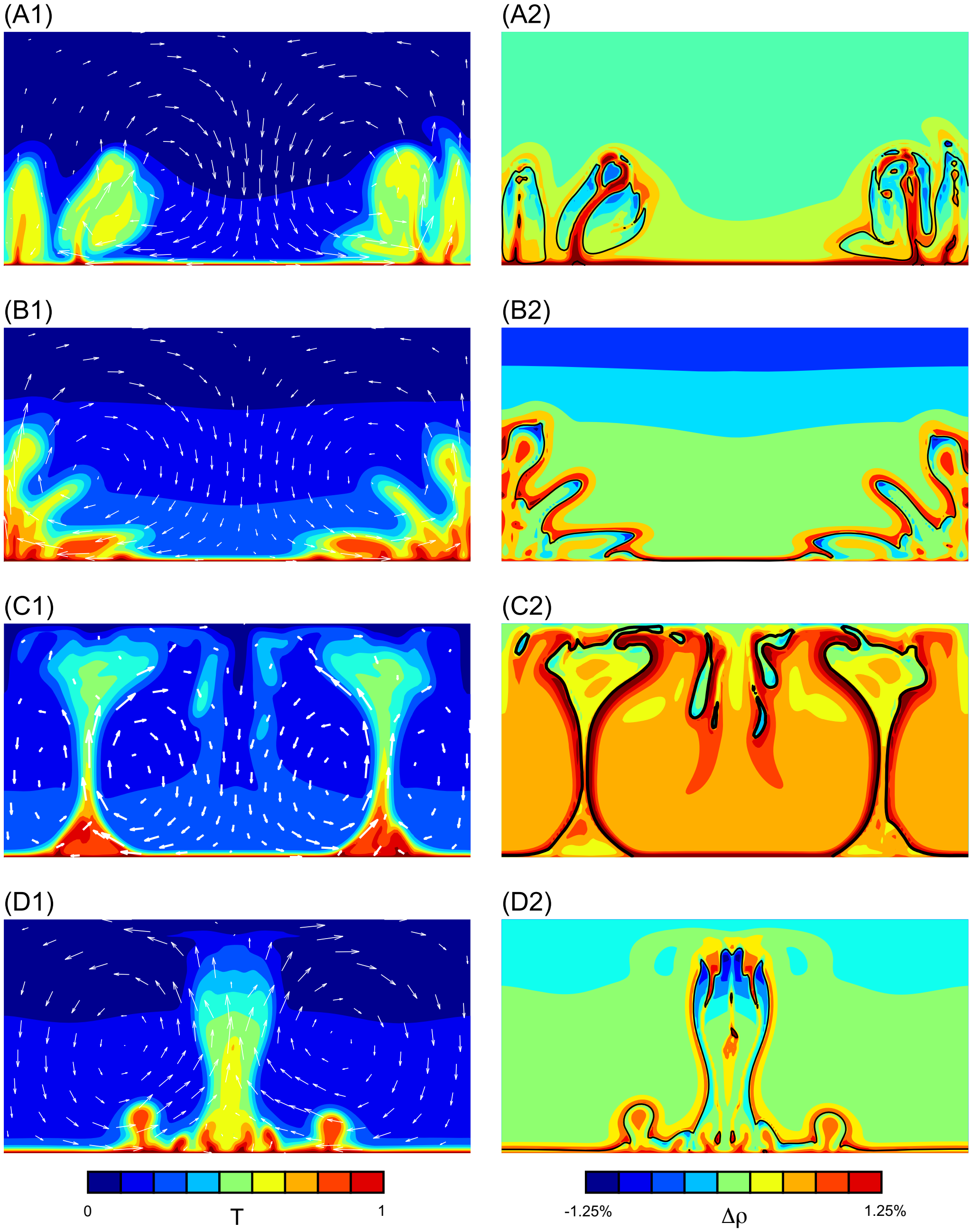

Figure 6-5. Additional model outcomes. (A) Mushroom-shaped plumes swept into piles. K_{S2}=1.08. $\Delta\rho_{top}$=3%. m_{α}=0.2 (B) Early stage of a classical thermo-chemical plume. K_{S2}=1.02. $\Delta\rho_{top}$=1.5%. m_{α}=0.7. (C) Hourglass-shaped plume. K_{S2}=1.02. $\Delta\rho_{top}$=1.75%. m_{α}=0.7. (D) Columnar plume. K_{S2}=1.02. $\Delta\rho_{top}$=1.5%. m_{α}=0.5.

Regarding stability, the chemical layers in the classical thermo-chemical and mushroom-shaped plume categories are unstable, and the bulk of the layer is lifted off the CMB in a few overturn cycles. The chemical layer in the continuous layer category is stable, as the layer will stay at the CMB indefinitely. The dome and ridge are neither stable (as their topography is maintained by the excess temperature and will collapse without heating across the CMB) nor unstable (as the structures are never removed from the CMB). Hence, the dome and ridge are metastable.

6.4 Discussion

We have explored a wide range of parameters for compressible thermo-chemical convection. Now we will apply these results to the Earth's mantle. α_m for the lower mantle material is likely not large, suggesting that an HNB could exist for a wide range of K_{S2} and $\Delta\rho_{top}$. If materials with different K_{S2} and $\Delta\rho_{top}$ exist in the lower mantle, what kind of structures will they form?

6.4.1 Possible chemical structures

Anomalous material with small $\Delta\rho_{top}$ is unstable and will erupt as classical thermo-chemical plumes or as mushroom-shaped plumes. In both scenarios, the material will mix with the ambient mantle rapidly. The anomalous material is not expected to remain and accumulate at the CMB. As a result, this type of material is not likely to form large-scale structures within the present-day lower mantle. Nevertheless, it is possible for the material to form large-scale structures beneath cold slabs. If the material could somehow accumulate beneath slabs, the dense and highly viscous slabs will inhibit the boundary layer instability, and a large volume of the anomalous material could accumulate, similar to the results of purely thermal convection models [*Tan et al.*, 2002].

Anomalous material with large $\Delta\rho_{top}$ will form a continuous layer at the base of the mantle. Since such a layer has not been found seismologically, this scenario can be ignored. However, subducted slabs can impinge and deflect the layer, such that the layer becomes isolated piles [e.g., *McNamara and Zhong*, 2005]. Such "piles" are passive structures, as the high topography of the sidewalls is maintained by slab push. The piles are denser than the ambient mantle but less dense than surrounding slabs. This pattern of density variation will be an important diagnostic in later discussion.

Anomalous material with moderate $\Delta\rho_{top}$ will form domes or ridges. Such structures are metastable and can remain at the CMB for long periods of geological time. If this type of material exists in a large quantity, we would expect to find domes and ridges in the lower mantle. There is no definitive seismic evidence of ridges, although the part of the African superplume under the Atlantic mid-ocean ridge is a possible candidate. On the other hand, the shape of the dome resembles the shape of the southern part of the African superplume, a broad structure with steep sidewalls and high relief [*Ni and Helmberger*, 2003a; 2003b; 2003c]. Before we can attribute the dome as the dynamic explanation of the southern African superplume, we must address the problem of uniqueness.

6.4.2 Possible dynamical scenarios for superplumes

Several dynamical scenarios have been proposed for superplumes (Figure 6-6), including: A) buoyant active upwellings [*Forte and Mitrovica*, 2001; *Ni et al.*, 2002], B) plume clusters [*Schubert et al.*, 2004], C) ridges [*Jellinek and Manga*, 2002; *Tackley*, 2002], D) passive piles [*Kellogg et al.*, 1999; *McNamara and Zhong*, 2005], E) sluggish domes [*Davaille*, 1999; *McNamara and Zhong*, 2004], and F) metastable domes [*Tan and Gurnis*, 2005]. We will

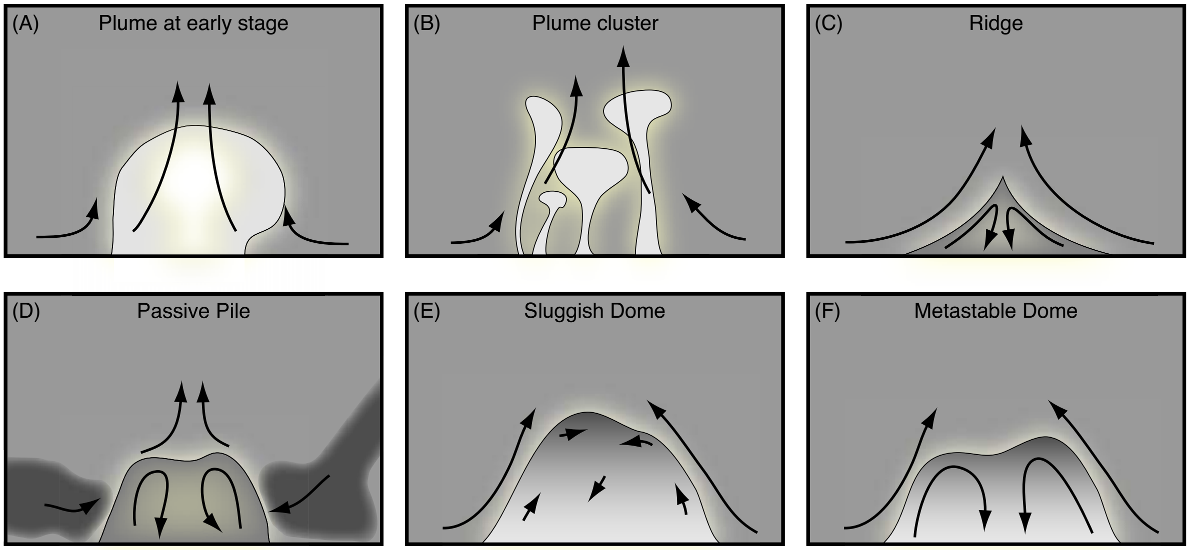

Figure 6-6. Various dynamic scenarios for superplumes. The gray scale indicates the density anomaly. Darker is denser. The arrows indicate the direction and speed of the flow.

introduce each scenario briefly. Scenario A is similar to the early stage of our classical thermo-chemical plume model (Figure 6-5B), where a large, buoyant plum rises to the surface. Scenario B is similar to our model of mushroom-shaped plumes swept together (Figure 6-5A), where several small plumes are swept together by background flow. Scenario C and E are described in previously (Figure 6-4E and 6-4D). Scenario D is also discussed previously, where a continuous chemical layer is impinged and pushed aside by subducted slabs and becomes an isolated pile. Such piles are passive structures. In Scenario E, the dome is more viscous than surrounding mantle and can rise and fall for several overturns. Due to its high viscosity, the particle velocity inside the dome is sluggish. This scenario will be explored more in Chapter 7.

In Scenario C, the triangular shape of the ridge is distinctive from dome-like structures in other scenarios. A ridge-like structure, when filted to the resolution of tomography models, is undistinguishable from a dome-like structure [*Tackley*, 2002]. However, the morphology of the southern African superplume is constrained by body wave seismology, which locally has higher resolution than tomography. The seismic observations clearly require a steep sidewall for the southern African superplume. Therefore, we reject this scenario for the superplume.

In Scenario D, the passive pile is surrounded by subducted slabs. As discussed earlier, the piles are denser than ambient mantle but less dense than surrounding slabs. As a result, the pile will look like a low-density anomaly if the horizontal average of density is removed. This is incompatible with results of normal mode inversion [*Ishii and Tromp*, 1999; *Resovsky and Trampert*, 2003; *Ishii and Tromp*, 2004]. Therefore, this scenario is also rejected.

In the remaining four scenarios, the outline of the chemical structures all have a similar dome shape. With morphology alone, we cannot determine which scenario would represent the southern African superplume best. Fortunately, the southern African superplume has a distinctive seismic velocity anomaly. The southern African superplume has average $\delta V_P=-0.5\%$ and $\delta V_S=-3\%$. Can these dynamic scenarios fit the seismic observation and, if so, what thermo-elastic parameters are required?

6.4.3 Conversion to seismic anomalies

We transform dynamic model results into seismic velocity anomalies δV_P and δV_S as follows. We assume that the ratio of shear modulus G to bulk modulus K_S, $R_1=G/K_S$, is fixed at 0.45, similar to PREM at 2700 km depth. The value of R_1 does not strongly affect later

Table 6-4. Estimate on elastic moduli perturbation.

$\delta\rho$	-1%	0%	1%
δK_S	1%	2%	3%
δG	-7%	-6%	-5%

analysis. The perturbations to V_P and V_S can be written as

$$\begin{aligned}\delta V_P &= \frac{1}{2}\left(\delta(K_S+\frac{4}{3}G)-\delta\rho\right)=\frac{1}{2}\left(\frac{\Delta K_S+4\Delta G/3}{K_S+4G/3}-\delta\rho\right)\\ &=\frac{1}{2}\left(\frac{\Delta K_S}{(1+4R_1/3)K_S}+\frac{4R_1\Delta G/3}{(1+4R_1/3)G}-\delta\rho\right)=\frac{1}{2}\left(\frac{\delta K_S+4R_1\delta G/3}{1+4R_1/3}-\delta\rho\right)\end{aligned} \quad (6\text{-}27)$$

$$\delta V_S=\frac{1}{2}\left(\delta G-\delta\rho\right) \quad (6\text{-}28)$$

where ΔK_S and ΔG are the changes in the bulk and shear moduli; $\delta\rho$, δK_S and δG are the perturbations to the density, bulk modulus, and shear modulus, respectively. $\delta\rho$ can be directly retrieved from dynamic models. In average, $\delta\rho$ is in the ranges of -1% to 1%. A simple calculation indicates the required elastic modulus perturbations (Table 6-4). It is clear that positive δK_S (i.e., $K_{S2}>1$) is required by the seismic data.

The perturbations to the elastic moduli are decomposed into compositional and thermal parts. Assuming these two parts are linearly independent, we can write

$$\delta K_S=\frac{\partial\ln K_S}{\partial C}\mathrm{C}+\frac{\partial\ln K_S}{\partial T}\mathrm{T} \quad (6\text{-}29)$$

$$\delta G=\frac{\partial\ln G}{\partial C}\mathrm{C}+\frac{\partial\ln G}{\partial T}\mathrm{T} \quad (6\text{-}30)$$

There are four parameters for the composition and temperature derivatives of the elastic moduli. Most of the temperature variation occurs inside material 2. Therefore, the temperature derivatives of the elastic moduli of material 1 are unimportant, with the exception in the thermal boundary layer. We will assume that the two materials have the same temperature derivatives of the elastic moduli. The composition derivative of K_S is known.

$$\frac{\partial \ln K_S}{\partial C} = \frac{K_{S2} - K_{S1}}{K_{S1}} = K_{S2} - 1 \tag{6-31}$$

Furthermore, we assume that the ratio of temperature derivatives of the elastic moduli is constant.

$$\frac{\partial \ln G}{\partial T} \bigg/ \frac{\partial \ln K_S}{\partial T} = R_2 \tag{6-32}$$

R_2 is usually set as 2.6, similar to $MgSiO_3$ perovskite at 2000 km depth between 1500 K and 3500 K [*Oganov et al.*, 2001], but sometimes as 2.2 or 3.0.

As a result, two unknown parameters ($\partial \ln G/\partial C$ and $\partial \ln K_S/\partial T$) can be chosen to satisfy the two constraints (average δV_P and δV_S). For any given $\partial \ln K_S/\partial C$ and $\delta\rho$, without knowledge of T, we can find a unique set of $T\partial \ln K_S/\partial T$, $T\partial \ln G/\partial T$ and $\partial \ln G/\partial C$ that fit the observed average δV_P and δV_S values (Table 6-5).

In our dynamic models, T of the anomalous material (i.e. δT) is usually between 0.6 to 0.8, from which we can estimate $\partial \ln K_S/\partial T$ and $\partial \ln G/\partial T$. For reference, the dimensional values of $\partial \ln K_S/\partial T$ and $\partial \ln G/\partial T$ for $MgSiO_3$ perovskite are -3.29×10^{-5} K^{-1} and -8.62×10^{-5} K^{-1}, respectively [*Oganov et al.*, 2001]. These values can be non-dimensionalized by multiplying ΔT_{total}. The temperature contrast ΔT_{total} across the lower mantle is estimated in the range of 1800 to 2400 K [*Boehler*, 2000] and is 1800 K in our dynamic models. After non-dimensionalization, for $MgSiO_3$ perovskite, $T\partial \ln K_S/\partial T$ is between -3.5 to -6.3%, and $T\partial \ln G/\partial T$ is between -9.3% to -16.6%. This estimate has large uncertainty and only

Table 6-5. Estimate on temperature and composition derivatives of elastic moduli.

K_{S2}		**1.02**			**1.04**			**1.06**			**1.08**		
average $\delta\rho$ (%)		**-1**	**0**	**1**	**-1**	**0**	**1**	**-1**	**0**	**1**	**-1**	**0**	**1**
$T\partial\ln K_S/\partial T$ (%)		-1	0	1	-3	-2	-1	-5	-4	-3	-7	-6	-5
R_2=2.2	**$T\partial\ln G/\partial T$ (%)**	-2.2	0	2.2	-6.6	-4.4	-2.2	-11	-8.8	-6.6	-15.4	-13.2	-11
	$\partial\ln G/\partial C$ (%)	-4.8	-6	-7.2	-0.4	-1.6	-2.8	4	2.8	1.6	8.4	7.2	6
R_2=2.6	**$T\partial\ln G/\partial T$ (%)**	-2.6	0	2.6	-7.8	-5.2	-2.6	-13	-10.4	-7.8	-18.2	-15.6	-13
	$\partial\ln G/\partial C$ (%)	-4.4	-6	-7.6	0.8	-0.8	-2.4	6	4.4	2.8	11.2	9.6	8
R_2=3.0	**$T\partial\ln G/\partial T$ (%)**	-3	0	3	-9	-6	-3	-15	-12	-9	-21	-18	-15
	$\partial\ln G/\partial C$ (%)	-4	-6	-8	2	0	-2	8	6	4	14	12	10

applicable to $MgSiO_3$ perovskite. Nevertheless, it represents a useful reference for plausible lower mantle materials.

From Table 6-5, the case of K_{S2}=1.02 and the case of K_{S2}=1.04 with $\delta\rho>0$ require a set of $T\partial\ln K_S/\partial T$ and $T\partial\ln G/\partial T$ whose magnitude is far smaller than that of plausible mantle material. On the other hand, for the case of $K_{S2}=1.08$, extremely negative $\partial\ln K_S/\partial T$ and $\partial\ln G/\partial T$ would produce excessively negative δV_S (<-6%) in the thermal boundary layer that is incompatible with observations. The excessively negative δV_S can be remedied if we allow $\partial\ln K_S/\partial T$ and $\partial\ln G/\partial T$ of material 1 to be less negative than material 2, which is certainly possible. In addition to satisfying average δV_P and δV_S, each of the converted seismic models has additional distinct features contained within the lateral δV_P and δV_S variations, which can also be compared with seismic observation.

Models of classical thermo-chemical plumes typically occur at small K_{S2} and $\Delta\rho_{top}$. The plume before eruption resembles a dome (Scenario A). The high temperature and low density of the "dome" makes it difficult to fit the observed average δV_P and δV_S. To fit δV_P, a small negative $\partial\ln K_S/\partial T$ is required, which in turn implies a small negative $\partial\ln G/\partial T$. As argued above, the small magnitude of $\partial\ln K_S/\partial T$ and $\partial\ln G/\partial T$ does not match the thermo-elastic property of plausible lower mantle material. We conclude that this scenario is unfavorable. There are a few models of large K_S and m_α that produce classical thermo-chemical plumes (Figure 6-3). The early evolution of these models is similar to the evolution of models of mushroom-shaped plume swept together. The seismic signature of these models is discussed below.

For models of mushroom-shaped plumes swept together (Scenario B), the vertical layering produces strong lateral variations (Figure 6-7A). The plume conduits, made of ambient material, have low δV_S. The dripping side lobes, made of anomalous material, have moderately low δV_S. Such vertical layering should be easily visible by seismic waves traveling vertically through the structure, like SKS or PKP. The southern African superplume is well-sampled by SKS. But no internal vertical layering is found [*Ni and Helmberger*, 2003a]. Therefore, we reject this scenario as an explanation of the superplume.

The scenario of sluggish dome is explored in Chapter 7. The sluggish motion inside the dome allows effective cooling. As a result, the base of the dome is warmer and less dense than the crest. The strong temperature and density gradients consequently produce strong vertical gradients in δV_S and δV_P. However, the δV_S and δV_P of the southern African superplume appears to be vertically uniform. Also in Chapter 7, we argue that the physical mechanisms for sluggish domes, including composition-dependent rheology, temperature-dependent rheology with negative activation enthalpy, and radiative heat transfer, have not been demonstrated for lower mantle conditions. Therefore, we reject the scenario.

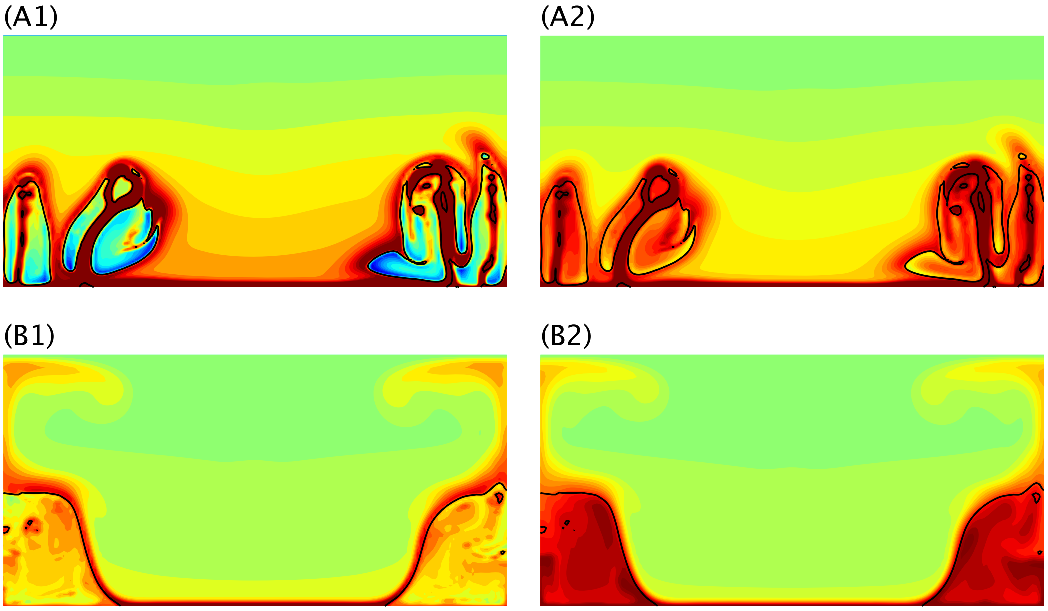

Figure 6-7. Predicted seismic anomalies. δV_P is displayed on the left column (-1.5% to 1.5%), and δV_S on the right (-4% to 4%). (A) converted from Figure 6-5A, using R_2=2.6, $\partial \ln K_S/\partial T$=-8% and $\partial \ln G/\partial C$=7%. (B) converted from Figure 6-4D, using R_2=2.6, $\partial \ln K_S/\partial T$=-6% and $\partial \ln G/\partial C$=4.4%.

For models of metastable domes, the thermal boundary layer outside the chemical boundary produces a δV_P minimum. In contrast, δV_S smoothly decreases across the thermal boundary layer and has a local minimum at the inner edge of the chemical boundary (Figure 6-7B). The minimum of δV_S and δV_P is offset in a horizontal profile. Such an offset is found in all models of metastable domes. The converted seismic model fits the observation surprisingly well. The converted seismic model fits not only the average δV_S and δV_P, but also travel times versus epicenter distance for S, S_{diff}, S_CS, SKS, P, P_{diff}, P_CP, and PKP phases [*Sun et al.*, 2006]. The δV_S and δV_P minimums on the edge, predicted by the dynamic models, is observed at the northern edge of the Pacific superplume [*Sun et al.*, 2006]. The data are also consistent with the offset in the minimum of δV_S and δV_P, although not conclusively. Furthermore, the thermo-elastic parameters required by the fit are close to the parameters of $MgSiO_3$ perovskite [*Oganov et al.*, 2001]. Therefore, the metastable dome scenario is favored as an explanation of the southern African superplume. Finally, the density structure, close to neutrally buoyancy predicted by the model, is compatible with dynamic flow models that simultaneously match observed topography and uplift rate of the African superplume [*Gurnis et al.*, 2000].

Because of entrainment, the chemical structure will gradually lose its density contrast and adjust its morphology accordingly. For example, a continuous layer can evolve into a ridge, and then to a metastable dome over geological time scales. As a result, a continuum of morphologies is expected in the mantle [*Davaille et al.*, 2005]. We suspect that the mid-Atlantic African superplume is an elongated ridge structure. As its density decreases by entrainment, the superplume becomes a metastable dome structure in the southern part. Our interpretation is similar to that of *Davaille et al.* [2005], except that they invoke a highly viscous layer (sluggish dome) to explain the dome-like structures.

6.4.4 Implication to geochemistry and mineralogy

Hotspot volcanism is common above mantle superplumes. If mantle plumes originate from the superplumes, they must carry entrained superplume material. Superplumes can be the source reservoir of the DUPAL anomaly [*Castillo*, 1988], and thermal plumes rising on top of the superplumes can slowly entrain the anomalous material. The DUPAL anomaly has high Pb^{207}/Pb^{204}, Pb^{208}/Pb^{204}, and Sr^{87}/Sr^{86} ratios, indicating the source reservoir is enriched in U, Th and Rb. The isotopic age of the source reservoir of the DUPAL anomaly is estimated to be 1–2 Gyrs [*Hofmann*, 1997]. Only the metastable structures (domes and ridges) and the stable continuous layer can survive for such a long time.

A popular hypothesis for the material of the source reservoir is that it is recycled material that was once fractionated (e.g., oceanic crust or enriched oceanic lithosphere) and later subducted back into the deep mantle [*Hofmann and White*, 1982; *Hirschmann et al.*, 2003]. Pyroxenite is a pyroxene-rich ($MgSiO_3$) rock that lacks sufficient olivine (Mg_2SiO_4) to be considered peridotitic. Pyroxenite is commonly attributed to recycled oceanic crust [*Hauri*, 1996] or enriched oceanic lithosphere [*Hirschmann et al.*, 2003]. In the lower mantle, a pyroxenite will contain more perovskite ($MgSiO_3$) and less magnesiowüstite (MgO) than the peridotitic mantle. Because the perovskite is denser and less compressible than the magnesiowüstite, pyroxenite will be denser and will have a higher bulk modulus than the peridotitic mantle. In fact, pyroxenite has been shown to be 1–2% denser and have a 7% higher bulk modulus than PREM for a 1600 K adiabat [*Lee et al.*, 2005], which is consistent with the material properties of a metastable dome. Fe enrichment might be required to increase the density of pyroxenite to better match the dynamic models. Recent mineralogical inversion of seismic data suggests that the superplumes are enriched in perovskite and Fe [*Trampert et al.*, 2004], which agrees with the pyroxenite model.

The volume of the African superplume has been estimated to be at least 10^{10} km^3 [*Ni and Helmberger*, 2003c]. The volume of the Pacific superplume is possibly smaller, and we assume it is about $5x10^9$ km^3. So, the total volume of the superplumes is about $1.5x10^{10}$ km^3. The average thickness of oceanic crust is 7 km, and the subduction rate of oceanic crust is about 20 km^3/yr. From a simple mass balance calculation, the replenishment time of superplumes by oceanic crust is about 0.75 Gyrs, which is consistent with the longevity of metastable domes in the dynamic model. In the mass balance calculation, we assumed that all subducted oceanic crust goes into superplumes, which is unlikely. Some of the subducted oceanic crust may not segregate from the subducted lithosphere and mix with the mantle [*Christensen and Hofmann*, 1994]. Therefore, the replenish time of 0.75 Gyrs is a lower bound of the age of the superplumes. The actual age can easily be 1 Gyrs or older, which would reconcile with the observed isotopic age.

6.4.5 Future works

In this study, the profile of ρ_r is parameterized by the composition-dependent bulk modulus and hydrostatic compression, and the profile of α is parameterized by a linear equation. The bulk modulus is assumed constant with depth and temperature. This approach does not take the thermodynamics into account. Furthermore, in the conversion to seismic models, we consider the temperature-dependence of the bulk modulus, which is inconsistent with the previous assumption. Such inconsistency is shared among current generation of dynamic models. Ideally, the dynamic model should be complemented by an equation of state from mineral physics. Given the temperature, pressure, and composition fields from dynamic models, the equation of the state can be used to calculate the density and elastic moduli, which can be fed back into dynamic models to drive the convection (density) or to predict the seismic velocity (elastic moduli). Such an approach is desirable in modeling the thermo-chemical evolution of Earth.

References

Akber-Knutson, S., G. Steinle-Neumann, and P. D. Asimow (2005), Effect of Al on the sharpness of the MgSiO3 perovskite to post-perovskite phase transition, *Geophys. Res. Lett.*, *32*, L14303, doi:10.1029/2005GL023192.

Allegre, C. J., O. Brevart, B. Dupre, and J. F. Minster (1980), Isotopic and chemical effects produced in a continuously differentiating convecting earth mantle, *Phil. Trans. R. Soc. A*, *297*, 447–477.

Anderson, O. L. (1967), Equation for thermal expansivity in planetary interiors, *J. Geophys. Res.*, *72*, 3661–3668.

Badro, J., et al. (2004), Electronic transitions in perovskite: Possible nonconvecting layers in the lower mantle, *Science, 305*, 383–386.

Balachandar, S., D. A. Yuen, and D. Reuteler (1992), Time-Dependent 3-Dimensional Compressible Convection with Depth-Dependent Properties, *Geophys. Res. Lett.*, *19*, 2247–2250.

Barrett, R., et al. (1994), *Templates for the Solution of Linear Systems: Building Blocks for Iterative Methods*, 2 ed., 141 pp., SIAM, Philadelphia, PA.

Baumgardner, J. R. (1985), 3-Dimensional Treatment of Convective Flow in the Earths Mantle, *J. Statistical Physics*, *39*, 501.

Bercovici, D., G. Schubert, and G. A. Glatzmaier (1992), 3-Dimensional Convection of an Infinite-Prandtl-Number Compressible Fluid in a Basally Heated Spherical-Shell, *J. Fluid Mech.*, *239*, 683–719.

Boehler, R. (2000), High-pressure expeeriments and the phase diagram of lower mantle and core materials, *Rev. Geophys.*, *38*, 221–245.

Brooks, A. N., and T. J. R. Hughes (1982), Streamline Upwind Petrov-Galerkin Formulations for Convection Dominated Flows with Particular Emphasis on the Incompressible Navier-Stokes Equations, *Comput. Method Appl. M.*, *32*, 199–259.

Brooks, C., S. R. Hart, A. W. Hofmann, and D. E. James (1976), Rb-Sr mantle isochrons from oceanic regions, *Earth Planet. Sci. Lett.*, *32*, 51–61.

Bunge, H. P., M. A. Richards, and J. R. Baumgardner (1997), A sensitivity study of three-dimensional spherical mantle convection at 10(8) Rayleigh number: Effects of depth-dependent viscosity, heating mode, and an endothermic phase change, *J. Geophys. Res.*, *102*, 11991–12007.

Burke, K., and T. H. Torsvik (2004), Derivation of Large Igneous Provinces of the past 200 million years from long-term heterogeneities in the deep mantle, *Earth Planet. Sci. Lett.*, *227*, 531–538.

Caracas, R., and R. E. Cohen (2005), Effect of chemistry on the stability and elasticity of the perovskite and post-perovskite phases in the MgSiO3-FeSiO3-Al2O3 system and implications for the lowermost mantle, *Geophys. Res. Lett.*, *32,* L16310, 10.1029/2005GL023164.

Castillo, P. (1988), The Dupal Anomaly as a Trace of the Upwelling Lower Mantle, *Nature*, *336*, 667–670.

Castle, J. C., and R. D. van der Hilst (2003), Searching for seismic scattering off mantle interfaces between 800 km and 2000 km depth, *J. Geophys. Res.*, *108,* 2095, doi:10.1029/2001JB000286.

Christensen, U. (1984), Instability of a hot boundary-layer and initiation of thermo-chemical plumes, *Ann. Geophys.*, *2*, 311–319.

Christensen, U. R., and A. W. Hofmann (1994), Segregation of subducted oceanic-crust in the convecting mantle, *J. Geophys. Res.*, *99*, 19867–19884.

Davaille, A. (1999), Simultaneous generation of hotspots and superswells by convection in a heterogenous planetary mantle, *Nature*, *402*, 756–760.

Davaille, A., et al. (2005), Convective patterns under the Indo-Atlantic << box >>, *Earth Planet. Sci. Lett.*, *239*, 233–252.

Davies, G. F. (1999), *Dynamic earth: plates, plumes, and mantle convection*, 458 pp., Cambridge University Press, Cambridge.

Davies, G. F., and M. Gurnis (1986), Interaction of Mantle Dregs with Convection - Lateral Heterogeneity at the Core Mantle Boundary, *Geophys. Res. Lett.*, *13,* 1517–1520.

Dziewonski, A. M., and D. L. Anderson (1981), Preliminary reference earth model, *Phys. Earth Planet. Inter.*, *25*, 297–356.

Farnetani, C. G. (1997), Excess temperature of mantle plumes: The role of chemical stratification across D", *Geophys. Res. Lett.*, *24*, 1583–1586.

Farnetani, C. G., and H. Samuel (2005), Beyond the termal plume paradigm, *Geophys. Res. Lett.*, *32,* L07311, doi:10.1029/2005GL022360.

Forte, A. M., and J. X. Mitrovica (2001), Deep-mantle high-viscosity flow and thermochemical structure inferred from seismic and geodynamic data, *Nature*, *410,* 1049–1056.

Garnero, E. J. (2000), Heterogeneity of the lowermost mantle, *Annu. Rev. Earth Planet. Sci.*, *28*, 509–537.

Garnero, E. J., and D. V. Helmberger (1996), Seismic detection of a thin laterally varying boundary layer at the base of the mantle beneath the central-Pacific, *Geophys. Res. Lett.*, *23*, 977–980.

Glatzmaier, G. A. (1988), Numerical Simulations of Mantle Convection - Time-Dependent, 3-Dimensional, Compressible, Spherical-Shell, *Geophys. Astro. Fluid*, *43*, 223.

Gonnermann, H. M., M. Manga, and A. M. Jellinek (2002), Dynamics and longevity of an initially stratified mantle, *Geophys. Res. Lett.*, *29*, 1399, doi:10.1029/2002GL014851.

Grand, S. P., R. D. van der Hilst, and S. Widiyantoro (1997), Global seismic tomography: a snapshot of convection in the Earth, *GSA Today*, *7*, 1–7.

Gurnis, M. (1986), The effects of chemical density differences on convective mixing in the Earth's mantle, *J. Geophys. Res*, *91*, 1407–1419.

Gurnis, M., J. X. Mitrovica, J. Ritsema, and H. van Heijst (2000), Constraining mantle density structure using geological evidence of surface uplift rates: The case of the African Superplume, *Geochem. Geophys. Geosyst.*, *1*, doi:10.1029/1999GC000035.

Hama, J., and K. Suito (2001), Thermoelastic models of minerals and the composition of the Earth's lower mantle, *Phys. Earth Planet. Inter.*, *125*, 147–166.

Hansen, U., and D. A. Yuen (1988), Numerical simulations of thermal-chemical instabilities at the Core Mantle Boundary, *Nature*, *334*, 237–240.

Hauri, E. H. (1996), Major-element variability in the Hawaiian mantle plume, *Nature*, *382*, 415–419.

Helmberger, D., T. Lay, S. Ni, and M. Gurnis (2005), Deep mantle structure and the postperovskite phase transition, *P. Natl. Acad. Sci. USA*, *102*, 17257–17263.

Hirose, K., R. Sinmyo, S. N., and O. Y. (2006), Determination of post-perovskite phase transition boundary in MgSiO3 using Au and MgO internal pressure standards, *Geophys. Res. Lett.*, *33*, L01310, doi:10.1029/2005GL024468.

Hirschmann, M. M., T. Kogiso, M. B. Baker, and E. M. Stolper (2003), Alkalic magmas generated by partial melting of garnet pyroxenite, *Geology*, *31*, 481–484.

Hofmann, A. W. (1997), Geochemistry - Early evolution of continents, *Science*, *275*, 498–499.

Hofmann, A. W., and W. M. White (1982), Mantle plumes from ancient oceanic crust, *Earth Planet. Sci. Lett.*, *57*, 421–436.

Hughes, T. J. R. (2000), *The Finite Element Method: linear static and dynamic finite element analysis*, 682 pp., Dover Pub., Mineola, NY.

Ishii, M., and J. Tromp (2004), Constraining large-scale mantle heterogeneity using mantle and inner-core sensitive normal modes, *Phys. Earth Planet. Inter.*, *146*, 113–124.

Ita, J., and S. D. King (1994), Sensitivity of convection with an endothermic phase-change to the form of governing equations, initial conditions, boundary conditions, and equation of state, *J. Geophys. Res.*, *99*, 15919–15938.

Jacobsen, S. B., and G. J. Wasserburg (1979), The mean age of mantle and crustal reservoirs, *J. Geophys. Res.*, *84,* 7411.

Jarvis, G. T., and D. P. McKenzie (1980), Convection in a Compressible Fluid with Infinite Prandtl Number, *J. Fluid Mech.*, *96*, 515–583.

Jellinek, A. M., and M. Manga (2002), The influence of a chemical boundary layer on the fixity, spacing and lifetime of mantle plumes, *Nature*, *418*, 760–763.

Karato, S., and B. B. Karki (2001), Origin of lateral variation of seismic wave velocities and density in the deep mantle, *J. Geophys. Res.*, *106*, 21771–21783.

Kellogg, L. H., B. H. Hager, and R. D. van der Hilst (1999), Compositional stratification in the deep mantle, *Science*, *283*, 1881–1884.

King, S. D., A. Raefsky, and B. H. Hager (1990), Conman - vectorizing a finite-element code for incompressible 2-dimensional convection in the Earth's mantle, *Phys. Earth Planet. Inter.*, *59*, 195–207.

Kuo, B. Y., E. J. Garnero, and T. Lay (2000), Tomographic inversion of S-SKS times for shear velocity heterogeneity in D ": Degree 12 and hybrid models, *J. Geophys. Res.*, *105*, 28139–28157.

Lay, T., and D. Helmberger (1983), A lower mantle S-wave triplication and the shear velocity structure of D", *Geophys. J. Roy. Astr. S.*, *75*, 799–837.

Lay, T., Q. Williams, and E. J. Garnero (1998), The core-mantle boundary layer and deep Earth dynamics, *Nature*, *392*, 461–468.

Lee, K. K., P. D. Asimow, and O. Tschauner (2005), Phase assemblage and stability of pyroxenite at Lower-Mantle conditions, *Eos Trans. AGU, Jt. Assem. Suppl.*, *86*, Abstract V42A-02.

Leitch, A. M., D. A. Yuen, and G. Sewell (1991), Mantle Convection with Internal Heating and Pressure-Dependent Thermal Expansivity, *Earth Planet. Sci. Lett.*, *102,* 213–232.

Machetel, P., and D. A. Yuen (1989), Penetrative Convective Flows Induced by Internal Heating and Mantle Compressibility, *J. Geophys. Res*, *94,* 10609–10626.

Mao, W. L., et al. (2004), Ferromagnesian postperovskite silicates in the D " layer of the Earth, *P. Natl. Acad. Sci. USA*, *101*, 15867–15869.

Marton, F. C., and R. E. Cohen (2002), Constraints on lower mantle composition from molecular dynamics simulations o MgSiO3 perovskite, *Phys. Earth Planet. Inter.*, *134*, 239–252.

Masters, G., G. Laske, H. Bolton, and A. M. Dziewonski (2000), The relative behavior of shear velocity, bulk sound speed, and compressional velocity in the mantle: implications for chemical and thermal structure, in *Earth's Deep Interior*, edited by S. Karato, et al., pp. 63–87, AGU, Washington DC.

McNamara, A. K., and S. J. Zhong (2004), Thermochemical structures within a spherical mantle: Superplumes or piles?, *J. Geophys. Res.*, *109*, B07402, doi:10.1029/2003JB002847.

McNamara, A. K., and S. J. Zhong (2005), Thermochemical structures beneath Africa and the Pacific Ocean, *Nature*, *437*, 1136–1139.

McNutt, M. K. (1998), Superswells, *Rev. Geophys.*, *36*, 211–244.

Megnin, C., and B. Romanowicz (2000), The three-dimensional shear velocity structure of the mantle from the inversion of body, surface and higher-mode waveforms, *Geophys. J. Int.*, *143*, 709–728.

Montague, N. L., and L. H. Kellogg (2000), Numerical models of a dense layer at the base of the mantle and implications for the geodynamics of D", *J. Geophys. Res.*, *105*, 11101–11114.

Montelli, R., et al. (2004), Finite-frequency tomography reveals a variety of plumes in the mantle, *Science*, *303*, 338–343.

Murakami, M., et al. (2004), Post-perovskite phase transition in MgSiO3, *Science*, *304*, 855–858.

Murakami, M., K. Hirose, N. Sata, and Y. Ohishi (2005), Post-perovskite phase transition and mineral chemistry in the pyrolitic lowermost mantle, *Geophys. Res. Lett.*, *32*, L03304, doi:10.1029/2004GL021956.

Nakagawa, T., and P. J. Tackley (2004), Effects of a perovskite-post perovskite phase change near core-mantle boundary in compressible mantle convection, *Geophys. Res. Lett.*, *31*, L16611, doi:10.1029/2004GL020648.

Nakagawa, T., and P. Tackley (2005), The interaction between the post-perovskite phase change and a thermo-chemical boundary layer near the core-mantle boundary, *Earth Planet. Sci. Lett.*, *238*, 204–216.

Namiki, A. (2003), Can the mantle entrain D"?, *J. Geophys. Res.*, *108*, 2487, doi:10.1029/2002JB002315.

Ni, S., E. Tan, M. Gurnis, and D. Helmberger (2002), Sharp sides to the African superplume, *Science*, *296*, 1850–1852.

Ni, S. D., and D. V. Helmberger (2003a), Seismological constraints on the South African superplume; could be the oldest distinct structure on Earth, *Earth Planet. Sci. Lett.*, *206,* 119–131.

Ni, S. D., and D. V. Helmberger (2003b), Ridge-like lower mantle structure beneath South Africa, *J. Geophys. Res.*, *108*, 2094, doi:10.1029/2001JB001545.

Ni, S. D., and D. V. Helmberger (2003c), Further constraints on the African superplume structure, *Phys. Earth Planet. Inter.*, *140*, 243–251.

Nyblade, A. A., and S. W. Robinson (1994), The African Superswell, *Geophys. Res. Lett.*, *21*, 765–768.

Oganov, A. R., J. P. Brodholt, and G. D. Price (2001), The elastic constants of MgSiO3 perovskite at pressures and temperatures of the Earth's mantle, *Nature*, *411*, 934–937.

Oganov, A. R., and S. Ono (2004), Theoretical and experimental evidence for a post-perovskite phase of MgSiO3 in Earth's D" layer, *Nature*, *430*, 445–448.

Olson, P., and C. Kincaid (1991), Experiments On The Interaction Of Thermal-Convection And Compositional Layering At The Base Of The Mantle, *J. Geophys. Res*, *96*, 4347–4354.

Ono, S., and A. R. Oganov (2005), In situ observations of phase transition between perovskite and CaIrO3-type phase in MgSiO3 and pyrolitic mantle composition, *Earth Planet. Sci. Lett.*, *236*, 914–932.

Quareni, F., W. Marzocchi, and F. Mulargia (1991), Anelastic Convection in the Mantle with Variable Properties, *Phys. Earth Planet. Inter.*, *68*, 117–131.

Ramage, A., and A. I. Wathen (1994), Iterative solution techniques for the Stokes and Navier-Stokes equations, *Int. J. Numer. Methods Fluids*, *19*, 67–83.

Resovsky, J. S., and J. Trampert (2003), Using probabilistic seismic tomography to test mantle velocity-density relationships, *Earth Planet. Sci. Lett.*, *215*, 121–134.

Richards, M. A., and D. C. Engebretson (1992), Large-scale mantle convection and the history of subduction, *Nature*, *355*, 437–440.

Ritsema, J., H. J. van Heijst, and J. H. Woodhouse (1999), Complex shear wave velocity structure imaged beneath Africa and Iceland, *Science*, *286*, 1925–1928.

Rost, S., E. J. Garnero, Q. Williams, and M. Manga (2005), Seismological constraints on a possible plume root at the core-mantle boundary, *Nature*, *435*, 666–669.

Schmeling, H. (1989), Compressible Convection with Constant and Variable Viscosity - the Effect on Slab Formation, Geoid, and Topography, *J. Geophys. Res*, *94*, 12463–12481.

Schubert, G., G. Masters, P. Olson, and P. Tackley (2004), Superplumes or plume clusters?, *Phys. Earth Planet. Inter.*, *146*, 147–162.

Sidorin, I., M. Gurnis, and D. V. Helmberger (1999a), Dynamics of a phase change at the base of the mantle consistent with seismological observations, *J. Geophys. Res.*, *104*, 15005–15023.

Sidorin, I., M. Gurnis, and D. V. Helmberger (1999b), Evidence for a ubiquitous seismic discontinuity at the base of the mantle, *Science*, *286*, 1326–1331.

Solheim, L. P., and W. R. Peltier (1994), Avalanche Effects in-Phase Transition Modulated Thermal-Convection - a Model of Earths Mantle, *J. Geophys. Res.*, *99*, 6997–7018.

Steinbach, V., U. Hansen, and A. Ebel (1989), Compressible Convection in the Earths Mantle - a Comparison of Different Approaches, *Geophys. Res. Lett.*, *16*, 633–636.

Sturhahn, W., J. M. Jackson, and J. F. Lin (2005), The spin state of iron in minerals of Earth's lower mantle, *Geophys. Res. Lett.*, *32*, L12307, doi:10.1029/2005GL022802.

Su, W. J., and A. M. Dziewonski (1997), Simultaneous inversion for 3-D variations in shear and bulk velocity in the mantle, *Phys. Earth Planet. Inter.*, *100*, 135–156.

Sun, D. Y., E. Tan, D. Helmberger, and M. Gurnis (2006), Seismic validation of metastable superplume, in review.

Tackley, P. J. (1996), Effects of strongly variable viscosity on three-dimensional compressible convection in planetary mantles, *J. Geophys. Res.*, *101*, 3311–3332.

Tackley, P. J. (1998), Three-dimensional simulations of mantle convection with a thermo-chemical basal boundary layer: D"?, in *The Core-mantle Boundary Region*, edited by M. Gurnis, et al., pp. 231–253, AGU, Washington DC.

Tackley, P. J. (2002), Strong heterogeneity caused by deep mantle layering, *Geochem. Geophys. Geosyst.*, *3*, 1024, doi:10.1029/2001GC000167.

Tan, E., and M. Gurnis (2005), Metastable superplumes and mantle compressibility, *Geophys. Res. Lett.*, *32*, L20307, doi:10.1029/2005GL024190.

Tan, E., M. Gurnis, and L. J. Han (2002), Slabs in the lower mantle and their modulation of plume formation, *Geochem. Geophys. Geosyst.*, *3*, 1067, doi:10.1029/2001GC000238.

To, A., B. Romanowicz, Y. Capdeville, and N. Takeuchi (2005), 3D effects of sharp boundaries at the borders of the African and Pacific Superplumes: Observation and modeling, *Earth Planet. Sci. Lett.*, *233*, 137–153.

Trampert, J., F. Deschamps, J. Resovsky, and D. Yuen (2004), Probabilistic tomography maps chemical heterogeneities throughout the lower mantle, *Science*, *306*, 853–856.

Tsuchiya, J., T. Tsuchiya, and R. M. Wentzcovitch (2005), Vibrational and thermodynamic properties of MgSiO3 postperovskite, *J. Geophys. Res.*, *110*, B02204, doi:10.1029/2004JB003409.

van der Hilst, R. D., S. Widiyantoro, and E. R. Engdahl (1997), Evidence for deep mantle circulation from global tomography, *Nature*, *386*, 578–584.

van Keken, P. E., et al. (1997), A comparison of methods for the modeling of thermochemical convection, *J. Geophys. Res.*, *102*, 22477–22495.

Wen, L. (2001), Seismic evidence for a rapidly varying compositional anomaly at the base of the Earth's mantle beneath the Indian Ocean, *Earth Planet. Sci. Lett.*, *194,* 83–95.

Wen, L., and D. V. Helmberger (1998), Ultra-low velocity zones near the core-mantle boundary from broadband PKP precursors, *Science*, *279,* 1701–1703.

Williams, Q., and E. J. Garnero (1996), Seismic evidence for partial melt at the base of Earth's mantle, *Science*, *273,* 1528–1530.

Xie, S., and P. J. Tackley (2004), Evolution of helium and argon isotopes in a convecting mantle, *Phys. Earth Planet. Inter., 146,* 417–439.

Zhang, S. X., and D. A. Yuen (1996), Various influences on plumes and dynamics in time-dependent, compressible mantle convection in 3-D spherical shell, *Phys. Earth Planet. Inter.*, *94*, 241–267.

Chapter 7

Competing roles of rheology and thermal expansion in stabilizing a basal chemical layer

Abstract

The stability of a chemical layer at the base of the mantle with composition-dependent rheology and depth-dependent thermal expansion is studied. A high-viscosity chemical layer can form a diapiric plume or a dome by varying the density of the chemical layer and the thermal expansion profile. We demonstrate that the strong temperature gradient inside the chemical layer, caused by composition-dependent rheology, is the dominant factor in stabilizing the chemical layer. Other mechanisms to stabilize the chemical layer are discussed, including temperature-dependent rheology with negative activation enthalpy, radiative heat transfer, and composition-dependent density profile, with the latest mechanism preferred.

7.1 Introduction

The stability of a chemical layer at the base of the mantle has been studied [*Christensen*, 1984; *Gurnis*, 1986; *Hansen and Yuen*, 1988; *Olson and Kincaid*, 1991; *Farnetani*, 1997; *Tackley*, 1998; *Davaille*, 1999; *Montague and Kellogg*, 2000; *Gonnermann et al.*, 2002; *Jellinek and Manga*, 2002; *Ni et al.*, 2002; *Namiki*, 2003; *McNamara and Zhong*, 2004; *Tan and Gurnis*, 2005; *Tan and Gurnis*, 2006]. Of particular interest are the physical parameters that can produce a long-lived chemical layer but with a high relief on its interface [*Ni et al.*, 2002]. Much of the claimed longevity relies on the low entrainment rate observed in the model. The chemical layer in these models tends to form isolated ridges sitting below thermal upwellings [*Jellinek and Manga*, 2002].

Composition-dependent rheology has been shown to change the nature of entrainment and the shape of a dense, basal chemical layer [*Davaille*, 1999; *McNamara and Zhong*, 2004]. When the dense basal layer has a viscosity lower than ambient, the entrainment primarily occurs in thin sheets, while if the material has a high viscosity, the entrainment occurs in thin conduits. Low viscosity layers form ridges with cusps at the interface, with the strongest entrainment occurring at the tips of the cusps. On the other hand, high viscosity layers form domes, which penetrate upward into the less viscous layer but can rise and then sink cyclically for several times. *Davaille* [1999] and *McNamara and Zhong* [2004] argued that the ridges (or cusps) are passive structures, induced by large-scale flow within the ambient layer, while the domes are active structures, controlled by thermal instabilities inside the dense, basal layer. However, both studies give little discussion on how the composition-dependent rheology stabilizes the chemical layer.

Considering a chemical layer with a density (including thermal and chemical contribution) slightly lower than ambient mantle at the base of the mantle. Without composition-dependent rheology, the chemical layer will be less viscous, due to its higher temperature and thermally activated viscosity. When the layer becomes unstable, a plume erupts from the layer. The plume has a lower viscosity than its surroundings and has a large plume head, commonly referred to as a cavity plume [*Whitehead and Luther*, 1975; *Olson and Singer*, 1985; *Campbell and Griffiths*, 1990]. The plume entrains ambient material as it rises, with strongest entrainment in the plume head. In the plume head, the two materials mix together. As a result, the chemical layer is drained by the plumes and mixes with the ambient mantle quickly. On the other hand, if the dense chemical layer has an intrinsic viscosity increase due to its composition, the erupting plume will not have a large head. This type of plume is commonly referred to as the diapiric plume [*Whitehead and Luther*, 1975; *Olson and Singer*, 1985]. The high viscosity of the diapiric plume reduces the particle velocity inside the plume and slows the ascent of the plume. The smaller particle velocity makes entrainment less effective, which keeps the integrity of the plume. The smaller particle velocity also reduces the internal mixing and promotes temperature heterogeneity inside the plume. In addition, the slow ascent of the plume leads to more cooling. As a result, there can be a large temperature gradient with the plume, stabilizing it at the mid-mantle depths (Figure 7-1).

From this argument, we propose that the temperature gradient within the diapiric plume is the dominant factor in stabilizing it. If this is true, we predict that a depth-dependence of thermal expansion could change the stability of the diapiric plume. The coefficient of thermal expansion, α, of the mantle decreases with depth. When a parcel of warm material moves

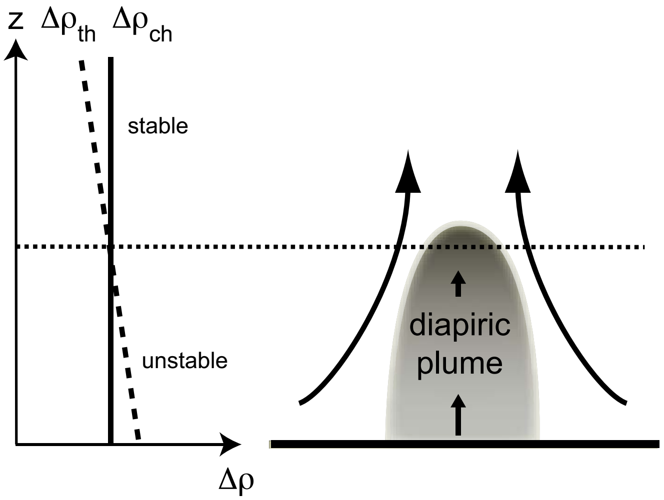

Figure 7-1. Cartoon for a diapiric plume. The plume is highly viscous. The particle velocity (arrows) inside the plume is much smaller than that outside the plume. A large temperature gradient (grayscale) helps to stabilize the plume

upward, its buoyancy increases as α increases. The parcel would lose its heat by thermal diffusion and adiabatic cooling and lose its buoyancy. The adiabatic cooling is proportional to α and the dissipation number (defined in Chapter 6). The dissipation number in the lower mantle is small (about 0.4), and the buoyancy loss due to adiabatic cooling is smaller than the buoyancy gain due to larger α. As a result, we expect that the depth-dependency of thermal expansion will destabilize the diapiric plume.

7.2 Method

The numerical method is described in Chapter 6. We will briefly summarize the model setup. The numerical code is capable of the Truncated Anelastic Liquid Approximation (TALA) [*Ita and King*, 1994], but we only utilize the Extending Boussinesq Approximation (EBA) [*Christensen*, 1995] by setting the Gruneisen parameter (defined in Chapter 6) to infinity, thus removing the adiabatic density gradient. We choose EBA over TALA for two reasons. First, this removes the effect of composition-dependent density profile, which has been shown to strongly control the stability of the chemical layer [*Tan and Gurnis*, 2005; 2006]. Second, we can directly compare these results with *Davaillle* [1999] and *McNamara and Zhong* [2004], which both used Boussinesq Approximation (BA). Compared with the BA, the EBA introduces an adiabatic temperature gradient and adiabatic cooling contributing to increased stability of the chemical layer.

The convection is driven by thermal and chemical density variations. The mantle composition C is modeled using a marker chain method (see Chapter 6). The mantle consists of two types of materials, one is the ambient material (C=0) and the other is the anomalous material (C=1), which is denser than the ambient material by $\Delta\rho_{ch}$. The coefficient of thermal expansion, $\alpha=0.3+m_\alpha z$, varies linearly in z.

The viscosity is temperature and depth dependent according to the equation

$$\eta = e^{\delta_\eta C} \exp\left(\frac{E_\eta + V_\eta (1-z)}{T+T_\eta} - \frac{E_\eta}{T_\eta} \right) \tag{7-33}$$

where δ_η is the viscosity contrast due to composition; E_η is the activation energy; V_η is the activation volume; T is the temperature; and T_η is the temperature offset. The magnitude of this depth-dependence is chosen to compensate for the effect of adiabatic temperature gradients. The viscosity has a minimum cutoff of 10^{-3}. The computational domain is Cartesian and 2x1 with the base corresponding to the CMB. The top of the box, when scaled to Earth, is 2000 km above the CMB. The top and bottom boundaries are free-slip and isothermal, with fixed temperature at 0 and 1, respectively. The sidewalls are reflecting. The initial temperature is adiabatic with a thin, basal thermal boundary layer. The chemical layer is initially flat with a thickness d. The values of all parameters are listed in Table 7-1.

Table 7-1. Values of parameters in models.

Symbol	Description	Value
Ra	Rayleigh number	$2.2\text{x}10^6$
Di	dissipation number	0.4
γ	Gruneisen parameter	Infinity
T_s	surface temperature	0.75
μ	fraction of volume change due to thermal expansion	0.054
δ_η	viscosity contrast due to composition	6.21
E_η	activation energy of viscosity	11
V_η	activation volume of viscosity	-1.8
T_η	temperature offset of viscosity	-1.5
d	initial thickness of the chemical layer	0.125

Each model is run for a non-dimensional time t=0.025 or more, which corresponds to about 5–10 mantle overturns. We calculate the contour C=0.8 and use the maximum height of the contour as the height of the chemical layer. Since the chemical layer is more viscous than the ambient mantle, the entrainment rate is low. The contour approximates the interface of the chemical layer well. We terminate the model early if the chemical layer reaches the top of the domain.

7.3 Results

In the first set of models, we fix m_α=0 and vary $\Delta\rho_{ch}$ to find the transition from a stable to an unstable layer (Figure 7-2A). The transition is sharp and occurs between $\Delta\rho_{ch}$=0.008 to 0.009. The temperature, composition, density, and viscosity fields of two models below and above the transition are shown (Figure 7-2B and 7-2C).

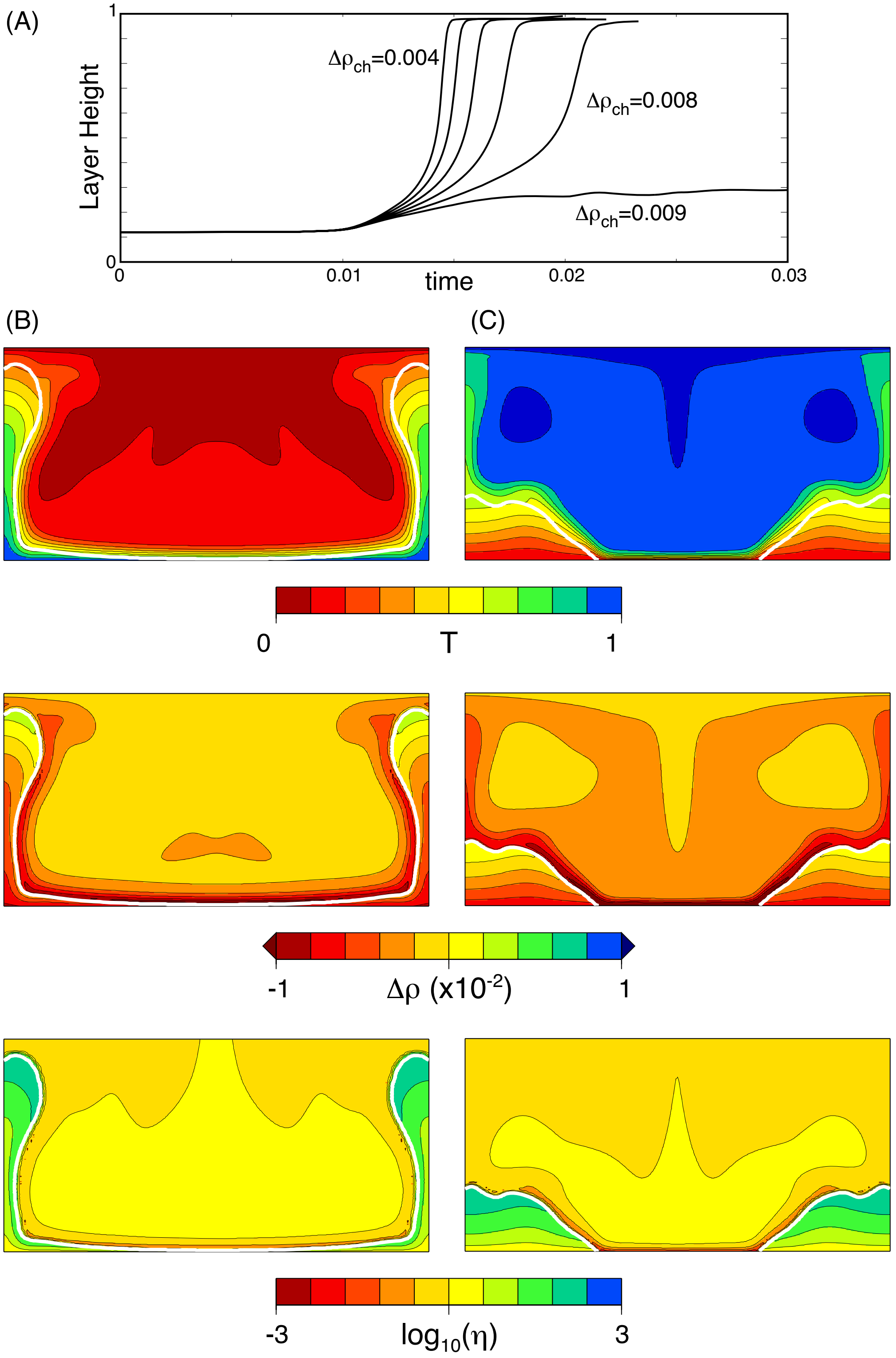

Figure 7-2. Results of m_α=0. (A) The time evolution of the height of the chemical layer. The transition from stable to unstable layer occurs between $\Delta\rho_{ch}$=0.008 to 0.009. (B) The result of $\Delta\rho_{ch}$=0.008. Top: temperature; middle: density; bottom: viscosity. The white lines are the C=0.8 contours. (C) The result of $\Delta\rho_{ch}$=0.009.

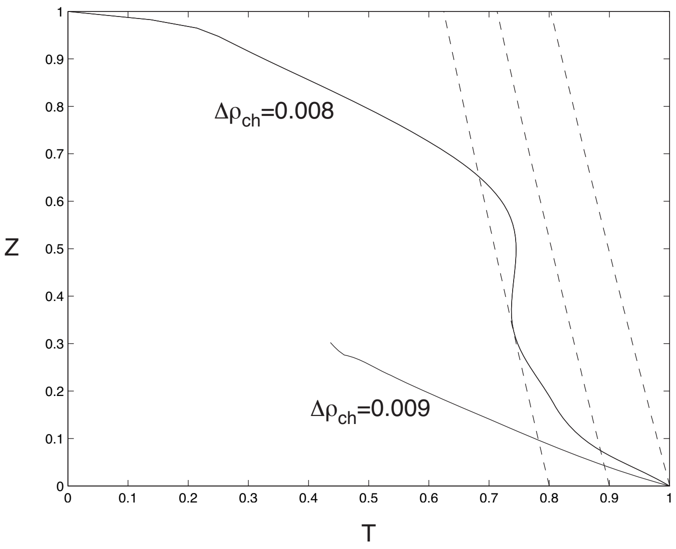

Figure 7-3. Temperature profiles. The solid lines are average temperature profiles of the plume in Figure 7-2B and the dome in Figure 7-2C. The dashed lines are three different adiabatic temperature profiles.

For the unstable layer, owing to its large viscosity, the layer forms a diapir plume, which rises slowly and loses its heat during ascent. As a result, a strong temperature gradient develops inside the diapiric plume (Figure 7-3). Only a small portion of the temperature gradient is attributed to the adiabatic temperature gradient. The entrainment rate in the diapiric plume is low until the plume impinges the top surface. Then, the entrainment rate grows greatly, and the length of the marker chain increases exponentially. The computation is terminated as a result. We suspect that as the diapiric plume is cooled by the top surface, bulk of the anomalous material in the diapiric plume will fall back to the base of the mantle, similar to the results of *Davaille* [1999] and *McNamara and Zhong* [2004].

In the stable regime, the layer forms large domes, with sluggish convection within. To assess the stability of the dome, the calculation continues until *t*=0.034. The height of the

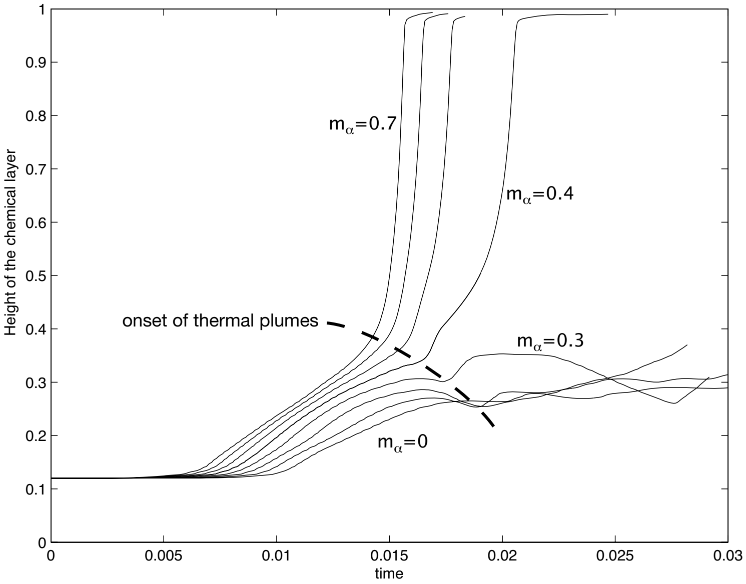

Figure 7-4. Results of $\Delta\rho_{ch}$=0.009. The transition from stable to unstable layer occurs between m_α=0.3 to 0.4. The dashed line marks the onset of thermal plumes.

dome undulates slightly over time, but never rises higher than 0.35. The temperature profile of the dome is nearly conductive with a strong temperature gradient (Figure 7-3).

In the second set of models, we fix $\Delta\rho_{ch}$=0.009 and vary m_α. The increase of thermal expansion in the mid-mantle destabilizes the originally stable layer. Again, we can find a sharp transition from stable to unstable layer between m_α=0.3 to 0.4 (Figure 7-4). For the stable layer, the amplitude of undulation on the height of the dome increases with m_α. For all cases, there is a thermal plume either locates above the dome or leads the chemical diapiric plume. The onset of the thermal plume significantly increases the rising speed of the layer for two reasons. First, the thermal plume establishes a low viscosity conduit, which decreases the resistance of rising chemical layer. Second, after the eruption of the thermal plume, the magnitude of ambient flow increases significantly, which increases the upward drag to the chemical layer.

7.4 Discussion

The results clearly demonstrate the competing roles of depth-dependent thermal expansion versus composition-dependent rheology in the stability of a parcel of warm, rising material. The former will increases the parcel's buoyancy and destabilize it further. The latter will slow down the parcel, so low that cooling by thermal diffusion becomes effective, and stabilize the parcel.

We demonstrate that the strong temperature gradient inside the chemical layer, caused by composition-dependent rheology, is the dominant factor in stabilizing the chemical layer. Since the chemical layer is also hotter than the ambient mantle, the composition field is highly correlated with the temperature field (Figure 7-2). A temperature-dependent rheology law with negative activation enthalpy will have similar effect as the composition-dependent rheology. It has been proposed that a temperature-dependent rheology law with negative activation enthalpy can produce a diapiric plume [*Korenaga*, 2005]. A possible mechanism for the negative activation enthalpy is grain-size sensitive diffusion creep [*Solomatov*, 1996]. But it has not been demonstrated that this mechanism dominate the viscous deformation in the lower mantle condition.

It is conceivable that other physical properties, such as the heat capacity and thermal conductivity, if strongly composition- or temperature-dependent, can potentially induce a strong temperature gradient inside the chemical layer and stabilize it, too. Besides viscosity, the thermal conductivity is the only physical property whose value has been proposed to change over an order of magnitude [*Hofmeister*, 1999; *Badro et al.*, 2004]. The radiative heat conductivity, proportional to the third power of the temperature, can dominate the heat transfer process if the material is transparent to photons. The high to low spin transition of Fe in $(Mg_{0.9},Fe_{0.1})SiO_3$ perovskite increases the transparency in the infrared region [*Badro et al.*, 2004]. It has been shown in a purely thermal convection model that incorporating radiative heat conductivity can stabilize the basal thermal boundary layer [*Matyska and Yuen*, 2005]. Very likely, radiative heat conductivity can stabilize the basal chemical layer too. However, impurity in the perovskite, such as Al and other trace elements, even only a small amount, can absorb the photon and make the perovskite opaque. It is unlikely that the bulk of a mantle rock can be transparent and have high radiative heat conductivity.

In this study, we did not consider the effect of the composition-dependent density profile, which has been shown to profoundly affect the stability of the chemical layer [*Tan and Gurnis*, 2005]. With Earth-like parameters, the composition-dependent density profile can produce a dome-like chemical structure that survives for a geological time scale. Comparing with the models of negative activation enthalpy and radiative heat conductivity, the model of *Tan and Gurnis* [2005] is more plausible and supported by seismic observations.

References

Badro, J., et al. (2004), Electronic transitions in perovskite: Possible nonconvecting layers in the lower mantle, *Science*, *305*, 383–386.

Campbell, I. H., and R. W. Griffiths (1990), Implications of Mantle Plume Structure for the Evolution of Flood Basalts, *Earth Planet. Sci. Lett.*, *99*, 79–93.

Christensen, U. (1984), Instability of a hot boundary-layer and initiation of thermo-chemical plumes, *Ann. Geophys.*, *2*, 311–319.

Christensen, U. (1995), Effects of phase-transitions on mantle convection, *Annu. Rev. Earth Planet. Sci.*, *23*, 65–87.

Davaille, A. (1999), Simultaneous generation of hotspots and superswells by convection in a heterogenous planetary mantle, *Nature*, *402*, 756–760.

Farnetani, C. G. (1997), Excess temperature of mantle plumes: The role of chemical stratification across D", *Geophys. Res. Lett.*, *24*, 1583–1586.

Gonnermann, H. M., M. Manga, and A. M. Jellinek (2002), Dynamics and longevity of an initially stratified mantle, *Geophys. Res. Lett.*, *29*, 1399, doi:10.1029/2002GL014851.

Gurnis, M. (1986), The effects of chemical density differences on convective mixing in the Earth's mantle, *J. Geophys. Res*, *91*, 1407–1419.

Hansen, U., and D. A. Yuen (1988), Numerical simulations of thermal-chemical instabilities at the Core Mantle Boundary, *Nature*, *334*, 237–240.

Hofmeister, A. M. (1999), Mantle values of thermal conductivity and the geotherm from phonon lifetimes, *Science*, *283*, 1699–1706.

Ita, J., and S. D. King (1994), Sensitivity of convection with an endothermic phase-change to the form of governing equations, initial conditions, boundary conditions, and equation of state, *J. Geophys. Res.*, *99*, 15919–15938.

Jellinek, A. M., and M. Manga (2002), The influence of a chemical boundary layer on the fixity, spacing and lifetime of mantle plumes, *Nature*, *418*, 760–763.

Korenaga, J. (2005), Firm mantle plumes and the nature of the core-mantle region, *Earth Planet. Sci. Lett.*, *232*, 29–37.

Matyska, C., and D. A. Yuen (2005), The importance of radioactive heat transfer on superplumes in the lower mantle with the new post-perovskite phase change, *Earth Planet. Sci. Lett.*, *234*, 71–81.

McNamara, A. K., and S. J. Zhong (2004), Thermochemical structures within a spherical mantle: Superplumes or piles?, *J. Geophys. Res.*, *109*, B07402, doi:10.1029/2003JB002847.

Montague, N. L., and L. H. Kellogg (2000), Numerical models of a dense layer at the base of the mantle and implications for the geodynamics of D", *J. Geophys. Res.*, *105*, 11101–11114.

Namiki, A. (2003), Can the mantle entrain D"?, *J. Geophys. Res.*, *108*, 2487, doi:10.1029/2002JB002315.

Ni, S., E. Tan, M. Gurnis, and D. Helmberger (2002), Sharp sides to the African superplume, *Science*, *296*, 1850–1852.

Olson, P., and C. Kincaid (1991), Experiments on the interaction of thermal-convection and compositional layering at the base of the mantle, *J. Geophys. Res*, *96*, 4347–4354.

Olson, P., and H. Singer (1985), Creeping Plumes, *J. Fluid Mech.*, *158*, 511–531.

Solomatov, V. S. (1996), Can hotter mantle have a larger viscosity?, *Geophys. Res. Lett.*, *23*, 937–940.

Tackley, P. J. (1998), Three-dimensional simulations of mantle convection with a thermo-chemical basal boundary layer: D"?, in *The Core-mantle Boundary Region*, edited by M. Gurnis, et al., pp. 231–253, AGU, Washington DC.

Tan, E., and M. Gurnis (2005), Metastable superplumes and mantle compressibility, *Geophys. Res. Lett.*, *32*, L20307, doi:10.1029/2005GL024190.

Tan, E., and M. Gurnis (2006), Compressible thermo-chemical convection and application to lower mantle superplumes, in preparation.

Whitehead, J. A., and D. S. Luther (1975), Dynamics of Laboratory Diapir and Plume Models, *J. Geophys. Res.*, *80*, 705–717.

Appendix A

Benchmarks of regional-regional CitcomS.py coupling

Two regional *CitcomS.py Solvers* are coupled. The size of the embedded domain is half that of the containing domain in each direction (Figure A-1). The two domains share the top surface, and the grids are aligned. This configuration does not incur errors when interpolating exchanged data. Therefore, any discrepancy in the velocity solutions can be attributed the embedded *Solver*. Moreover, when the element number ratio of the containing to the embedded meshes is 2 (case a1 and a5), every embedded node is collocated with another containing node, so that the solutions on the two meshes should be identical. For the other cases, only portions of the embedded nodes are collocated with the containing nodes. The initial temperature field has a hot, spherical anomaly sitting below the embedded domain. Therefore, the initial temperature field in the embedded mesh is 0 everywhere, and the flow inside is purely driven by the BCs. We compare the velocity fields at the 0th time step on the collocated nodes (Table A-1). The purpose of this benchmark is to confirm the consistency of the velocity field on both meshes, which is the basic requirement of solver coupling.

We allow the containing *Solver* to execute for 100 time steps and the embedded *Solver* for corresponding time steps. One-way communication is used, i.e., no temperature feedback from the embedded *Solver* to the containing *Solver*. Discrepancy in temperature fields will

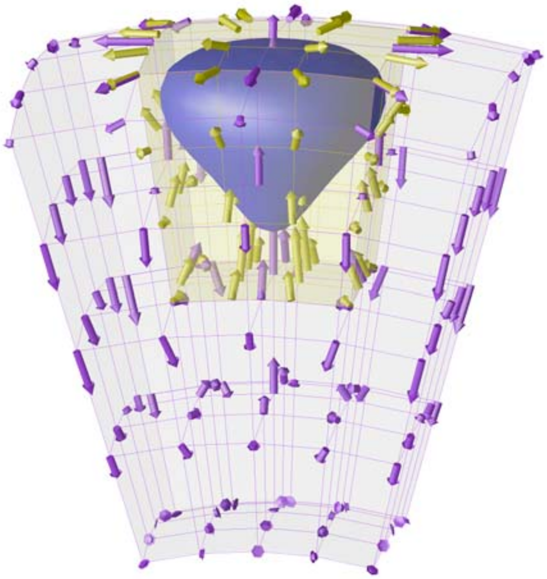

Figure A-1. Regional-regional *CitcomS.py* coupling of case a1 at 100th step. The containing mesh and its velocity vectors are in purple, while the embedded mesh and its velocity vectors in yellow. The magnitude and direction of the velocity fields are consistent for the two meshes. Also plotted are the temperature iso-surfaces (blue for the containing mesh and green for the embedded mesh) at *T=0.05*. The two iso-surfaces are so close that only one is visible. The numbers of grid points are reduced for visualization purpose.

accumulate over time. Then, we compare the temperature fields at the 100th time step on the collocated nodes (Table A-2; Figure A-1). Alternatively, if two-way communication is used instead, the temperature fields of both *Solvers* will be consistent after each synchronized time step. Therefore, the temperature discrepancy of a two-way communication model will be less than 1/100 of the value in Table A-2.

The results in Table A-1 and A-2 confirm that the solution on the embedded mesh is consistent to that on the containing mesh. When all nodes are collocated (case a1 and a5), the discrepancy is minimized. Doubling the resolution of both meshes will decrease the discrepancy by half. Refining the resolution in the embedded mesh while keeping the same

Table A-1. Results of velocity fields at the 0th time step of regional-regional coupling. The second column is the number of elements in each direction of the containing mesh. The third column is the number of elements in each direction of the embedded mesh. **u** is the velocity field in the overlapping region. $\mathbf{d_u}$ is the difference in the velocity fields of the two meshes. RMS is the root mean square. Discrepancy is defined as RMS($\mathbf{d_u}$)/RMS(**u**).

Case	**# of Elements (containing)**	**# of Elements (embedded)**	**RMS(u)**	**RMS(d_u)**	**Discrepancy (%)**
a1	32	16	87.4848	0.374317	0.4279
a2	32	32	87.4848	0.497431	0.5686
a3	32	48	87.4848	0.532460	0.6087
a4	32	64	87.4848	0.935975	1.0698
a5	64	32	84.2790	0.203668	0.2417

Table A-2. Results of temperature fields at 100th time step of regional-regional coupling. We only compare the temperature field in the overlapping region. d_T is the difference in the temperature field of the two meshes. Discrepancy is defined as RMS(d_T)/RMS(T). The fifth column is the time step of the embedded mesh when the time step of the containing mesh is 100.

Case	**# of Elements (containing)**	**# of Elements (embedded)**	**RMS(T) ($x10^{-2}$)**	**RMS(d_T) ($x10^{-4}$)**	**Discrepancy (%)**	**Time step (embedded)**
a1	32	16	5.0029	1.9009	0.3799	109
a2	32	32	5.0029	5.6182	1.1229	237
a3	32	48	5.0029	5.6161	1.1225	338
a4	32	64	5.0029	7.5698	1.5130	469
a5	64	32	10.133	5.0963	0.5029	113

resolution in the containing mesh increases the discrepancy gradually (case a2, a3, and a4). The consistency achieved is encouraging, considering that grid spacing of the embedded mesh in case a4 is four times smaller than that of the containing mesh.

Appendix B

Benchmarks of full-regional CitcomS.py coupling

The containing mesh is a spherical shell extending from an inner radius of 0.5 to an outer radius of 1, and is divided into 12 caps. The side of each cap is ≈55°. The embedded mesh extends from 0°N to 22.5°N, 45°E to 90°E, and 0.75 to 1 in radius. These two meshes share the same top surface. The containing grid is not parallel to the embedded grid. As a result, interpolation error is unavoidable. The grid spacing of the embedded mesh in case b4 is 4.9 times smaller than that of the containing mesh. The initial temperature field has a hot, spherical anomaly sitting below the embedded domain. Therefore, the initial temperature field in the embedded mesh is 0 everywhere, and the flow within is purely driven by the BCs. The embedded velocity field is interpolated to the coordinates of the containing nodes. The interpolated velocity field is compared with the containing velocity field at the 0th time step (Table B-1).

We allow the containing *Solver* to execute for 70 time steps and the embedded *Solver* for the corresponding time steps. One-way communication is used, i.e., no temperature feedback from the embedded *Solver* to the containing *Solver*. Discrepancy in temperature fields can accumulate over time. The embedded temperature field is interpolated to the coordinates of the containing nodes. The interpolated temperature field is compared with the containing

Table B-1. Results of velocity fields at the 0th time step of full-regional coupling. The second column is the number of elements horizontally in a spherical cap of the containing mesh. The third column is the number of elements along the latitude of the embedded mesh. $\mathbf{u}$ is the velocity field in the overlapping region. $\mathbf{d_u}$ is the difference in the velocity fields of the two meshes. RMS is the root mean square. Discrepancy is defined as RMS($\mathbf{d_u}$)/RMS($\mathbf{u}$).

Case	**# of Elements (containing)**	**# of Elements (embedded)**	**RMS(u)**	**RMS(d_u)**	**Discrepancy (%)**
b1	32	16	28.3647	0.308470	1.0781
b2	32	32	28.3647	0.346116	1.2165
b3	32	48	28.3647	0.500369	1.7622
b4	32	64	28.3647	0.500971	1.7662
b5	64	32	28.6791	0.145538	0.5075

Table B-2. Results of temperature fields at 70th time step of full-regional coupling. We only compare the temperature field in the overlapping region. d_T is the difference in the temperature field of the two meshes. Discrepancy is defined as RMS(d_T)/RMS(T). The fifth column is the time step of the embedded mesh when the time step of the containing mesh is 70. Case b5 is terminated early because the temperature fields diverge too much.

Case	**# of Elements (containing)**	**# of Elements (embedded)**	**RMS(T) ($x10^{-2}$)**	**RMS(d_T) ($x10^{-3}$)**	**Discrepancy (%)**	**Time step (embedded)**
b2	32	32	4.1186	2.9344	7.1248	165
b3	32	48	4.1499	3.4362	8.2802	230
b4	32	64	4.1662	4.6017	11.045	289
b5	64	32	2.5045	3.3190	13.252	198*

* The containing mesh is at 44th time step.

temperature field at the 70th time step (Table B-2). The temperature discrepancy of a two-way communication model will be less than 1/70 of the value in Table B-2.

The results in Table B-1 and Table B-2 show a similar trend as the regional-regional coupling benchmark. When the resolutions of the meshes are similar (case b1 and b5), the discrepancy is minimized. Doubling the resolution of both meshes will decrease the discrepancy by half. Refining the resolution in the embedded mesh while keeping the same resolution in the containing mesh increases the discrepancy gradually (case b2, b3, and b4).

The results in Table B-2 show a large discrepancy due to accumulated interpolation error over time. However, if two-way communication is used, the temperature fields of both meshes are synchronized every time step, so that discrepancy never accumulates.

Appendix C

Code listing

All of the codes listed are written in Python. For the sake of simplicity, the codes are greatly simplified, so that the definitions of non-essential functions are omitted and some variables are treated global in scope.

C.1 Simplified structure of *Application*.

```
def main():
      # assign a solver to the current processor
      # (definition omitted)
      solver = assign_solver()

      # allocates memory, initializes variables, etc...
      solver.initialize()

      # solve the initial field if necessary
      # (definition omitted)
      solver.solve_0th_time_step()

      # loop until finished
      while True:
            # notify solver to begin a new time step
            solver.new_time_step()

            # determine the size of the time step
            dt = solver.find_stable_time_step()

            # move forward by dt
            solver.solve_next_time_step(dt)

            # notify the solver to end the time step
            # (definition omitted)
            solver.end_time_step()

            # check the end-of-simulation conditions
            # (definition omitted)
            if is_finished():
                  break
```

```
      # release memory, etc...
      # (definition omitted)
      solver.finalize()
```

C.2 Simplified structure of *CitcomS.py* solver

```
### Remark: coupler is a “global” variable

def initialize():
      # (definitions omitted)
      allocate_memory()
      init_variables()

      # assign a coupler (either a ContainingCoupler
      # or an EmbeddedCoupler) to the solver
      # (definition omitted)
      coupler = assign_coupler()

      # initialize the Exchanger package
      coupler.initialize()


def find_stable_time_step():
      # calculate proposed_dt from grid spacing
      # and velocity field (definition omitted)
      proposed_dt = find_local_stable_time_step()

      # exchange proposed_dt with another solver,
      # clip it if necessary
      dt = coupler.clip_stable_time_step(proposed_dt)

      return dt


def solve_next_time_step(dt):
      # solve the energy equation by a time step
      # of size dt (definition omitted)
      solve_temperature(dt)

      # solve the momentum equation
      solve_velocity()

      # save the result to disk
      # (definition omitted)
      output()


def solve_velocity():
      # EmbeddedCoupler receives velocity BCs
      # from ContainingCoupler and imposes the BCs
      coupler.pre_solve_velocity()
```

```
      # solve the Stokes flow problem
      # (definition omitted)
      solve_stokes_flow()

      # ContainingCoupler sends velocity BCs to EmbeddedCoupler
      coupler.post_solve_velocity()


def new_time_step():
      # update the temperature field of containing
      # solver if using two-way communication
      coupler.new_time_step()
```

C.3 Simplified structure of *Coupler* for *CitcomS-CitcomS* coupling

ContainingCoupler:

```
### Remark: inlet and outlet are “global” variables

def initialize():
      # source will receive the boundary nodes
      # from the sink of EmbeddedCoupler
      source = create_source()

      # outlet will use source to interpolate the data and send
      # the data to the inlet of EmbeddedCoupler
      outlet = create_outlet(source)

      if is_two_way_communication:
            # overlapped is an instance of BoundedMesh,
            # it contains the overlapped nodes of the
            # containing solver (e.g. Figure 3-2C)
            overlapped = create_boundedmesh()

            # sink will broadcast the overlaped nodes
            # to the sources of ContainingCoupler
            sink = create_sink(overlapped)

            # inlet will use sink to receive data sent
            # by outlet of ContainingCoupler
            inlet = create_intlet(sink)


def pre_solve_velocity():
      # do nothing
      pass


def post_solve_velocity():
      # send velocity/stress/temperature BCs to EmbeddedCoupler
      outlet.send()
```

```
def new_time_step():
      if is_two_way_communication:
            # receive temperature from ContainingCoupler
            inlet.recv()

            # replace the temperature field by the received value
            inlet.impose()


def clip_stable_time_step(proposed_dt):
      # exchange the value of dt with EmbeddedCoupler
      ec_dt = exchange_dt(proposed_dt)
      return proposed_dt
```

EmbeddedCoupler:

```
### Remark: inlet, outlet, is_two_way_communication
### cc_dt, accumulated_dt, and was_synchronized are
### “global” variables

def initialize():
      # boundary is an instance of BoundedMesh, it
      # contains the boundary nodes of the
      # embedded solver (e.g. Figure 3-2B)
      boundary = create_boundedmesh()

      # sink will broadcast the boundary nodes to the
      # sources of ContainingCoupler
      sink = create_sink(boundary)

      # inlet will use sink to receive data sent by
      # outlet of ContainingCoupler
      inlet = create_inlet(sink)

      if is_two_way_communication:
            # source will receive the overlapped nodes
            # from the sink of ContainingCoupler
            source = create_source()

            # outlet will use source to interpolate the
            # data and send the data to the inlet
            # of ContainingCoupler
            outlet = create_outlet(source)

      # was synchronized at the previous time step?
      was_synchronized = False

      # dt of ContainingCoupler
      cc_dt = 0

      # dt accumulated since the last synchronized time step
      accumulated_dt = 0


def pre_solve_velocity():
```

```
      # receive velocity/stress/temperature BCs from
      # ContainingCoupler when solvers were synchronized
      # at the previous time step, i.e. both solvers
      # march forward in this time step
      if was_synchronized:
            inlet.recv()

      # impose BCs
      inlet.impose()


def post_solve_velocity():
      # do nothing
      pass


def new_time_step():
      if is_two_way_communication and is_sync():
            # send temperature to ContainingCoupler
            outlet.send()

      # store the sync state of the previous time step
      # in a variable
      if is_sync():
            was_synchronized = True
      else:
            was_synchronized = False


def clip_stable_time_step(proposed_dt):
      if is_sync():
            # exchange the value of dt with
            # ContainingCoupler (definition omitted)
            cc_dt = exchange_dt(proposed_dt)

            # reset the time
            accumulated_dt = 0

      # accumulate the time
      accumulated_dt += dt

      # if after accumulation, the time exceeds that
      # of ContainingCoupler, clip the time
      if accumulated_dt > cc_dt:
            # clip proposed_dt
            dt = proposed_dt – (accumulated_dt - cc_dt)
            accumulated_dt = cc_dt
      else:
            dt = proposed_dt

      return dt


def is_sync():
      if accumulated_dt == cc_dt:
            return True
      else:
            return False
```

Appendix D

Benchmark of compressible Stokes flow solver

We follow a similar procedure to that of *Hager and O'Connell* [1981] to develop an analytical solution for Stokes flow in a compressible, Newtonian fluid. The meanings of the symbols are defined in Chapter 6.

$$\nabla \cdot (\rho_r \mathbf{u}) = 0 \qquad \text{(D-1)}$$

$$-\nabla P + \nabla \cdot \underline{\tau} = \Delta\rho Ra\, \mathbf{e}_z \qquad \text{(D-2)}$$

If the viscosity variation is restricted in the z direction only, the equation can be decomposed in Fourier series. Without losing generality, the flow is assumed to be periodic with a wave number k in the x direction. The flow variables can be expressed as

$$u_z(x,z) = U_z(z)\cos kx \qquad \text{(D-3)}$$

$$u_x(x,z) = U_x(z)\sin kx \qquad \text{(D-4)}$$

$$\sigma_{zz}(x,z) = \Sigma_{zz}(z)\cos kx \qquad \text{(D-5)}$$

$$\sigma_{xx}(x,z) = \Sigma_{xx}(z)\cos kx \qquad \text{(D-6)}$$

$$\sigma_{xz}(x,z) = \Sigma_{xz}(z)\sin kx \qquad \text{(D-7)}$$

$$P(x,z) = \Pi(z)\cos kx \qquad \text{(D-8)}$$

$$\Delta\rho(x,z) = \Omega(z)\cos kx \qquad \text{(D-9)}$$

where $\underline{\sigma}=\underline{\tau}-P\underline{I}$ is the total stress tensor. The reference density profile is assumed to be

$$\rho_r(z) = e^{\beta\,(1-z)} \tag{D-10}$$

where $\beta=Di/\gamma$. Substitution of (D-3), (D-4), and (D-10) into the continuity equation (D-1) yields

$$\partial U_z = -kU_x + \beta U_z \tag{D-11}$$

where ∂ is a shorthand for d/dz.

Similarly, the constitutive relationship, Equation (6-4) and (6-5), becomes

$$\Sigma_{zz} = \eta\left[\frac{4}{3}\partial U_z - \frac{2}{3}kU_x\right] - P \tag{D-12}$$

$$\Sigma_{xx} = \eta\left[-\frac{2}{3}\partial U_z + \frac{4}{3}kU_x\right] - P \tag{D-13}$$

$$\Sigma_{xz} = \eta\left[\partial U_x - kU_z\right] \tag{D-14}$$

The expression for pressure can be obtained by combining (D-11) and (D-12).

$$\Pi = \eta\left[-2kU_x + \frac{4}{3}\beta U_z\right] - \Sigma_{zz} \tag{D-15}$$

The expression of Σ_{xx} can be obtained by combining (D-11), (D-12), and (D-13).

$$\Sigma_{xx} = \Sigma_{zz} - 2\beta\eta U_z + 4k\eta U_x \tag{D-16}$$

The Stokes equation (D-2) becomes

$$-k\Sigma_{xx} + \partial\Sigma_{xz} = 0 \tag{D-17}$$

$$k\Sigma_{xz} + \partial\Sigma_{zz} = \Omega Ra \tag{D-18}$$

Substituting (D-16) into (D-17) yields

$$\partial\Sigma_{xz} = k\Sigma_{zz} - 2\beta k\eta U_z + 4k^2\eta U_x \tag{D-19}$$

Combining (D-11), (D-12), (D-18), and (D-19), we obtain a set of linear equations

$$\partial \begin{bmatrix} U_z \\ U_x \\ \Sigma_{zz}/2\eta_0 k \\ \Sigma_{xz}/2\eta_0 k \end{bmatrix} = \begin{bmatrix} \beta & -k & 0 & 0 \\ k & 0 & 0 & 2k/\eta^* \\ 0 & 0 & 0 & -k \\ -\beta\eta^* & 2k\eta^* & k & 0 \end{bmatrix} \cdot \begin{bmatrix} U_z \\ U_x \\ \Sigma_{zz}/2\eta_0 k \\ \Sigma_{xz}/2\eta_0 k \end{bmatrix} + \begin{bmatrix} 0 \\ 0 \\ \Omega Ra/2\eta_0 k \\ 0 \end{bmatrix} \quad \text{(D-20)}$$

where $\eta^*=\eta/\eta_0$, and η_0 is an arbitrary constant. The purpose of η_0 is to dimensionalize the vector on the left-hand side. Note that when β=0, there is no adiabatic density gradient, and (D-20) is reduced to the result of *Hager and O'Connell* [1981]. Subject to free-slip boundary conditions at the top and bottom surface, (D-20) is a boundary value ordinary differential equation, which can be solved analytically. Instead, we use the *bvp4c* function in *MATLAB* [*Shampine et al*., 2003] to solve the equation numerically up to machine precision. The solution obtained is referred to as the "analytical solution" hereinafter.

We compared the finite element solution with the analytical solution. The finite element calculation is computed using 16, 32, or 64 elements in each direction. By changing the value of *Di* and γ, different approximations of the governing equations are benchmarked: Boussinesq Approximation (BA, *Di*=0 and $\gamma=\infty$), Extended Boussinesq Approximation (EBA, *Di*=0.5 and $\gamma=\infty$), and Truncated Anelatic Liquid Approximation (TALA, *Di*=0.5 and γ=1). The density anomaly is set according to

$$\Delta\rho(x,z) = \rho_r(z)T(x,z) \quad \text{(D-21)}$$

$$T(x,z) = \sin \pi z \cos kx \quad \text{(D-22)}$$

The viscosity is $\eta=e^{az}$, where *a* is either 0 or 2. The result of the benchmark is in Table D-1.

Table D-1. Benchmark of the Stokes flow solver.

Approximation	**a_η**	**# of Elements**	**Relative Error on u_z**
BA	0	16	0.374%
BA	0	32	0.0937%
BA	0	64	0.0234%
TALA	0	16	0.366%
TALA	0	32	0.0916%
TALA	0	64	0.0229%
TALA	2	16	0.450%
TALA	2	32	0.113%
TALA	2	64	0.0281%

References

Hager, B. H., and R. J. Oconnell (1981), A simple global-model of plate dynamics and mantle convection, *J. Geophys. Res.*, *86*, 4843–4867.

Shampine, L. F., I. Gladwell, and S. Thompson (2003), *Solving ODEs with MATLAB*, 272 pp., Cambridge University Press, New York.

Appendix E

Benchmark of compressible temperature solver

Once the analytical solution of the velocity and stress are obtained, they can be substituted into the energy equation (6-3). Assuming $C_P=k_T=\alpha=g=1$, each term of the energy equation can be expressed analytically.

$$-\rho_r \mathbf{u}\cdot\nabla T = e^{\beta\,(1-z)}\left(kU_x \sin^2 kx \sin \pi z - \pi U_z \cos^2 kx \cos \pi z\right) \tag{E-1}$$

$$\nabla \cdot k_T \nabla T = (-k^2 - \pi^2)\cos kx \sin \pi z \tag{E-2}$$

$$Di(T + T_{surf})\rho_r u_z = Di e^{\beta\,(1-z)} U_z \cos kx (\sin \pi z \cos kx + T_s) \tag{E-3}$$

$$\frac{Di}{Ra}\underline{\sigma} : \underline{\varepsilon} = \frac{Di}{Ra}\eta\left(4k^2U_x^2 + \frac{4}{3}\beta^2 U_z^2 - 4\beta k U_x U_z\right)\cos^2 kx + \frac{1}{\eta}\Sigma_{xz}^2 \sin^2 kx \tag{E-4}$$

$$\rho_r H = e^{\beta\,(1-z)} H \tag{E-5}$$

The result of the benchmark is in Table E-1.

Table E-1. Benchmark of the energy equation solver.

Approximation	**a_η**	**# of Elements**	**Relative Error on $\partial T/\partial t$**
BA	0	16	10.11%
BA	0	32	5.20%
BA	0	64	3.40%
TALA	0	16	9.47%
TALA	0	32	4.61%
TALA	0	64	2.64%
TALA	2	16	8.20%
TALA	2	32	3.90%
TALA	2	64	1.92%